From Cuprates to Manganites: Spin and Orbital Liquids

Dissertation zur Erlangung
des akademischen Grades
Doctor rerum naturalium (Dr. rer. nat.)
vorgelegt der Fakultät Mathematik und
Naturwissenschaften der Technischen
Universität Dresden von

Rolf Kilian

aus Ulm

Contents

Perspective

The discovery of high-temperature superconductivity by Bednorz and Müller [BED86] in 1986 sparked the search for new materials with ever higher values of T_c. The "early" compounds $La_{2-x}A_xCuO_4$ with $A = $ Sr, Ba and $YBa_2Cu_3O_{7-y}$ as well as most other high-T_c materials discovered in subsequent years all share one common feature: They are built out of layered CuO_2 planes forming quasi-two-dimensional electron systems. It is one of the most striking observations in the physics of cuprates that the same electrons can experience superconductivity at finite doping and antiferromagnetic order in the undoped ($x = 0$) system. It seems to be clear that these two phenomena must be intimately related to each other; a full understanding of the properties of high-T_c cuprates hence goes hand in hand with a better grasp of the peculiar nature of the CuO_2 planes (for reviews see, e.g., [AND97, IMA98]).

Manganites, on the other hand, have a much longer history to look back upon than cuprates. In their perovskite form, i.e., $R_{1-x}A_xMnO_3$ where R and A represent rare earth and divalent metal ions, respectively, they were already under investigation for the peculiar interplay between ferromagnetism and metalicity in the early 1950's: At certain doping levels, these compounds were found to be in a ferromagnetic metallic state at low temperatures which could be driven to a paramagnetic insulating one by raising the temperature [JON50]. Recently, interest in manganites has been revitalized by the discovery of colossal magnetoresistance [JIN94] and has since been further stimulated by successive observations of a variety of interesting effects (for reviews see, e.g., [RAM97, IMA98]).

Both cuprates and manganites belong to the transition metal oxides. The physics of these compounds is characterized by a dualism of local electron interaction and itinerant charge motion. The former originates in the strong repulsion between electrons in the d shells of transition metal ions, the latter in the hybridization of these states with $2p$ orbitals of oxygen. In the undoped parent compound of cuprates and of many manganites, correlations prevail as an insulating and antiferromagnetically ordered Néel state is formed. Upon doping the system can be turned metallic, but it is still reminiscent of its

correlated nature. This effect is most pronounced in the cuprates: At low doping, the metallic state exhibits local antiferromagnetic correlations which signal the proximity to the spin-ordered Néel state. Furthermore, gaplike features in the magnetic excitation spectrum become observable that manifest local spin-singlet correlations which can be thought of as a precursor effect of superconductivity. It is difficult if not impossible to reconcile these peculiar features with a conventional theory of metals, and it is now widely recognized that strong correlations must be the key ingredient of a comprehensive understanding of cuprates. Correlation effects in manganites, on the other hand, have for long been considered only in an indirect manner: Early work which established the notion of double exchange [ZEN51, AND55, DEG60] is based on the incidence of a strong Hund's coupling stemming from the on-site repulsion between d electrons. Recently, however, it has become clear that one has to go beyond double exchange to explain the multitude of peculiar features of manganites and that a more thorough treatment of correlation effects in these compounds is needed.

In the following chapters, we address several key issues of metallic cuprates and manganites. The work is based on the notion of spin and orbital liquids: These represent elegant tools to handle the strongly correlated nature of the metallic state in an efficient and transparent way. We shortly introduce these concepts in Chapter 1 which gives an overview of the methods and the relevant models employed throughout this work. In Chapter 2, we analyze the peculiar magnetic response of metallic cuprates upon impurity doping. We argue that the magnetic behavior can be well understood if one assumes the spins of the CuO_2 planes to form a spin liquid. The subsequent Chapters 3 - 5 are devoted to the metallic state of manganites. Elaborating on the notion of an orbital liquid, we study the interplay of electron correlations, orbital degeneracy, and double exchange. We assert that several puzzling experimental observations can be resolved in a natural way by adopting a strong-correlation picture of metallic manganites. In general, the results on cuprates and manganites presented in this thesis closely agree with experiment. We believe this to strongly support the validity of our approach and to give new insight into the spectacular and sometimes astonishing physics of transition metal oxides.

Chapter 1

From Cuprates to Manganites: A Short Primer

1.1 Introduction

Cuprates and manganites both belong to the class of transition metal oxides. It is therefore not surprising that the two compounds are of very similar structure. Nevertheless, the physical behavior strongly deviates which is most clearly manifested in the phase diagram (see Fig. 1.1): Both substances show signs of antiferromagnetism at zero doping. Upon the insertion of holes the behavior drifts apart. Roughly, cuprates can then be characterize as metals with a pronounced instability towards superconductivity and manganites as insulators with an instability towards metalicity and ferromagnetism. The staggered spin structure of the parent compounds suggests an underlying Mott-Hubbard system in both cases. Besides this basic similarity, the following key differences can be identified to be foremost responsible for the distinct behavior at finite doping: (1) In cuprates only one $3d$ electron per site is of physical relevance. In manganites, on the other hand, the $3d$ states of the Mn ions provide an additional background of local $S = \frac{3}{2}$ spins that ferromagnetically interact with the itinerant electrons via Hund's coupling. This gives rise to double exchange which is absent in cuprates. (2) Only one orbital per Cu site is active in cuprates. This differs from the case of manganites where the itinerant electrons can move within orbital doublets, yielding an additional orbital degree of freedom. (3) The $3d$ electrons form small $S = \frac{1}{2}$ spins in cuprates which are subject to strong quantum fluctuations. In contrast, the large $S = 2$ spins in manganites behave more classically. (4) Electrons are essentially confined to two dimensions in cuprates but can move in three dimensions in perovskite manganites.
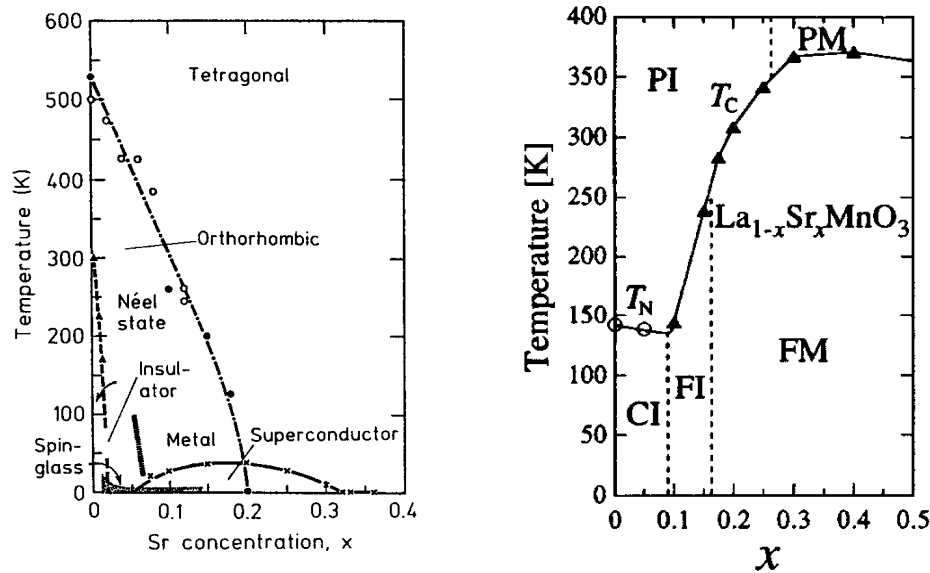
Figure 1.1: *Phase diagram of $La_{2-x}Sr_xCuO_4$ (left) and $La_{1-x}Sr_xMnO_3$ (right). At zero doping, $LaMnO_3$ is an A-type antiferromagnet with antiferromagnetic order in c direction and ferromagnetic order in ab planes [WOL55, GOO55]. The phases on the right are denoted as follows: canted insulator (CI), ferromagnetic insulator (FI), ferromagnetic metal (FM), paramagnetic metal (PM), and paramagnetic insulator (PI). From [BIR89], [URU95].*

In this chapter, we give a short overview of the physics relevant to cuprates and manganites. The emphasis is on a comparison between the two substances and the introduction of concepts relevant for later chapters. Where it is necessary to be specific we restrict ourselves to the two compounds that are most closely related to each other: $La_{2-x}Sr_xCuO_4$ and $La_{1-x}Sr_xMnO_3$ to represent cuprates and manganites, respectively. We note that throughout this work manganites are considered only in their perovskite form; the layered compounds are discarded (for these see, e.g., [MOR96]). In the following we discuss the crystal and electronic structure of the two substances and expand on the orbital degeneracy encountered in the latter. We then introduce the effective Hamiltonians that capture the relevant low-energy physics of orbitally non-degenerate and degenerate Mott-Hubbard systems. To describe the strongly correlated metallic state of cuprates, the notion of a spin liquid is reviewed. This picture is finally extended to an orbital liquid which accounts for correlation effects in metallic manganites.
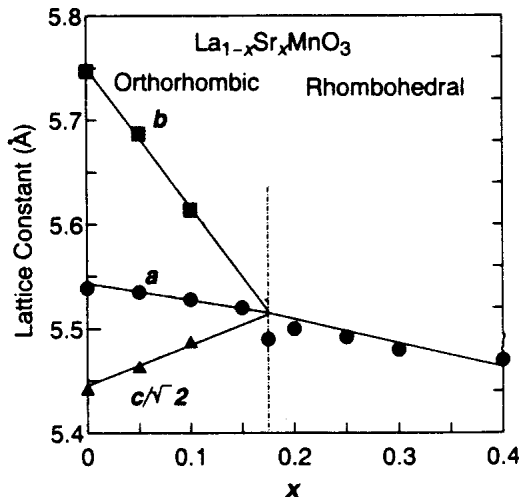
Figure 1.2: *Change of the lattice parameter with doping in $La_{1-x}Sr_xMnO_3$ at room temperature. From [URU95].*

1.2 Crystal Structure

The crystal structure of cuprates varies within a broad range except for one common feature shared by all compounds: a stacking structure of two dimensional CuO_2 planes. For illustration, we shortly review the structure of $La_{2-x}Sr_xCuO_4$ here. Manganites, on the other hand, are frequently studied in their layered and perovskite form. Here we restrict ourselves to the latter one, choosing $La_{1-x}Sr_xMnO_3$ as an example.

The basic building blocks of $La_{2-x}Sr_xCuO_4$ as well as of $La_{1-x}Sr_xMnO_3$ are $(Cu/Mn)O_6$ octahedra surrounded by La/Sr atoms as shown in Fig. 1.3(a). In the cuprate compound these cells form well separated CuO_2 planes. The crystal symmetry is orthorhombic at low doping concentrations ($x < 10\%$) and tetragonal at higher ones [see Fig. 1.3(b)]. The two-dimensional character of $La_{2-x}Sr_xCuO_4$, which is implied by its layered structure, is further enhanced by a Jahn-Teller distortion of the CuO_6 octahedra perpendicular to the planes. The Cu-O distances in ab and c directions, which are 1.9 Å and 2.4 Å, respectively, hence deviate significantly [HAZ90]. In the manganese oxide $La_{1-x}Sr_xMnO_3$, on the other hand, the MnO_6 octahedra form a perovskite structure [see Fig. 1.3(c)]. At low doping concentrations ($x < 17.5\%$), the crystal is subject to a cooperative Jahn-Teller distortion which reduces the symmetry to orthorhombic [KAN60]. At higher doping levels, cubic symmetry is recovered. The change of lattice parameters with doping is indicated in Fig. 1.2 [URU95]. Replacing La and Sr by other rare earth and divalent metal ions leaves the crystal structure unaffected but in-

duces a canting of Mn-O bonds which can be used as an experimental tool to vary the bandwidth [HWA95].

1.3   Electronic Structure

The key elements of the electronic structure of cuprates and manganites are the partially filled $3d$ states. Depending upon the symmetry of the crystal field, the degeneracy of these states is lifted (see Fig. 1.4). In a cubic environment as in metallic manganites, the $3d$ states split into a lower-lying t_{2g} triplet and a higher-lying e_g doublet. This splitting is of the order of several eV. In the tetragonal or orthorhombic structure of cuprates, the e_g doublet further splits up into a lower-lying $d_{3z^2-r^2}$ and a higher-lying $d_{x^2-y^2}$ state. These two states are separated by an energy of the order of one eV.

At zero doping the $3d$ states of cuprates and manganites are filled by 9 and 4 electrons, respectively. This follows from a valency of 3+ for La and 2− for O, which leaves Cu in 2+ and Mn in 3+. Replacing La by Sr with a valency of 2+ effectively reduces the $3d$ electron number by one per doped ion (at zero doping, cuprates and manganites are charge-transfer insulators — doped holes enter O $2p$ states, the remaining unpaired spins form Zhang-Rice singlets with unpaired $3d$ electrons).

The $3d$ electrons, both in cuprates and manganites, are subject to a strong mutual repulsive interaction which is significantly larger than the transfer amplitude between sites (photoemission experiments yield an on-site repulsion of 5 - 10 eV [SHE87, FUJ89, SAI95, SAR96]). This has two important consequences which follow from the urge of the system to reduce its ground-state energy: (1) The number of $3d$ electrons per site is minimized; and (2) multiple $3d$ electrons at one site try to form a high-spin state which promotes a ferromagnetic Hund's coupling between unpaired $3d$ electrons in different orbitals.

Hund's coupling plays no active role in cuprates — in the parent compound all $3d$ states except one are filled, leaving only one unpaired $3d$ electron per Cu site [see Fig. 1.5(a)]. This unpaired electron resides in the state of highest energy which is an antibonding orbital formed of Cu $3d_{x^2-y^2}$ and O $2p$ with predominantly $d_{x^2-y^2}$ character. Due to the hybridization with oxygen, the $d_{x^2-y^2}$ electrons can hop between nearest-neighbor Cu sites within the two-dimensional CuO_2 planes. The amplitude for tunneling between planes, on the other hand, is only small. This anisotropy is reflected in the normal-state resistivity: At finite doping cuprates are good metals along the planes but almost insulating perpendicular to them [IYE90]. In manganites the $3d$ states are filled by only 4 electrons which are subject to Hund's rule: Three
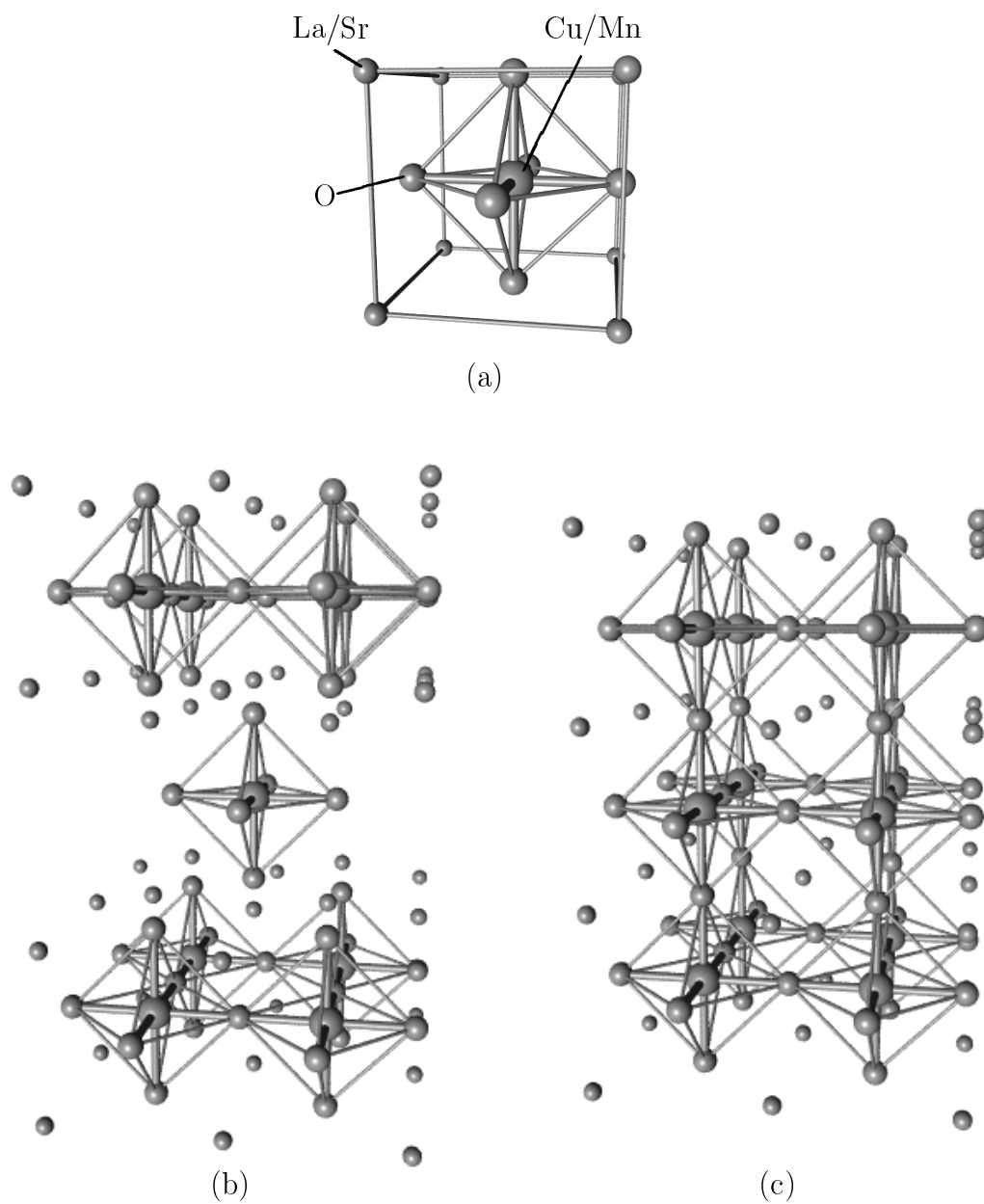
Figure 1.3: $(Cu/Mn)O_6$ octahedra surrounded by La/Sr ions (a) are the basic building block of (b) tetragonal $La_{2-x}Sr_xCuO_4$ and (c) rhombohedral $La_{1-x}Sr_xMnO_3$.
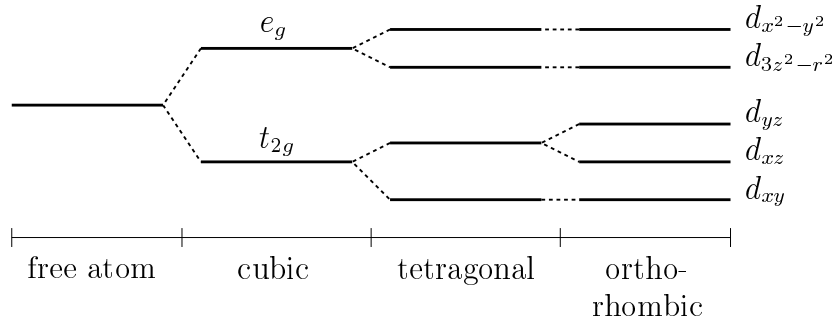
Figure 1.4: *The degeneracy of 3d states is lifted by the crystal field.*
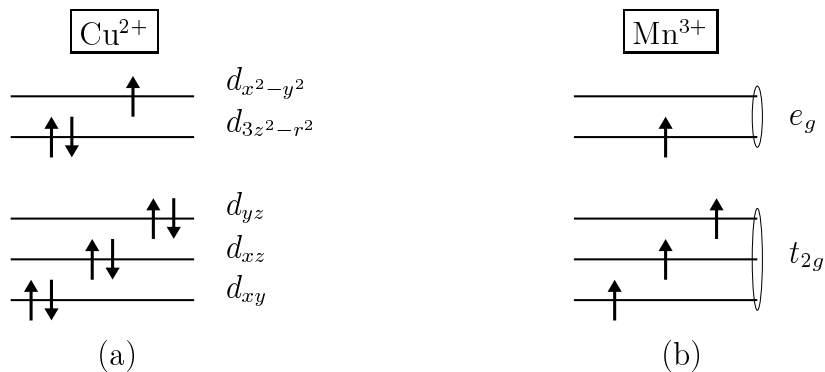
Figure 1.5: *(a) In cuprates the electronically active states are the singly occupied $d_{x^2-y^2}$ orbitals. (b) In manganites half-filled t_{2g} triplets form local spins $S = \frac{3}{2}$, interacting ferromagnetically with electrons in singly occupied e_g doublets. Degenerate orbitals are encircled.*

electrons enter the lower-lying t_{2g} triplet, forming a localized spin $S^c = \frac{3}{2}$, the remaining one electron is placed in either one of the two degenerate e_g states [see Fig. 1.5(b)]. The latter form antibonding orbitals with O $2p$ states and are predominantly of $d_{x^2-y^2}$ and $d_{3z^2-r^2}$ character. Due to this hybridization, the e_g electrons can hop between Cu sites in all three principal directions. In contrast to cuprates the resistivity of metallic manganites shows no anisotropy [URU95].

The ferromagnetic Hund's coupling between itinerant e_g and localized t_{2g} electrons is the origin of the peculiar interplay between conductivity and magnetism observed in doped manganites. According to estimates from photoemission experiments, the magnitude of this coupling is $J_H \approx 2.5$ eV in $La_{1-x}Sr_xMnO_3$, which is larger than the one-electron bandwidth $W \approx 1.5$ eV [HWA96]. In the ferromagnetic phase at $T < T_C$ this results in a split-

$$t^{\mathrm{eff}} = t \qquad t^{\mathrm{eff}} = 0 \qquad t^{\mathrm{eff}} = \cos(\Phi/2)t$$
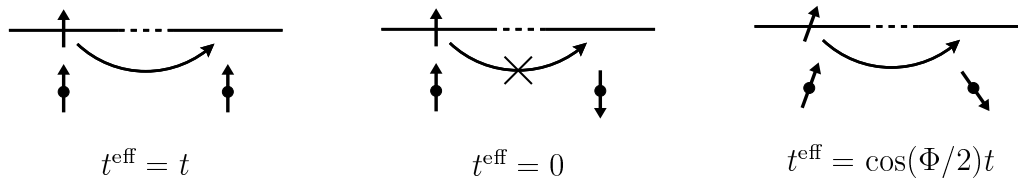
Figure 1.6: *Double-exchange model: The hopping amplitude reaches its maximum if the core spins are aligned in parallel and vanishes in the case of an antiparallel orientation. In general the hopping amplitude is modulated by a factor $\cos(\Phi/2)$, where Φ is the angle between core spins.*

ting of the conduction band into well separated spin-polarized bands. At low enough energies, the physics of manganites is then fully captured by the limit $J_H \rightarrow \infty$ in which localized and itinerant $3d$ electrons together form a large on-site spin $S = 2$. This limit is assumed by the double-exchange model which in addition employs a classical treatment of spins [ZEN51, AND55, DEG60]. The model relates charge mobility and ferromagnetism as follows: The transfer amplitude of e_g electrons depends on the relative orientation of spins as described by (see Fig. 1.6)

$$t^{\mathrm{eff}} = t\sqrt{\frac{1 + m^2}{2}}, \quad m = \frac{\langle \boldsymbol{S}_i \boldsymbol{S}_j \rangle}{S^2}, \tag{1.1}$$

where m is the normalized magnetization. Electron motion is hence unaffected by Hund's coupling if all core spins are aligned ferromagnetically, while it is blocked if the core spins form an antiferromagnetic background. The kinetic energy is minimized in the former case which establishes a ferromagnetic interaction between sites. On the other hand, a quenching of the magnetization which can, e.g., be induced by raising the temperature, suppresses the conductivity. Figure 1.7 shows experimental data on the interplay between magnetization and resistivity in $\mathrm{La}_{1-x}\mathrm{Ca}_x\mathrm{MnO}_3$. For a detailed study of the metal-insulator transition in manganites and the role played by lattice and orbital degrees of freedom we refer to Chap. 5.

1.4 Orbital Degeneracy in Manganites

The degeneracy of e_g states in manganites implies that the itinerant electrons carry an orbital degree of freedom which is absent in cuprates. To keep track of this orbital quantum number it is convenient to define an orbital isospin operator $\boldsymbol{T} = (T^x, T^z)$ with $T^{x/z} = \frac{1}{2}\sigma^{x/z}$. The Pauli matrices $\sigma^{x/z}$ act on the orbital subspace for which one conventionally chooses the orthogonal orbitals
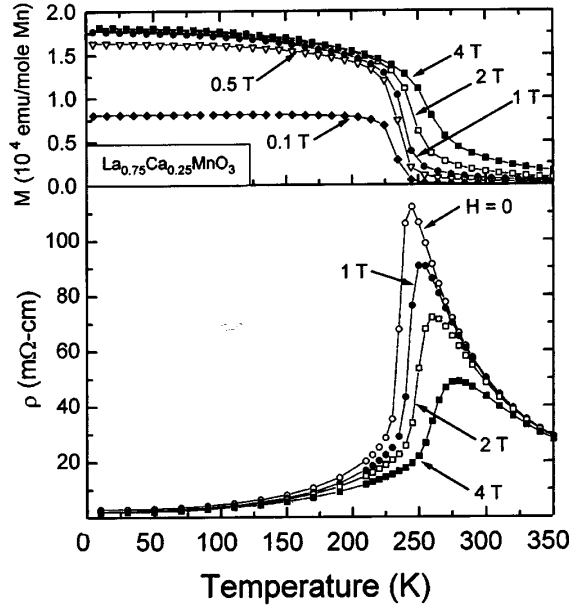
Figure 1.7: *Experimental realization of double exchange in $La_{0.75}Ca_{0.25}MnO_3$: Magnetization (top) and resistivity (bottom). From [SCH95].*

$d_{3z^2-r^2}$ and $d_{x^2-y^2}$ as a basis set. These orbitals correspond to isospin vectors $\langle \boldsymbol{T} \rangle = (0, \frac{1}{2})$ and $(0, -\frac{1}{2})$, respectively. Generally, the isospin vector

$$\langle \boldsymbol{T} \rangle^\Theta = \frac{1}{2}(\sin \Theta, \cos \Theta) \tag{1.2}$$

represents the orbital state

$$|\Theta\rangle = \cos\left(\frac{\Theta}{2}\right)|3z^2 - r^2\rangle + \sin\left(\frac{\Theta}{2}\right)|x^2 - y^2\rangle. \tag{1.3}$$

Due to the cubic symmetry, a rotation in real space by 90° around the x, y, or z axis changes the orientation but not the geometry of orbitals. For instance, the orbital state $|3z^2 - r^2\rangle$ pointing in the z direction can be mapped onto $|3x^2 - r^2\rangle$ pointing in the x direction by a rotation around the y axis. In isospin space these transformations correspond to (successive) rotations by $\Theta = \frac{2\pi}{3}$ (see Fig. 1.8).

In an orbitally degenerate system the transfer amplitude of e_g electrons between Cu sites depends on the orbital orientation, i.e., the orbital quantum number of the initial and the final state and the direction of the transfer. Along the z direction, only the $|3z^2 - r^2\rangle$ orbital has a finite overlap with the $2p$ states of neighboring oxygens — the overlap of $|x^2 - y^2\rangle$ with these states
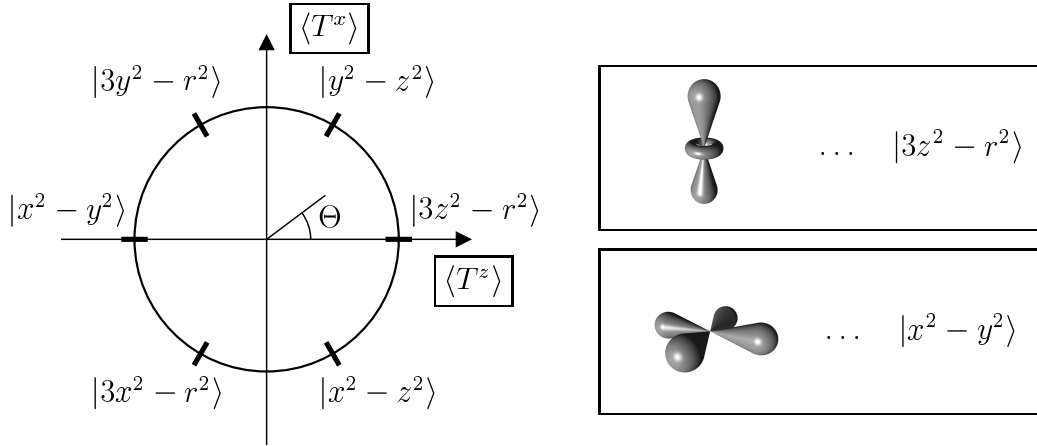
Figure 1.8: *Orbital isospin vector $\langle \boldsymbol{T} \rangle^\Theta = \frac{1}{2}(\sin\Theta, \cos\Theta)$. The orthogonal pair of orbitals $|3z^2 - r^2\rangle$ and $|x^2 - y^2\rangle$ shown on the right is associated with angles in isospin space $\Theta = 0, \pi$, respectively. The rotated orbital pairs $|3x^2 - r^2\rangle$, $|y^2 - z^2\rangle$ and $|3y^2 - r^2\rangle$, $|x^2 - z^2\rangle$ correspond to $\Theta = \frac{4\pi}{3}, \frac{\pi}{3}$ and $\Theta = \frac{2\pi}{3}, \frac{5\pi}{3}$, respectively.*

vanishes [KUG73]. Hence, the transfer matrix in the z direction is simply (see Fig. 1.9)

$$t_z^{\alpha\beta} = t \begin{pmatrix} 1 & 0 \\ 0 & 0 \end{pmatrix} \tag{1.4}$$

within orbital basis $\{|3z^2 - r^2\rangle, |x^2 - y^2\rangle\}$. The transfer matrices for bonds along the x and y directions can be obtained by performing a rotation in isospin space as discussed above, yielding

$$t_{x/y}^{\alpha\beta} = t \begin{pmatrix} 1/4 & \mp\sqrt{3}/4 \\ \mp\sqrt{3}/4 & 3/4 \end{pmatrix}. \tag{1.5}$$

It is important to note that orbital pseudospin is not a conserved quantum number in the present system. This follows from the fact that there is no orbital basis set which would simultaneously diagonalize the three transfer matrices $t_x^{\alpha\beta}$, $t_y^{\alpha\beta}$, and $t_z^{\alpha\beta}$. Consequently orbital states get mixed by inter-site transfer processes.

The partially filled e_g states of Mn in cubic manganese compounds are Jahn-Teller active, i.e., the system can gain energy from a local deformation of the crystal which lifts the e_g degeneracy. In the undoped compound LaMnO$_3$ a strong distortion of MnO$_6$ octahedra ascribed to a cooperative Jahn-Teller effect is observed below $T_O = 780$ K [KAN60]. This distortion vanishes as the system becomes metallic at hole concentrations above $x = 17.5\%$ [URU95]. Recently, static Jahn-Teller distortions have also been
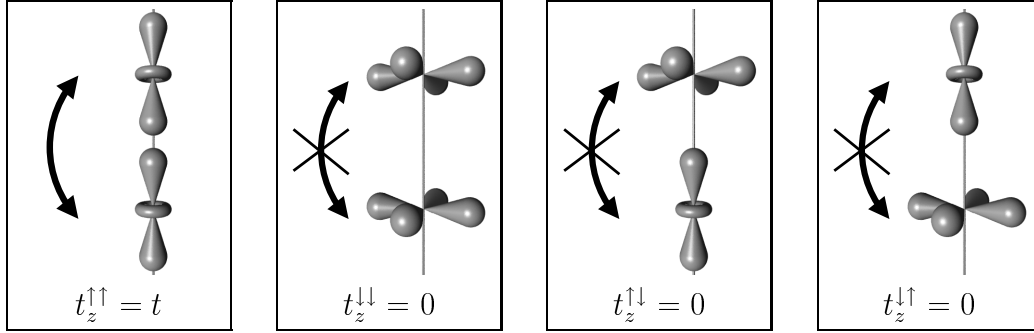
Figure 1.9: *Along the z direction, electrons can hop only from $|3z^2 - r^2\rangle$ into $|3z^2 - r^2\rangle$ orbitals. Transfer processes involving $|x^2 - y^2\rangle$ orbitals are forbidden due to the vanishing overlap with the in-between O 2p states (not shown).*

observed to develop as the ferromagnetic metal turns into a paramagnetic insulator at temperature above T_C [BIL96, KAP96, LOU97, BOO98, LAN98] (see Fig. 1.10). Due to the frustrating effect of holes, long-range Jahn-Teller distortions are absent here and only local distortions can be observed.

In the cubic system two independent Jahn-Teller modes Q_2 and Q_3 exist which lift the degeneracy of singly occupied e_g orbitals [KUG82]. These two modes correspond to a set of orthogonal vectors in isospin space for which one conventionally chooses $\langle \boldsymbol{T} \rangle = (\frac{1}{2}, 0)$ and $(0, \frac{1}{2})$, respectively. The displacement of oxygen ions associated with these modes is indicated in Figs. 1.11(b) and 1.11(c). In addition to the two Jahn-Teller modes acting on singly occupied sites, there exists a lattice breathing mode Q_1 that couples to holes, i.e., to sites with no e_g electron. The corresponding displacement of oxygen ions is show in Fig. 1.11(a). The Hamiltonian

$$H_{\text{el-ph}} = -\sum_i \left(g_1 Q_{1i} n_i^h + g_2 Q_{2i} \sigma_i^x + g_3 Q_{3i} \sigma_i^z + \frac{K}{2} \boldsymbol{Q}_i^2 \right) \qquad (1.6)$$

describes the interaction between electrons/holes and the three lattice modes $\boldsymbol{Q}_i = (Q_{1i}, Q_{2i}, Q_{3i})$. Here, K is the lattice spring constant, $g_{1/2/3}$ denote the coupling constants, n_i^h is the number operator for holes, and the Pauli matrices $\sigma_i^{x/z}$ act on the orbital subspace with basis $\{|3z^2 - r^2\rangle, |x^2 - y^2\rangle\}$.

Jahn-Teller and breathing mode distortions mediate an interaction between neighboring Mn sites. Here we discuss the coupling between two singly occupied sites, first considering a bond along the z direction (see Fig. 1.12). Integrating over oxygen displacements and noting that only the Q_3 but not the Q_2 Jahn-Teller mode has a z component (see Fig. 1.11), we obtain from
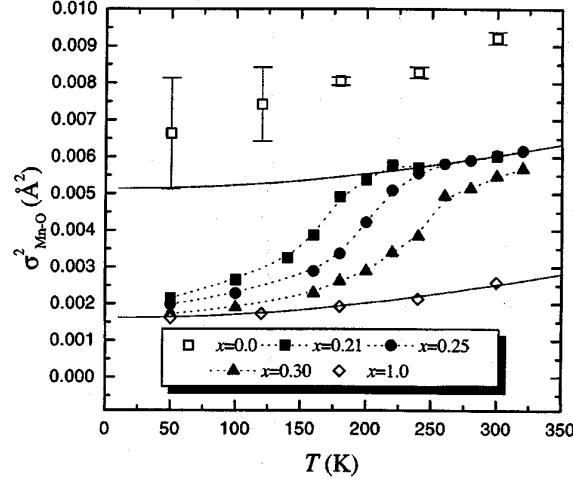
Figure 1.10: *Local Mn-O bond-length distribution in $La_{1-x}Ca_xMnO_3$ obtained by X-ray-absorption fine-structure measurements. Static Jahn-Teller distortions develop at the metal-insulator transition. The magnitude of distortions in the high-temperature insulating phase is comparable to those in $LaMnO_3$. From [BOO98].*

Eq. (1.6) the following interaction Hamiltonian:

$$H_{JT}^z = J_{JT} \sum_{\langle ij \rangle_z} \tau_i^z \tau_j^z, \tag{1.7}$$

with $J_{JT} = g_2^2/K = 2E_{JT}$ and $\tau_i^z = \frac{1}{2}\sigma_i^z$. Equation (1.7) describes an antiferro-type interaction between orbital pseudospins. The corresponding expressions for bonds pointing along the x and y directions can be obtained by a rotation in isospin space as discussed above, yielding the full Jahn-Teller
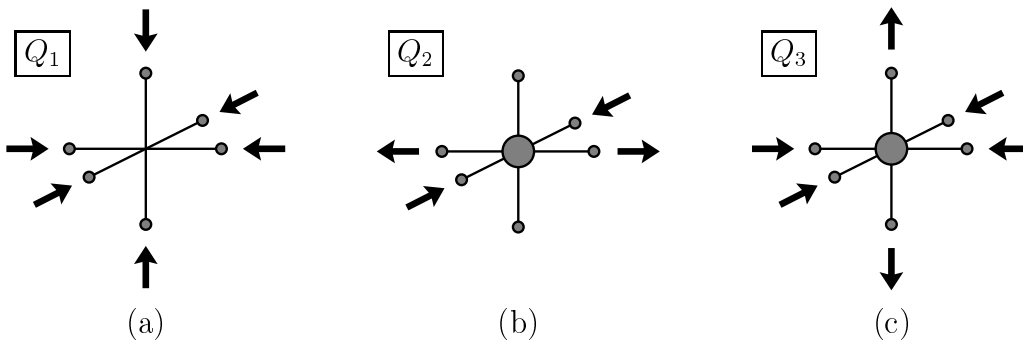
Figure 1.11: *Holes couple to the lattice via a breathing mode (a) Q_1 and electrons via two independent Jahn-Teller modes (b) Q_2 and (c) Q_3.*
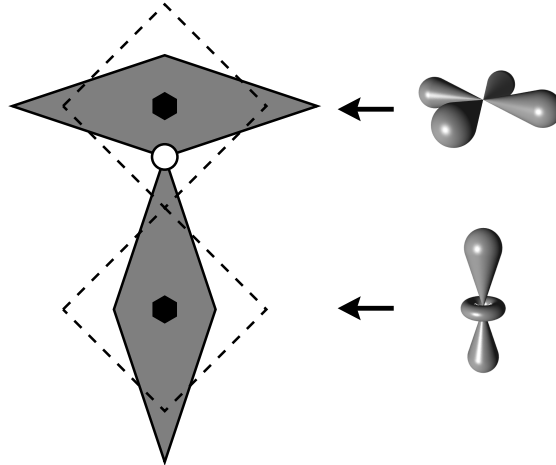
Figure 1.12: *Jahn-Teller mediated interaction between two Mn sites (black hexagons): A displacement of the oxygen ion (white circle) shared by neighboring MnO_6 octahedra leads to an antiferro-type interaction between orbital pseudospins.*

coupling Hamiltonian

$$H_{\mathrm{JT}} = J_{\mathrm{JT}} \sum_{\langle ij \rangle_\gamma} \tau_i^\gamma \tau_j^\gamma, \qquad (1.8)$$

with bond indices $\gamma \in \{x, y, z\}$ and orbital pseudospin operators

$$\tau_i^{x/y} = -\frac{1}{4}\left(\sigma_i^z \pm \sqrt{3}\sigma_i^x\right), \quad \tau_i^z = \frac{1}{2}\sigma_i^z. \qquad (1.9)$$

The characteristic Jahn-Teller energy E_{JT} is about 0.2 - 0.5 eV [DES98, MIL98] which is considerably less than the bandwidth. Hence, the motion of charge carriers in metallic manganites induces strong fluctuations in the orbital subsector. The mixing between electronic and lattice degrees of freedom described by Hamiltonian (1.6) then implies the absence of static lattice distortions. On the other hand, a breakdown of orbital fluctuations, e.g., by the development of orbital order, leads to a distortion of the crystal structure. In fact, Jahn-Teller coupling can be the driving force behind orbital order. This is the case in undoped $LaMnO_3$ which is subject to a cooperative Jahn-Teller effect [KAN60]. X-ray resonant scattering actually shows an antiferro-type orbital structure in this compound that complies with Hamiltonian (1.8) [MUR98, FAB98, ISH98]. However, Jahn-Teller effect is not the exclusive mechanism behind orbital order. This can be seen from the variety of orbital structures in manganites [MAE98a, MAE98b]. For instance, the establishment of one- or two-dimensional orbital networks in a ferro-type orbital orientation as shown in Fig. 1.13 allows for a reduction of

1D   2D
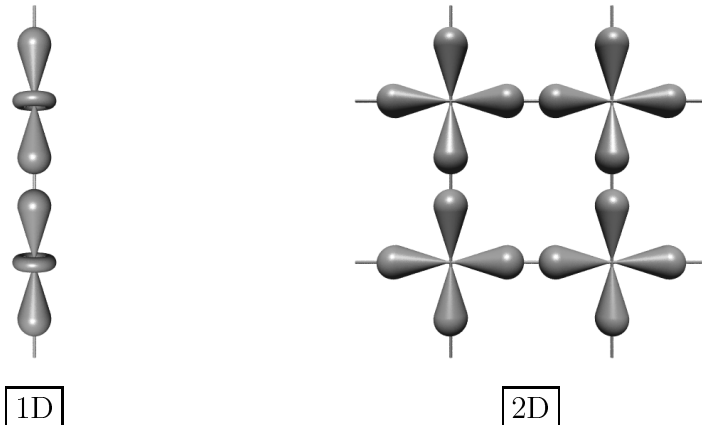
Figure 1.13: *A ferro-type orbital alignment allows for the formation of one- or two-dimensional orbital networks that reduce the kinetic energy of electrons.*

the kinetic energy by maximizing the inter-site transfer amplitude. Experimentally, two-dimensional layered structures have recently been observed in heavily doped manganites [KAW97, MOT98]. This interplay of kinetic energy and Jahn-Teller effect in establishing correlations among neighboring orbitals has important implications for the spin dynamics of ferromagnetic manganites which are discussed in Chap. 4.

1.5   Effective Model Hamiltonians

Shortly after the discovery of high-T_C superconductivity in cuprates it was suggested that this phenomenon should be discussed in terms of a doped Mott-Hubbard insulator [AND87, ZHA88]. Since then much of our understanding of the physics of cuprates has come from the study of the Hubbard model and its strong-coupling descendent, the t-J model. A first starting point is the three-band Hubbard model that describes Cu $d_{x^2-y^2}$ and O p_x, p_y orbitals on a two-dimensional square lattice. Great simplification is achieved by a mapping onto an effective low-energy one-band Hubbard model,

$$H_{\text{Hub}} = -t \sum_{\langle ij \rangle} \sum_s \left(c_{is}^\dagger c_{js} + \text{H.c.} \right) + U \sum_i n_i^\uparrow n_i^\downarrow, \qquad (1.10)$$

which is widely believed to contain the relevant physics of cuprates. In the strong-coupling limit $U \gg t$, the on-site interaction term forbids all but virtual double occupancies of sites. Equation (1.10) can then be further simplified by a projection onto the part of the Hilbert space that comprises only empty and singly occupied sites (see, e.g., [FUL95]). This yields the t-J
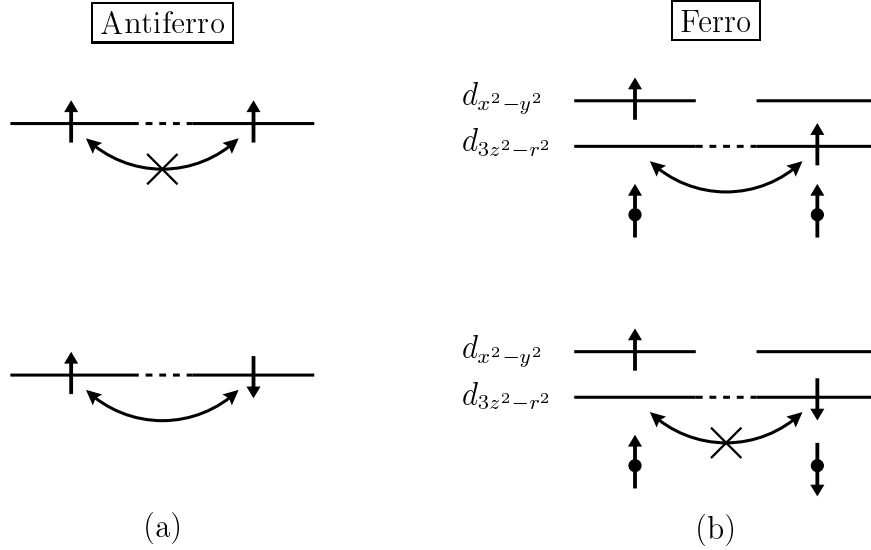
Figure 1.14: *Spin dependence of superexchange: (a) In the conventional t-J model the coupling is antiferromagnetic due to Pauli's exclusion principle. (b) In the orbitally degenerate model, Hund's coupling promotes a ferromagnetic interaction.*

Hamiltonian

$$H_{tJ} = -t \sum_{\langle ij \rangle} \sum_s \left(\hat{c}_{is}^\dagger \hat{c}_{js} + \text{H.c.} \right) + J_{\text{SE}} \sum_{\langle ij \rangle} \left(\boldsymbol{S}_i \boldsymbol{S}_j - \frac{1}{4} \right) n_i n_j, \qquad (1.11)$$

with superexchange coupling constant $J_{\text{SE}} = 4t^2/U$ and constrained electron operators $\hat{c}_{is}^\dagger = c_{is}^\dagger (1 - n_i)$ that create electrons on site i with spin index s under the condition that the site is empty. The superexchange mechanism in this conventional t-J model leads to an *antiferromagnetic* coupling between spins. This is a consequence of Pauli's exclusion principle which allows only for exchange processes of electrons in a spin-singlet configuration [see Fig. 1.14(a)].

In manganites the physics is more involved as one has to take into account the orbital degeneracy of e_g electrons as well as the ferromagnetic Hund's coupling between $3d$ electrons. We use the following Hubbard Hamiltonian

$$\begin{aligned} H_{\text{Hub}} \quad = \quad & -\sum_{\langle ij \rangle_\gamma} \sum_{s\alpha\beta} t_\gamma^{\alpha\beta} \left(c_{is\alpha}^\dagger c_{js\beta} + \text{H.c.} \right) - J_H \sum_i \boldsymbol{S}_i^c \boldsymbol{s}_i \\ & + \sum_i \sum_\alpha U n_{i\uparrow\alpha} n_{i\downarrow\alpha} + \sum_i \sum_{\alpha\neq\beta}{}' \left(U' - J_H \hat{P} \right) n_{i\alpha} n_{i\beta}, \quad (1.12) \end{aligned}$$

with $\hat{P} = \left(\boldsymbol{s}_{i\alpha} \boldsymbol{s}_{i\beta} + \frac{3}{4} \right)$. The indices α/β and s stand for orbital and spin quantum numbers of e_g electrons, respectively; double counting is excluded

from the primed sum. The spin operators $\boldsymbol{s}_{i\alpha}$ act on e_g electrons in orbital α and $\boldsymbol{s}_i = \sum_\alpha \boldsymbol{s}_{i\alpha}$; core-spin operators are denoted by $\boldsymbol{S}_i^c$. The first term in Eq. (1.12) describes the inter-site transfer of electrons within degenerate e_g levels. The interaction of these itinerant electrons with the localized core spins via Hund's coupling is captured by the second term. Finally, the last two terms in Eq. (1.12) describe the intra- (inter-) orbital Coulomb interaction U (U') and the Hund's coupling between e_g electrons in doubly occupied states. In analogy to the transformation from a conventional Hubbard to the t-J model, Eq. (1.12) can be projected onto the part of the Hilbert space with no double occupancies in the limit of strong on-site repulsions $U, (U' - J_H) \gg t$. Due to the presence of Hund's coupling, the energy level of doubly occupied sites depends on the spin orientation of core and e_g spins — a rich multiplet structure follows [FEI99]. The problem considerably simplifies in the limit of large Hund's coupling J_H which we believe to be realistic to manganites: Transitions to the lowest-lying intermediate state with energy $U_1 = U' - J_H$ in which core and e_g spins are in a high-spin configuration then dominate. Doubly occupied sites with different spin structures lie higher by an energy of the order of $\propto J_H$ and can be neglected. We hence obtain the following t-J Hamiltonian:

$$
\begin{aligned}
H_{tJ} &= -\sum_{\langle ij \rangle_\gamma} \sum_{s\alpha\beta} t_\gamma^{\alpha\beta} \left(\hat{c}_{is\alpha}^\dagger \hat{c}_{js\beta} + \text{H.c.} \right) - J_H \sum_i \boldsymbol{S}_i \boldsymbol{s}_i \\
&\quad - J_{\text{SE}} \sum_{\langle ij \rangle_\gamma} \left(\frac{1}{4} - \tau_i^\gamma \tau_j^\gamma \right) \left[\boldsymbol{S}_i \boldsymbol{S}_j + S(S+1) \right] n_i n_j, \qquad (1.13)
\end{aligned}
$$

with coupling constant $J_{\text{SE}} = (2t^2/U_1)[S(2S + 1)]^{-1}$. Orbital pseudospin operators τ^γ are defined in Eq. (1.9) and $\boldsymbol{S}_i$ refers to the total $3d$ spin of site i with $S_i = S_i^c + s_i$. Equation (1.13) is the generalization of orbitally degenerate superexchange models [KUG82, ISH96, ISH97b, FEI99] for arbitrary values of spin.

The first two terms of Eq. (1.13) describe the physics of double exchange in the orbitally degenerate Mott-Hubbard system and the Hund's coupling to localized core spins. As in a conventional double-exchange picture, the metallic motion of charge carriers mediates a ferromagnetic interaction between neighboring sites. Strong correlations and the orbital degeneracy are expected to modulate the specific character of the magnetic exchange bonds. Specifically this leads to a softening of magnon excitations which has lately been observed in experiment [HWA98] (see Fig. 1.15). For a thorough study of this problem we refer the reader to Chap. 4.

The third term of Eq. (1.13) describes the superexchange interaction between two singly occupied sites. We emphasize that in the present model
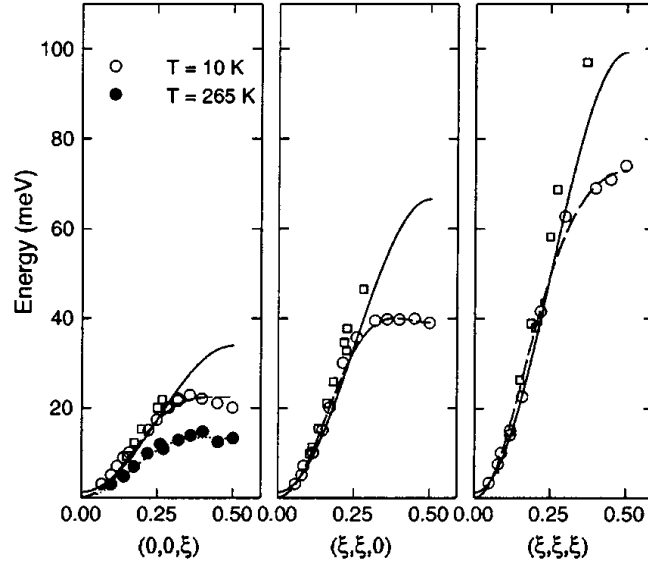
Figure 1.15: *Softening of magnon dispersion in $Pr_{0.63}Sr_{0.37}MnO_3$. The solid line is a fit to a nearest-neighbor Heisenberg model. From [HWA98].*

in which J_H is large this coupling is of *ferromagnetic* nature between spins and of *antiferro-type* between orbital pseudospins. The physics behind this term can be illustrated as follows: We write the superexchange term in the general form

$$H_J = \frac{\eta t^2}{U_1} \sum_{\langle ij \rangle_\gamma} A_{\mathrm{orb}} B_{\mathrm{spin}}, \qquad (1.14)$$

where spin and orbital dependencies have been grouped into A_{orb} and B_{spin}, respectively, and η is a yet undefined constant. First we focus on the orbital part A_{orb} (see Fig. 1.16). For a given bond along the z axis, only $d_{3z^2-r^2}$ electrons participate in superexchange processes, which is due to the vanishing transfer amplitude of $d_{x^2-y^2}$ electrons in the z direction. The presence of a strong Hund's coupling further implies that the transfer of an electron into an already occupied orbital is forbidden. Hence, bonds in the z direction contribute to the superexchange mechanism only if exactly one of the neighboring e_g electrons is in a $d_{3z^2-r^2}$ state. This requirement is enforced by the function

$$A_{\mathrm{orb}}^z = 2 \left(\frac{1}{4} - \tau_i^z \tau_j^z \right), \qquad (1.15)$$

which is equal to one if neighboring sites i and j differ in orbital quantum numbers and zero otherwise. A rotation in isospin space yields the corresponding expressions for bonds along the x and y directions. Next we
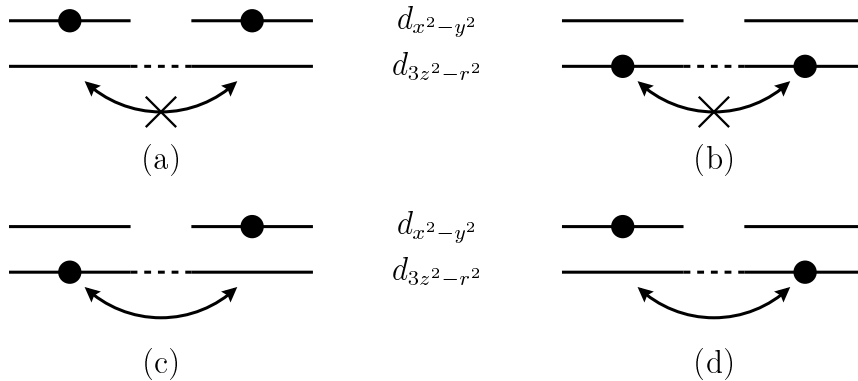
Figure 1.16: *Orbital dependence of superexchange: On a given bond along the z direction, only $d_{3z^2-r^2}$ electrons can participate in superexchange processes. Bonds with two $d_{3z^2-r^2}$ electrons as in (b) are excluded by Hund's rule.*

turn to the spin part B_{spin} [see Fig. 1.14(b)]. Since Equation (1.15) implies that superexchange processes always involve e_g electrons in distinct orbitals, Pauli's exclusion principle is inactive in the intermediate doubly occupied state. Rather the spin structure is dictated by Hund's coupling. We derive the specific form of the inter-site spin interaction starting from the general $SU(2)$-symmetric term

$$B_{\text{spin}} = \frac{\boldsymbol{S}_i \boldsymbol{S}_j + \alpha}{\beta}. \tag{1.16}$$

The constants α and β can be determined from the following two limiting cases: (1) The pair of spins at a given bond is in a high-spin configuration — Hund's coupling does not affect the exchange process; we set $B_{\text{spin}} = 1$ with $\langle \boldsymbol{S}_i \boldsymbol{S}_j \rangle = S^2$. (2) The pair of spins at a given bond is in a singlet configuration — Hund's coupling completely blocks the exchange process; hence, $B_{\text{spin}} = 0$ with $\langle \boldsymbol{S}_i \boldsymbol{S}_j \rangle = -S(S+1)$. From these considerations $\alpha = S(S+1)$ and $\beta = S(2S+1)$ follows. The overall constant $\eta = -1$ is finally obtained from the above observation that the high-spin configuration minimizes the kinetic energy and that only one e_g electron per bond participates in the exchange process.

We conclude that in an orbitally degenerate Mott-Hubbard system with strong Hund's coupling, double-exchange and superexchange processes both promote a ferromagnetic interaction between neighboring sites. The ferromagnetism encountered here is of atomic origin and is a consequence of the strong on-site repulsion between $3d$ electrons in distinct orbitals. In contrast to a conventional Mott-Hubbard system which exhibits weak ferromagnetism only for very special topologies and band fillings [KAN63], ferromagnetism is a robust feature of the orbitally degenerate model. As can be seen from the

phase diagram of $La_{1-x}Sr_xMnO_3$ in Fig. 1.1, it survives even the breakdown of metalicity at low doping concentrations. We note that antiferromagnetism in these systems evolves if the orbital degeneracy is lifted, e.g., in an orbitally ordered state. The electrons involved in the exchange process may then favor to occupy a single rather than two distinct orbitals, provided that Hund's coupling is not larger than the e_g-degeneracy splitting.

1.6   Spin Liquid in Cuprates

Taking the t-J model of Eq. (1.11) as the starting point for a description of the physics of cuprates, the formidable task of dealing with the competition between the itinerant motion of electrons and the local constraint of no double occupancy has to be approached. Since the two-dimensional system is beyond the accessibility of an exact treatment and the sheer number of electronic states puts severe limits on the system size that can be handled by numerical methods, analytic approximations are necessary. The validity of these approximations has to be checked by a comparison with experiment.

At zero doping cuprates are Mott-Hubbard insulators that turn metallic as holes are inserted into the system. It is not surprising that this correlated metallic state exhibits unconventional behavior which is most clearly manifested at low doping concentrations close to the insulating state. First to be noted is the appearance of a gap in the magnetic excitation spectrum at temperatures below a characteristic energy scale T^* (for a concise review see [LEE98]). This gap has the same d-wave symmetry as the superconducting order parameter and is often referred to as pseudogap since the weight of low-energy spin excitations vanishes by a power law. One can observe this magnetic gap in the NMR relaxation rate [TAI91, IMI93], in the magnetic susceptibility [JOH89, TAK89, NAK94, BOU96] (see Fig. 1.17), and in the specific heat [LOR93]. Furthermore, gapped features are visible in the c-axis conductivity [HOM93, TAE94], in photoemission experiments [LOE96, DIN96], and in tunneling measurements [REN98]. On the other hand, the in-plane transport properties seem to be affected only little: For instance, the coherent Drude weight of the optical-conductivity spectrum remains mostly unaltered as the spin gap opens up [UCH96].

These observations indicate that magnetic and charge sectors in underdoped cuprates are, to a certain degree, decoupled from each other. In the language of quasiparticles, the electron effectively seems to split up into two distinct entities, one carrying spin that determines the magnetic properties, the other carrying charge which controls the electric properties (see Fig. 1.18). This scheme of spin-charge separation might govern the physics inside
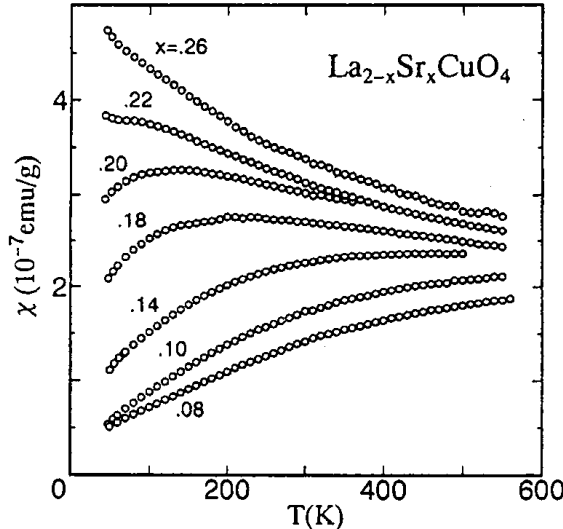
Figure 1.17: *The uniform magnetic susceptibility of underdoped $La_{2-x}Sr_xCuO_4$ declines as the temperature is lowered, reflecting the presence of a spin gap. From [NAK94].*

the CuO_2 planes, but it is clear that only physical electrons can leave the planes. Spin and charge quasiparticles then have to recombine to form an electron which explains why a gap in the magnetic channel is also expressed in photoemission and tunneling data.

We shortly note that there exist alternative approaches to explain the above experimental observations based on the existence of pre-formed electron pairs [UEM91, EME95, MEL97]. Above T_c, superconductivity is thought to be suppressed by strong phase fluctuations and/or the short coherence length of the pairing state. These models predict that manifestations of superconductivity, i.e., vanishing resistivity and diamagnetism, should be observable in short time/length-scale fluctuations even above T_c. However, recent high-frequency conductivity experiments show that the short-time phase coherence of Cooper pairs vanishes already at temperatures much below T^* [COR99, MIL99]. Furthermore, transport experiments seem to give no hint on the existence of pairs with charge $2e$ above T_c [LEE98].

From a technical point of view the notion of spin-charge separation represents a simple but powerful tool to deal with the no-double-occupancy constraint in an approximate way. The idea is to replace the fermionic electron operator by a pair of quasiparticle operators, one being of fermionic, the other of bosonic type. This can be done in two ways:

$$c_{is}^\dagger = f_{is}^\dagger b_i, \quad c_{is}^\dagger = b_{is}^\dagger f_i. \tag{1.17}$$
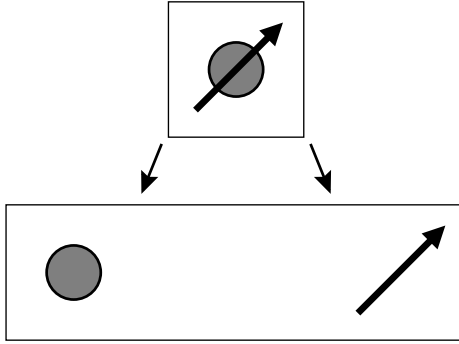
Figure 1.18: *Within the CuO_2 planes, spin and charge degrees of freedom are carried by separate quasiparticles.*

In the first case spin is carried by a fermionic quasiparticle (spinon) and charge by a "slave boson" (holon), while in the second case the spin quasiparticle is of bosonic nature and charge is assigned to a "slave fermion." In these representations the "slaved" particles take the role of counting the number of vacancies. The local constraint, which in the terms of electrons is $n_i \leq 1$, now becomes

$$n_i^f + n_i^b = 1. \tag{1.18}$$

Equation (1.18) enforces each site to be either occupied by a spin or a hole. Physically, electron and quasiparticle representations are equivalent to each other as long as no approximations are made. However, the local nature of the constraint generally prohibits an exact treatment and approximation schemes have to be employed. The problem becomes much more accessible if one allows for a relaxation of the local constraint to a global one — double occupancies are then no longer strictly forbidden, but the impact of these unphysical states should be kept as small as possible. At this point the difference between electron and quasiparticle representations emerges: While there is no straightforward way of relaxing the inequality $n_i \leq 1$ without discarding correlation effects altogether, Eq. (1.18) suggests to employ the simple average

$$\langle n_i^f \rangle + \langle n_i^b \rangle = 1, \tag{1.19}$$

which is enforced by introducing separate chemical potentials for fermions and bosons. The fundamental property of the correlated state, namely the distinction of empty and occupied sites, survives the relaxation of the constraint in this quasiparticle representation. The price to be paid is that one has to deal with an additional "slaved" particle now. We note that formally the above relaxation scheme coincides with a saddle-point approximation in a path-integral formulation [REA83]. Fluctuations around this

mean-field solution give rise to a coupling of spinons and holons via a gauge field [BAS88, IOF89, IOF90, NAG90, LEE92].

Spin-charge separation is a natural consequence of the relaxation of the local constraint: Separate quasiparticles controlling spin and charge degrees of freedom emerge from this procedure. For illustration we present here the two Hamiltonians that describe the dynamics of these spinons and holons. Employing a "slave boson" representation, we neglect for the moment the coupling between spins implied by the J term of Eq. (1.11). Introducing mean-field parameters $x = \langle b_i^\dagger b_j \rangle$, where x denotes the concentration of holes, and $\chi = \sum_s \langle f_{is}^\dagger f_{js} \rangle$, the spin and charge sectors of the Hilbert space can be decoupled, yielding

$$H_{\rm sp} = -xt \sum_{\langle ij \rangle} \sum_s \left(f_{is}^\dagger f_{js} + {\rm H.c.} \right), \qquad (1.20)$$

$$H_{\rm hl} = -\chi t \sum_{\langle ij \rangle} \left(b_i^\dagger b_j + {\rm H.c.} \right). \qquad (1.21)$$

In analogy to the Gutzwiller approach, the fermionic bandwidth gets quenched by a factor proportional to the concentration of holes. We note that the above mean-field equations describe the coherent motion of quasiparticles. In addition, fluctuations around the mean-field parameters $\langle b_i^\dagger b_j \rangle$ and $\sum_s \langle f_{is}^\dagger f_{js} \rangle$ introduce scattering events between spinons and holons.

While "slave fermion" and "slave boson" representations would both give identical results if the theory was solved exactly, they represent very different approximation schemes as soon as the constraint is relaxed. Quantum fluctuations are strong in the fermionic channel but weak in the bosonic one which has a tendency towards condensation. A "slave fermion" theory with its bosonic description of spins is therefore well suited to describe the antiferromagnetic Néel state at half filling where spin fluctuations are weak [ARO88, YOS89a, YOS89b]. On the other hand, a "slave boson" theory with its fermionic description of spin can best be applied to the spin-liquid state of underdoped cuprates which is subject to strong spin fluctuations [AND87].

We now turn to a discussion of the competition between hole mobility and spin correlations associated with the t and J term of Hamiltonian (1.11). The system can gain energy of order $\propto xt$ by allowing holes to hop, but at the same time it looses energy of order $\propto J$ due to a suppression of spin correlations. In cuprates the transfer amplitude and coupling parameter are approximately given by $t = 0.4$ eV and $J = t/3 = 0.13$ eV. At large doping concentrations $x > J/t$, the kinetic energy of holes dominates and spin correlations become unimportant. At low but finite doping levels $x \ll J/t$, the system has to accommodate the competition between hole kinetic

energy and spin correlations. It was envisioned by Anderson [AND87] that a resonance valence bond (RVB) state in which spins form a liquid of spin singlets and holes can move coherently would be a suitable choice.

The RVB state can be approximately described within mean-field theory. For this the exchange term of Eq. (1.11) is expressed in terms of fermionic spin operators using either one of the relations

$$
\begin{aligned}
\boldsymbol{S}_i \boldsymbol{S}_j &= -\frac{1}{2}\left(f_{i\uparrow}^\dagger f_{j\uparrow} + f_{i\downarrow}^\dagger f_{j\downarrow}\right)\left(f_{j\uparrow}^\dagger f_{i\uparrow} + f_{j\downarrow}^\dagger f_{i\downarrow}\right) \\
&= -\frac{1}{2}\left(f_{i\uparrow}^\dagger f_{j\downarrow}^\dagger - f_{i\downarrow}^\dagger f_{j\uparrow}^\dagger\right)\left(f_{j\downarrow} f_{i\uparrow} - f_{j\uparrow} f_{i\downarrow}\right).
\end{aligned}
\tag{1.22}
$$

This suggests to introduce the following two mean-field parameters [BAS87, AFF88a]:

$$
\begin{aligned}
\chi_{ij} &= \left\langle f_{i\uparrow}^\dagger f_{j\uparrow} + f_{i\downarrow}^\dagger f_{j\downarrow}\right\rangle, \\
\Delta_{ij} &= \left\langle f_{j\downarrow} f_{i\uparrow} - f_{j\uparrow} f_{i\downarrow}\right\rangle.
\end{aligned}
\tag{1.23}
$$

At half filling, the two decoupling schemes are equivalent to each other which follows from a local $SU(2)$ symmetry originating in the equivalence of the presence of an up-spin and the absence of a down-spin [AFF88b, WEN96]. Away from half filling this symmetry is broken and χ_{ij} and Δ_{ij} become distinguished parameters. Furthermore, the local gauge invariance of electron operators $c_{is}^\dagger \to \exp(i\Theta_i)c_{is}^\dagger$ implies the mean-field parameters to carry a phase. A priori, this phase is undefined and has to be chosen such as to minimize the free energy and/or to most closely resemble the experimental situation. Various different choices have been discussed; the ones most commonly used are: (1) *Uniform phase* — the bond parameter is real and invariant under translation and rotation. (2) *d-wave symmetric phase* — the bond parameter is real and invariant under translation but changes sign under a rotation by 90°.

Within the present mean-field picture of cuprates the spin gap can be considered as a precursor of superconductivity. The formation of spin singlets establishes coherency in the spin sector, while coherency in the charge sector is still lacking. The road to superconductivity can be described by a three-step process [FUK88, KOT88b, SUZ88, FUK92]: First, coherent motion of spinons is established as $\chi_{ij} \neq 0$ with a uniform phase. Second, a gap opens in the spinon spectrum as $\Delta_{ij} \neq 0$ which anticipates the d-wave symmetry of the superconducting order parameter. Third, coherence in the charge sector develops as holons undergo a Bose condensation, giving rise to a non-vanishing amplitude of $\langle b_i \rangle$. The simultaneous presence of Δ_{ij} and $\langle b_i \rangle$ finally yields a finite pairing amplitude of real electrons $\langle c_{i\uparrow} c_{j\downarrow} \rangle$ and hence
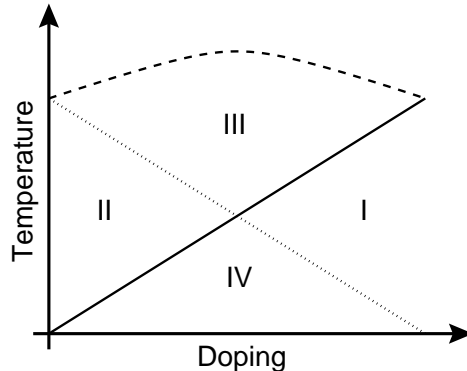
Figure 1.19: *Schematic mean-field phase diagram of cuprates. Below the dashed line, spin-singlet correlations are finite as $\chi_{ij} \neq 0$. Dotted and solid lines associated with mean-field parameters Δ_{ij} and $\langle b \rangle$ divide this region into four sections: (I) Fermi-liquid phase, (II) spin-gap phase, (III) strange-metal phase, and (IV) superconducting phase.*

superconductivity. Depending on the doping concentration, the above order of steps may change; the complete mean-field phase diagram is schematically shown in Fig. 1.19.

The strength of the RVB mean-field theory lies in the description of the spin-liquid features of underdoped cuprates. The transition to a superconducting state by a Bose condensation of holons, however, is unsatisfactory in many respects and remains an unsolved mystery. Since the mechanism of high-T_c superconductivity is believed to be intimately related to the unusual magnetic properties of the normal state, a better understanding of the latter seems to be a natural approach to superconductivity. One of the most challenging open problems in this respect is to reconcile the gaplike features reminiscent of a spin liquid with the presence of antiferromagnetic correlations that signal the closeness of the system to a spin-ordered Néel state (see Fig. 1.20). Insight into the nature of these anomalous features can be gained by NMR experiments that measure the effect of impurities in the magnetically active CuO_2 planes. On the theoretical side, there is need for a unifying picture of impurities with and without internal spin structure. To cover the multifaceted nature of magnetism in cuprates, it is necessary to go beyond a simple mean-field description in order to compensate for a severe underestimation of local AF correlations in the RVB picture. For a detailed study of these questions we refer the reader to Chap. 2.
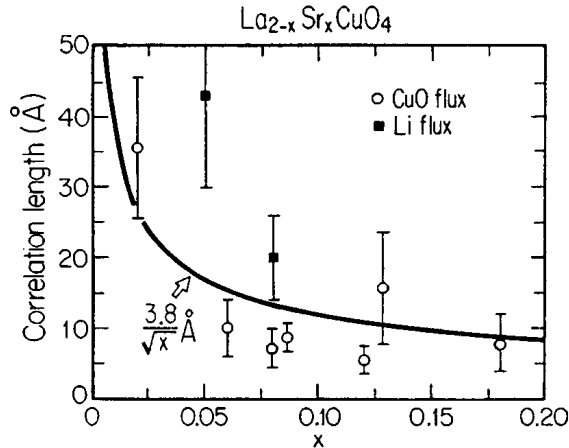
Figure 1.20: *Change of the AF correlation length with doping in* $La_{2-x}Sr_xCuO_4$. *From [BIR88].*

1.7   Orbital Liquid in Manganites

The strong on-site repulsion between $3d$ electrons has a pronounced effect on the properties of the metallic state in cuprates as was discussed in the previous section. It is interesting to see if the same holds true for the metallic state of manganites. This is not obvious from the beginning for the following reason: The ferromagnetic moment of metallic manganites is close to being completely saturated at low temperatures. Electrons move within a fully spin-polarized band and can effectively be considered as spinless fermions. One could then be inclined to think that Pauli's exclusion principle renders the on-site Hubbard interaction ineffective by prohibiting all double occupancies for quantum statistical reasons. The system should thus resemble a simple, non-correlated spin-polarized metal. However, experiment indicates this not to be the case: As in cuprates, the metallic state of manganites seems to be subject to strong correlations as will be discussed below. In order for the on-site repulsion to become effective, some new degree of freedom has to adopt the role of the strongly fluctuating spins in cuprates. Recently it was suggested by Ishihara, Yamanaka, and Nagaosa [ISH97a, NAG98] that this degree of freedom could be found in the orbital degeneracy of manganites. An orbital-liquid state characterized by strong orbital fluctuations was proposed as counterpart to the spin-liquid state of cuprates.

Experimentally there are clear indications that orbital fluctuations are strong in metallic manganites: First, anisotropies are neither detected in the conductivity nor in spin excitations which rules out a long-range orbitally ordered state [ISH97a]; analogously, cooperative distortions of oxygen ions
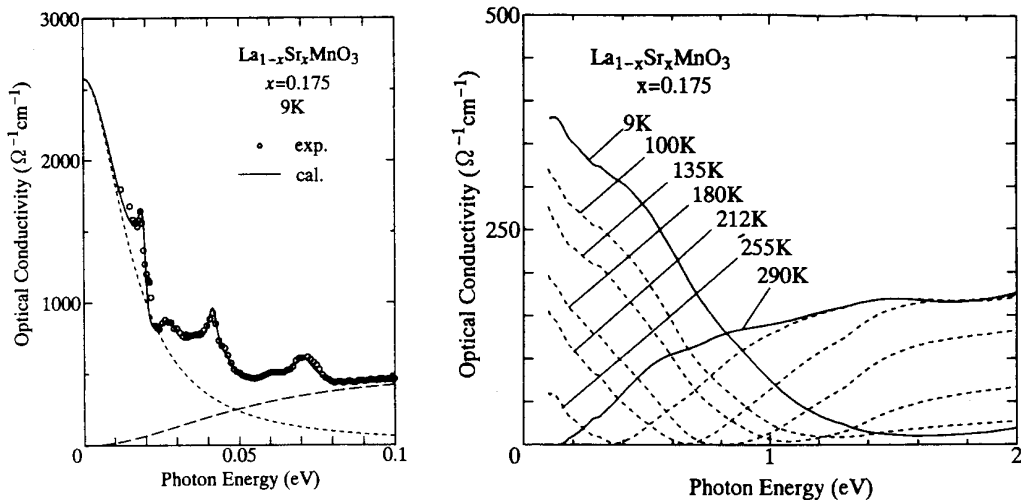
Figure 1.21: *Optical conductivity in $La_{0.825}Sr_{0.175}MnO_3$: Drude peak (left) and incoherent spectrum (right). Only the temperature-dependent part is shown on the right. From [OKI97], [OKI95].*

have not been observed by neutron scattering [ISH97a]. Second, local distortions of the MnO_6 octahedra that show up in neutron and X-ray data at temperatures above T_C vanish in the metallic state below T_C which rules out distortions even on a local scale [BIL96, BOO98, LAN98] (see Fig. 1.10). The potential energy gain due to a lifting of the e_g degeneracy hence seems to be more than compensated by the loss of kinetic energy implied by the constriction of charge motion in the non-degenerate system.

The metallic state of manganites exhibits several anomalous features that carry the fingerprint of strong correlations. The most important ones are: Photoemission spectra show only a small discontinuity at the Fermi level [CHA93, SAI95, SAR96]. This indicates that electronic quasiparticles have only a small weight. Particularly striking are recent measurements of the optical conductivity [OKI95, OKI97] (see Fig. 1.21). These show a strong suppression of the Drude weight accompanied by a broad incoherent spectrum extending up to ≈ 1 eV. This contrasts the behavior of a conventional metal in which the spectral weight accumulates mostly in the Drude peak at low temperatures. The rather high energies to which the incoherent part of the spectrum extends implies the presence of a scattering mechanism that is of electronic, not phononic origin. Employing the above picture of an orbital liquid, we are able to identify the interplay between orbital fluctuations and strong on-site repulsion between $3d$ electrons as the cause for the incoherent transport properties as is shown in Chap. 3. We further demon-

strate that there is no conflict between a strong-correlation description of manganites and the small values of specific heat observed experimentally [OKI95, OKI97, WOO97, OKU98].

Technically, the orbital-liquid state is to be regarded as an analytical tool to handle the strongly correlated nature of metallic manganites. In analogy to our previous discussion on spin liquids, one replaces the electron operators of the t-J model (1.13) by a set of auxiliary quasiparticle operators:

$$c_{is\alpha}^\dagger = f_{is\alpha}^\dagger b_i, \quad c_{is\alpha}^\dagger = b_{is\alpha}^\dagger f_i. \tag{1.24}$$

In the former representation, spin and orbital indices s and α are carried by a fermion and charge by a "slave boson," while the order is reversed in the latter "slave fermion" representation. The spin index can further be separated from the orbital one by introducing Schwinger bosons d_{is}

$$f_{is\alpha}^\dagger = f_{i\alpha}^\dagger d_{is}^\dagger, \quad b_{is\alpha}^\dagger = b_{i\alpha}^\dagger d_{is}^\dagger, \tag{1.25}$$

with the spin representation [AUE94]

$$s_i^+ = d_{i\uparrow}^\dagger d_{i\downarrow}, \quad s_i^- = d_{i\downarrow}^\dagger d_{i\uparrow}, \quad s_i^z = \frac{1}{2}(d_{i\uparrow}^\dagger d_{i\uparrow} - d_{i\downarrow}^\dagger d_{i\downarrow}), \tag{1.26}$$

and $d_{i\uparrow}^\dagger d_{i\uparrow} + d_{i\downarrow}^\dagger d_{i\downarrow} = 1$. The no-double-occupancy constraint

$$n_i^f + n_i^b = 1 \tag{1.27}$$

enforces that each site is either occupied by an orbital-carrying quasiparticle (orbiton) or by a charge-carrying one (holon). With the relaxation of the local constraint to a global one an orbital-charge separation scheme emerges (see Fig. 1.22). We illustrate this for the case of a "slave-boson" representation. For simplicity the ferromagnetic moment is assumed to be completely saturated and all spin fluctuations are discarded — this allows to drop the spin indeces altogether. Introducing mean-field parameters $x = \langle b_i^\dagger b_j \rangle$ for the concentration of holes and $\chi = t^{-1} \sum_{\alpha\beta} t_\gamma^{\alpha\beta} \langle f_{i\alpha}^\dagger f_{j\beta} \rangle$, the following two Hamiltonians for orbitons and holons are obtained:

$$H_{\rm orb} = -x \sum_{\langle ij \rangle_\gamma} t_\gamma^{\alpha\beta} \left(f_{i\alpha}^\dagger f_{j\beta} + {\rm H.c.} \right), \tag{1.28}$$

$$H_{\rm hl} = -\chi t \sum_{\langle ij \rangle} \left(b_i^\dagger b_j + {\rm H.c.} \right). \tag{1.29}$$

We note that the composite nature of the electron, i.e., the fact that two quasiparticles together form an electron, induces strong scattering between
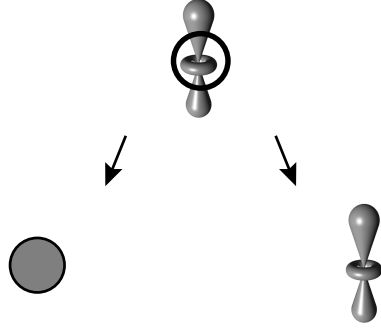
Figure 1.22: *Orbital and charge degrees of freedom are carried by separate quasiparticles.*

holons and orbitons. To account for this effect it is necessary to go beyond the mean-field theory presented here and to consider fluctuations in the parameters $x = \langle b_i^\dagger b_j \rangle$ and $\chi = t^{-1} \sum_{\alpha\beta} t_\gamma^{\alpha\beta} \langle f_{i\alpha}^\dagger f_{j\beta} \rangle$. These scattering events play an important role in the analysis presented in Chaps. 3 and 4.

To finish the discussion we shortly comment on the applicability of the two types of representations introduced in Eq. (1.24): A fermionic representation of the orbital sector is suitable for describing a disordered, strongly fluctuating orbital state, but the instability of orbitals to order (e.g., via Jahn-Teller coupling) is ad hoc underestimated. On the other hand, a bosonic description of the orbital sector accounts well for an orbitally ordered state and the low-energy orbital excitations around it. The inclination of bosons to condense, however, now overestimates the robustness of the ordered state. The picture of an orbital liquid, both in its "slave boson" and "slave fermion" form, is extensively employed in Chaps. 3 - 5 to model various aspects of metallic manganites.

Chapter 2

Impurity-Induced Moments in Underdoped Cuprates

2.1   Introduction

The simultaneous occurrence of a gap in the magnetic excitation spectrum and the persistence of local antiferromagnetic correlations mark the scope of magnetism in underdoped cuprates. Besides being interesting for their own virtue, these anomalous properties of the normal state are believed to be closely related to the mechanism of high-T_c superconductivity. Experimentally, the local magnetic structure of cuprates can be sensitively probed by doping the CuO_2 planes with impurities and subsequently measuring the response of the NMR signal of nuclei coupled to the planes. In this chapter, we present a theory of magnetic ($S = 1$) and non-magnetic ($S = 0$) impurities in underdoped cuprates that unifies the existence of the spin gap with the presence of antiferromagnetic (AF) correlations and accounts for the peculiarities observed in NMR experiments.

When doping high-T_c cuprates with impurities, Cu (d^9) with an effective in-plane spin of $S = \frac{1}{2}$ is commonly replaced by Ni (d^8) with $S = 1$ or Zn/Al (d^{10}) with $S = 0$. In the spin-gap phase at low hole concentrations, either type of impurity is experimentally observed to induce $S = \frac{1}{2}$ magnetic moments [XIA87, FIN90, ALL91, ISD93, ZHE93, MAN94, MEN94, RIS94, ISD96, BOB97a, BOB97b, MEN99]. This is a very interesting observation as it obviously shows that the magnetic behavior of impurities can be understood only in connection with the magnetic response of CuO_2 planes: In the case of non-magnetic impurities, the moments seen in experiment must be contributed to by the host. Similarly, magnetic moments of the CuO_2 planes must be active in partially screening the $S = 1$ spin of magnetic impurities.
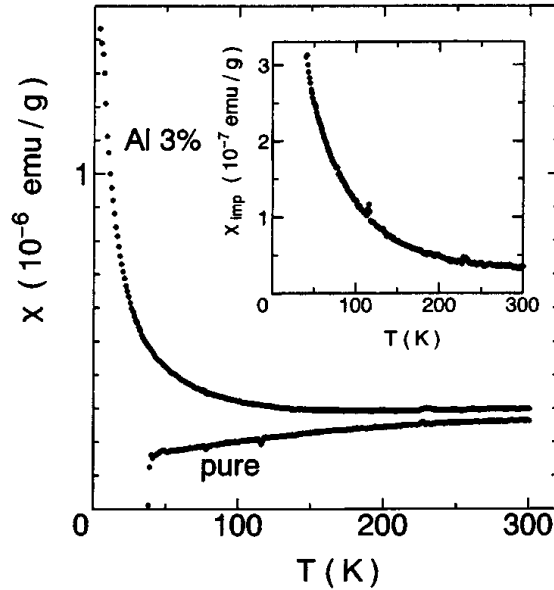
Figure 2.1: *Susceptibility of $La_{1.85}Sr_{0.15}CuO_4$: Pure and Al-doped (S = 0) system (inset: impurity contribution only). From [ISD96].*

Figure 2.1 illustrates the formation of magnetic moments due to doping with non-magnetic Al impurities: In the pure sample the static spin susceptibility follows a thermally activated behavior, reflecting the spin-singlet nature of the ground state. Doping with impurities adds a pronounced Curie component. Another interesting experimental observation is that of the local nature of impurity moments. Most convincingly this can be seen in the appearance of satellite peaks in the NMR signal, e.g., of ^{89}Y in $YBa_2Cu_3O_{7-y}$ (see Fig. 2.2). These satellites are associated with ^{89}Y nuclei that lie close to an impurity; the local field of the impurity-induced moments shifts the NMR resonance frequency, while nuclei at large distance remain unaffected. This results in a splitting of the NMR signal into distinct lines.

Our study of impurities in cuprates is, to a large extent, motivated by the following peculiar experimental findings: Superconducting quantum interference device (SQUID) measurements of the macroscopic susceptibility reveal an almost perfect T^{-1} Curie behavior of the moments associated with non-magnetic Zn and magnetic Ni impurities [MEN94]. This seems to be in apparent contradiction to recent NMR measurements on ^{17}O for the underdoped compound $YBa_2Cu_3O_{6.6}$ [BOB97a, BOB97b] [see Fig. 2.3(a)]. The polarization of Cu spins in the presence of Zn or Ni leads to a broadening of the NMR line. In contrast to the aforementioned SQUID measurement, the linewidth displays a marked non-Curie behavior. To resolve this con-
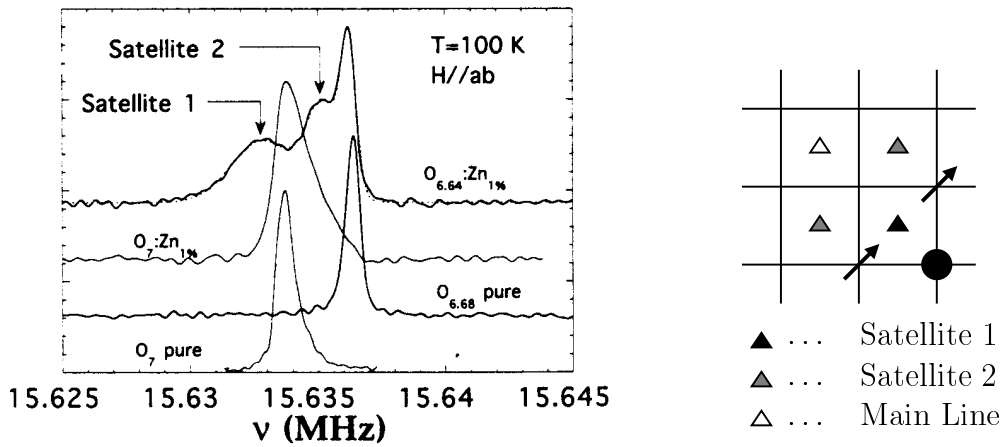
Figure 2.2: *Non-magnetic Zn impurities in $YBa_2Cu_3O_{7-y}$: The impurity (filled circle in the right figure) induces moments predominantly on nearest-neighbor Cu sites (arrows), leading to a splitting of the NMR signal of ^{89}Y (triangles) into a main and two satellite peaks (left). From [MAN94] (left).*
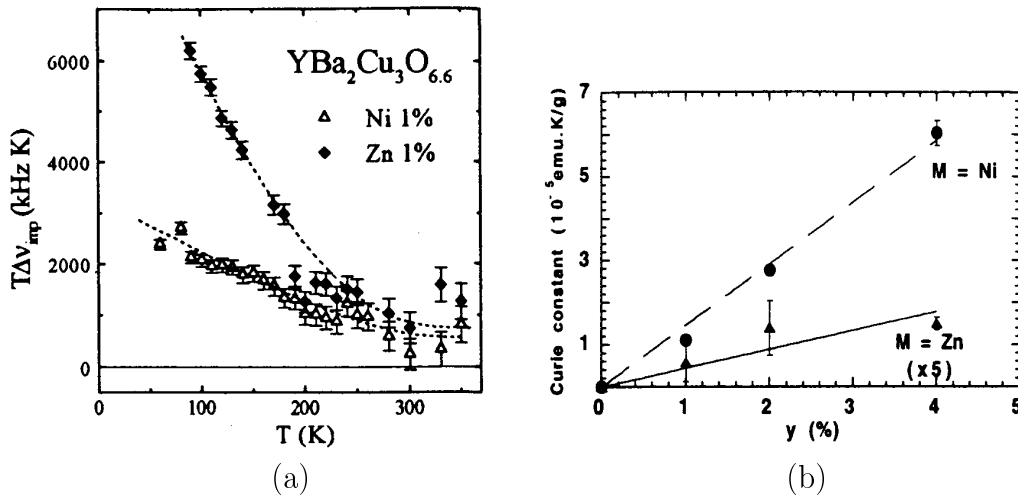
Figure 2.3: *Zn- ($S = 0$) and Ni- ($S = 1$) doped $YBA_2Cu_3O_{7-y}$: (a) Impurity-induced NMR line broadening. (b) Curie constant of the macroscopic susceptibility by SQUID. From [BOB97b], [MEN94].*

tradiction one is led to adopt an inherent temperature dependence of the polarizability of CuO_2 planes. Morr, Akimoto, Nakamur, *et al.* [MRR98] suggested to interpret this behavior of the polarizability in terms of a temperature dependence of the AF correlation length. We will later elaborate on this view. Still another interesting observation can be made by comparing the two experiments: While the NMR study shows non-magnetic Zn to have a more pronounced effect on the linewidth than Ni, the macroscopic susceptibility reveals a reversed effect [see Fig. 2.3(b)]. Since the NMR experiment is sensitive to a spatial variation of the spin polarization, a very different shape of the spin density induced by the two types of impurities can be inferred.

In the following, we present a microscopic theory of moments induced by magnetic and non-magnetic impurities in the spin-gap phase of underdoped cuprates. We analyze the different nature of coupling between Cu and impurity spins and derive expressions for the local spin polarization of CuO_2 planes. The presence of the spin gap and of short-range AF correlations is shown to strongly modify the conventional Ruderman-Kittel-Kasiya-Yosida (RKKY) picture. Finally, we derive expressions for the NMR Knight shift and line broadening which account well for the peculiarities of experimental data.

2.2   Impurity Model

The relevant physics of the CuO_2 planes of high-T_c cuprates is believed to be described by the large-U Hubbard or t-J model. The dualism between itinerant charge motion and local electron interaction that is inherent to these models can, in an approximate way, be captured by introducing separate quasiparticles for spin and charge degrees of freedom (see Chap. 1). Within this picture the normal state of underdoped cuprates is viewed as a phase in which spins form singlet pairs while coherence between holes that would eventually lead to superconductivity has not yet been established. We follow this line of thinking but restrict ourselves to the magnetic sector of the Hilbert space. Our starting point is the spin-$\frac{1}{2}$ AF Heisenberg model on a square lattice:

$$H = J \sum_{\langle ij \rangle} \boldsymbol{s}_i \boldsymbol{s}_j. \qquad (2.1)$$

Keeping in mind the presence of itinerant holes which prevent the system from developing long-range magnetic order, we treat this Hamiltonian within resonance valence bond (RVB) mean-field theory [AND87] — this accounts well for the spin-liquid features of cuprates. Relaxing the local no-double-occupancy constraint to a global one and introducing mean-field bond para-
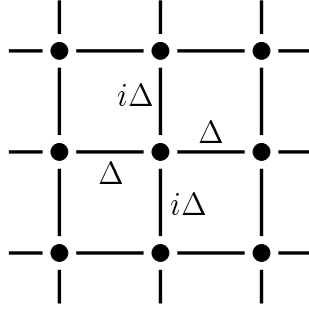
Figure 2.4: *Symmetry of the bond-order parameter in the flux phase.*

meters

$$\Delta_{ij} = \Delta_{\boldsymbol{\delta}} = J \sum_s \langle f_{js}^\dagger f_{is} \rangle^0, \tag{2.2}$$

the following mean-field Hamiltonian is obtained:

$$H_{\mathrm{RVB}} = - \sum_{\langle ij \rangle s} \left(\Delta_{ij} f_{is}^\dagger f_{js} + \mathrm{H.c.} \right). \tag{2.3}$$

The expectation value $\langle \ldots \rangle^0$ in Eq. (2.2) refers to Hamiltonian (2.1) of the impurity-free system. Original spin operators $\boldsymbol{s}_i$ have been expressed in terms of fermionic operators by $\boldsymbol{s}_i = \frac{1}{2} \sum_{ss'} \boldsymbol{\sigma}_{ss'} f_{is}^\dagger f_{is'}$ with Pauli matrix vector $\boldsymbol{\sigma} = (\sigma^x, \sigma^y, \sigma^z)$. We note that our approach considers the presence of holes only in an implicit manner: The above fermionic representation of spin excitations implies strong spin fluctuations. It is therefore not a suitable representation of the spin-ordered ground state of the 2D Heisenberg model but rather of a spin liquid. The latter is implied to be stabilized by the motion of holes in the hole-doped system studied here.

The phase of the mean-field bond parameter in Eq. (2.2) is yet undetermined and has to be chosen such as to resemble the experimental situation most closely. An appropriate choice for the spin-gap regime is the flux phase [AFF88a, SUZ88, KOT88a, MAS89, MAS99] (see Fig. 2.4):

$$\Delta_{\pm x} = i \Delta_{\pm y} \equiv \Delta. \tag{2.4}$$

Dividing the lattice into two sublattices A and B and going to the momentum representation, Hamiltonian (2.3) can be diagonalized

$$H_{\mathrm{RVB}} = \sum_{\boldsymbol{k}\nu} \xi_{\boldsymbol{k}}^\nu f_{\boldsymbol{k}\nu}^\dagger f_{\boldsymbol{k}\nu}, \tag{2.5}$$

with index $\nu = \pm$. The spectrum of spin excitations or spinons is

$$\xi_{\boldsymbol{k}}^\pm = \pm 2\Delta \left(\cos^2 k_x + \cos^2 k_y \right)^{1/2}.$$
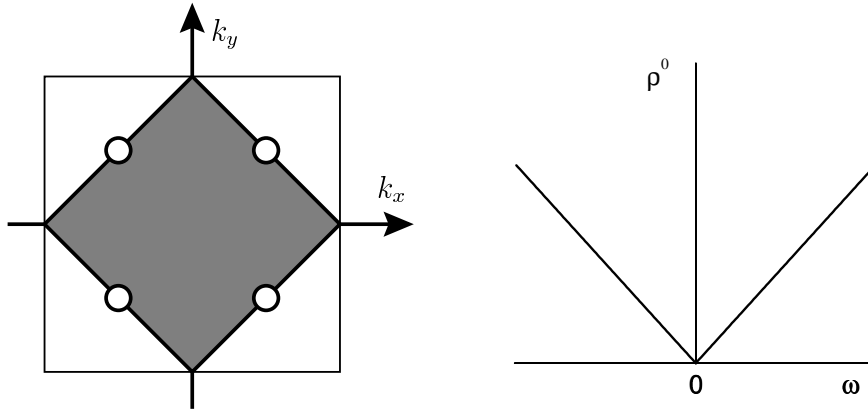
Figure 2.5: _The spinon excitation spectrum has four nodes at $(\pm\frac{\pi}{2}, \pm\frac{\pi}{2})$ that lie at the spinon chemical potential, yielding a V-shaped pseudogap in the density of states of magnetic excitations._

It has nodes at $(\pm\frac{\pi}{2}, \pm\frac{\pi}{2})$, yielding a V-shaped pseudogap in the density of states centered at the spinon chemical potential $\mu_s = 0$ (see Fig. 2.5):

$$\rho^{(0)}(\omega) = \frac{|\omega|}{D^2}. \tag{2.6}$$

The latter is defined per spin up/down state, and $D = 2\sqrt{\pi}\Delta$ denotes the spinon half bandwidth. We note that despite the fact that the mean-field Hamiltonian (2.3) is a single-particle one, it incorporates important aspects of a many-particle system: The pseudogap in the spin excitation spectrum is a consequence of the inter-site coupling between neighboring spins, which establishes a finite amplitude of singlet correlations across nearest-neighbor bonds. The resonating structure of the bonds makes this a many-particle effect.

To simulate first a non-magnetic impurity we introduce into Hamiltonian (2.3) a local chemical potential V acting on site $\boldsymbol{R} = 0$, which by convention lies on sublattice A. In the limit $V \to \infty$, spinons are expelled from this site, creating a vacancy. The Hamiltonian is then

$$H_{\mathrm{Zn}} = H_{\mathrm{RVB}} + V \sum_s f_{0s}^\dagger f_{0s}|_{V\to\infty}. \tag{2.7}$$

To describe a magnetic Ni impurity, we insert into the empty site an impurity spin $\boldsymbol{S}_0$ with $S = 1$ which is coupled antiferromagnetically to the surrounding Cu spins $\boldsymbol{s_\delta}$. The corresponding Hamiltonian is

$$H_{\mathrm{Ni}} = H_{\mathrm{RVB}} + V \sum_s f_{0s}^\dagger f_{0s}|_{V\to\infty} + J' \sum_\delta \boldsymbol{S}_0 \boldsymbol{s_\delta}. \tag{2.8}$$

In the following we study the impact of impurities upon the properties of the spin-liquid state. Different theoretical aspects of non-magnetic impurities in spin-gap systems have been investigated by several authors [BAL95, NAG95, NAG96, MAR97, NAG97, PEP98].

2.3   Local Magnetic Moments

Doping with static impurities breaks the translational invariance of the system and induces scattering of spinons on the impurity sites. Without spin-singlet correlations, the presence of an impurity would simply lead to a spatial redistribution of the spinon density in the form of Friedel-like oscillations. The situation is expected to change dramatically as singlet correlations between spins are taken into account and the spin gap opens. Intuitively, removing one spin from a liquid of spin singlets leaves another spin unpaired. Supposably this unpaired spin will modify the magnetic properties of the system. In the first part of this section we show that a non-magnetic impurity indeed alters the spin-singlet nature of the ground state by contributing a Curie-like component to the spin susceptibility. We then extend our study to a magnetic impurity. Here we observe a Kondo-like screening of the internal impurity spin by moments on neighboring Cu sites, leading to a quenching of the impurity moment.

2.3.1   Non-Magnetic Impurity

It is convenient to introduce propagators to describe the itinerant motion of spinons. In the pure and impurity-doped system, respectively, these are

$$
\begin{aligned}
g_\lambda^{(0)}(i\omega) &= -\langle T_\tau f_\lambda(\tau) f_\lambda^\dagger(0)\rangle_{i\omega}^0 = \frac{1}{i\omega - \xi_\lambda}, \\
g_{\lambda\lambda'}(i\omega) &= -\langle T_\tau f_\lambda(\tau) f_{\lambda'}^\dagger(0)\rangle_{i\omega},
\end{aligned}
\tag{2.9}
$$

where we use the simplified notation $\lambda = (\boldsymbol{k}, \nu)$ and Matsubara frequencies $i\omega = i(2n + 1)\pi T$ with temperature T and integer numbers n. The propagators of Eqs. (2.9) can be related by a scattering matrix $T_{\lambda\lambda'}$ that describes successive scattering of spinons on the impurity site (see Fig. 2.6):

$$
g_{\lambda\lambda'}(i\omega) = g_\lambda^{(0)}(i\omega)\delta_{\lambda\lambda'} + g_\lambda^{(0)}(i\omega)T_{\lambda\lambda'}(i\omega)g_{\lambda'}^{(0)}(i\omega).
\tag{2.10}
$$

In the limit of an infinitely large repulsive potential V on the impurity site, the scattering matrix is
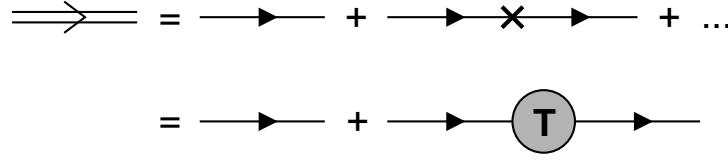
Figure 2.6: *The scattering matrix (circle) describes successive scattering of free spinons (single arrows) on a local potential (cross). The spinon propagator of the impurity-doped system is denoted by a double arrow.*

$$T^{\mathrm{Zn}}_{\lambda\lambda'} = \frac{V\delta_{\lambda\lambda'}}{1 - VG^{(0)}(i\omega)} = -\frac{\delta_{\lambda\lambda'}}{G^{(0)}(i\omega)} \tag{2.11}$$

where $G^{(0)}(i\omega) = \sum_\lambda g^{(0)}_\lambda(i\omega)$ is the k-integrated Green's function of the pure system

$$G^{(0)}(i\omega) = -\frac{2i\omega}{D^2}\ln(D/|\omega|). \tag{2.12}$$

The important point is that $G^{(0)}(i\omega)$ vanishes at zero frequency due to the presence of a spin gap. The scattering matrix of Eq. (2.11) then acquires a pole at $\omega = 0$. In the spinon density of states this pole is reflected by a δ function situated in the center of the pseudogap:

$$\delta\rho_{\mathrm{Zn}}(\omega) = \delta(\omega). \tag{2.13}$$

The latter expression, which is valid for $\omega \ll D$, is calculated from the impurity part of the k-integrated Green's function $\delta G(i\omega) = \sum_{\lambda\lambda'} g^{(0)}_\lambda(i\omega)T_{\lambda\lambda'}g^{(0)}_{\lambda'}(i\omega)$ given by

$$\delta G_{\mathrm{Zn}}(i\omega) = \frac{\partial}{\partial i\omega}\ln[G^{(0)}(i\omega)] = \frac{1 - \ln^{-1}(D/|\omega|)}{i\omega}. \tag{2.14}$$

Equation (2.14) is related to the impurity contribution to the spinon density of states by $\delta\rho(\omega) = -\frac{1}{\pi}\mathrm{Im}[\delta G(i\omega \to \omega + i0^+)]$. Figure 2.7 schematically shows the spectral densities $\rho^{(0)}(\omega)$ and $\rho(\omega) = \rho^{(0)}(\omega) + \delta\rho(\omega)$ of the pure and the impurity-doped system.

As a consequence of the finite spectral weight induced inside the gap, the static spin susceptibility $\chi(T) = \sum_{\boldsymbol{RR'}}\langle T_\tau s^z_{\boldsymbol{R}}(\tau)s^z_{\boldsymbol{R'}}(0)\rangle_{\omega=0}$ no longer vanishes as $\propto T$ at low temperatures. Rather, employing[1]

$$\chi(T) = \frac{1}{4T}\int_{-\infty}^{\infty} dx \frac{\rho(x)}{\cosh^2(x/2T)} \tag{2.15}$$

---

[1]Susceptibilities are corrected by a factor of 2 to compensate for an underestimation in the present mean-field treatment. The use of a Majorana fermion representation [MTT81, TSV92, KRI95] as employed in Ref. [KHA97b] makes this correction unnecessary.
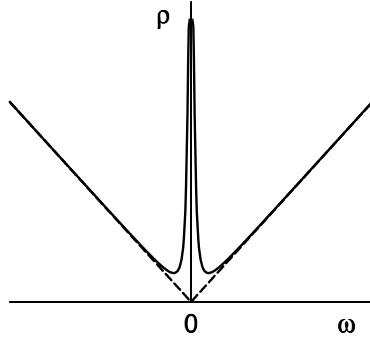
Figure 2.7: *Schematic plot of the spinon density of states for the system with a non-magnetic impurity (solid line) as compared to the pure system (dashed line). The δ function is artificially broadened.*

Figure 2.8: *Diagrammatic representation of the static spin susceptibility.*

(see Fig. 2.8), a new term appears in the susceptibility; at $T \ll D$, this impurity contribution resembles the behavior of a free spin-$\frac{1}{2}$:

$$\delta\chi_{\text{Zn}}(T) = \frac{1}{4T}. \tag{2.16}$$

Instead of dissolving into the RVB ground state, the unpaired spin created by the substitution of Cu by Zn is hence found to actively contribute to the magnetic behavior of the system. We note that fluctuations of spin-singlet correlations are strong in the RVB state. This tends to weaken the stability of the localized spinon state by "smearing" its position: The resonating structure of singlet pairs allows an unpaired spin to recombine with a new partner, thus leaving its original partner without counterpart. Due to the short-ranged nature of singlet correlations, this effect is not strong enough to prevent the bound state from evolving. Yet, one can expect the impurity moment to be rather broadly distributed over a large number of lattice sites. In the following we analyze this question by studying the spatial distribution of the impurity-induced moment.

   First we investigate the impurity contribution to the local density of states. The latter can be obtained from the impurity part of the local Green's function $\delta G^{\boldsymbol{R}}(i\omega) = \sum_{\lambda\lambda'} g_\lambda^{(0)} T_{\lambda\lambda'} g_{\lambda'}^{(0)} e^{i(\boldsymbol{k}-\boldsymbol{k}')\boldsymbol{R}}$ which describes the propagation of a spinon starting from and returning to site $\boldsymbol{R}$. In the impurity-doped system this quantity depends upon the relative position of the impurity. This

can be seen by expressing $\delta G^{\boldsymbol{R}}(i\omega)$ in terms of the inter-site Green's function of the pure system $G^{(0)}(i\omega, \boldsymbol{R}) = -\langle T_\tau f_{0s}(\tau) f^\dagger_{\boldsymbol{R}s}(0)\rangle^0_{i\omega}$ which yields

$$\delta G^{\boldsymbol{R}}_{\mathrm{Zn}}(i\omega) = -\frac{G^{(0)}(i\omega, \boldsymbol{R})G^{(0)}(i\omega, -\boldsymbol{R})}{G^{(0)}(i\omega)}. \tag{2.17}$$

The denominator of Eq. (2.17) describes the propagation of a free spinon from site $\boldsymbol{R}$ to site 0 and back to site $\boldsymbol{R}$, while the nominator accounts for the scattering of spinons on the impurity at site 0. At this point the sublattice structure evolves [see Eqs. (2.4) and (2.5)]: The inter-site Green's function assumes different forms depending on whether it connects two points on the same or on different sublattices. Explicitly,

$$G^{(0)}(i\omega, \boldsymbol{R}) = \begin{cases} -\dfrac{2i|\omega|}{D^2}\varphi_A(\boldsymbol{R}) K_0(R|\omega|/D) & \text{for} \quad \boldsymbol{R} \in A, \\[2ex] -\dfrac{2i|\omega|}{D^2}\varphi_B(\boldsymbol{R}) K_1(R|\omega|/D) & \text{for} \quad \boldsymbol{R} \in B, \end{cases} \tag{2.18}$$

with a modified Bessel functions of the second kind $K_\nu(x)$ and $R \neq 0$. The angular dependence is determined by the phase factors

$$\varphi_A(\boldsymbol{R}) = \frac{1}{2}\left(e^{i\pi R^+/2} + e^{i\pi R^-/2}\right), \tag{2.19}$$

$$\varphi_B(\boldsymbol{R}) = \frac{1}{2}\left(\tilde{R}^+ e^{i\pi R^+/2} + \tilde{R}^- e^{i\pi R^-/2}\right), \tag{2.20}$$

with $R^\pm = R_x \pm R_y$ and $\tilde{R}^\pm = (R_x \pm iR_y)/R$.

We are now in the position to evaluate the local Green's function, Eq. (2.17), using the above expressions for $G^{(0)}(i\omega, \boldsymbol{R})$. From this we then calculate the impurity part of the local density of states, $\delta\rho^{\boldsymbol{R}}(\omega) = -\frac{1}{\pi}\mathrm{Im}[\delta G^{\boldsymbol{R}}(i\omega \to \omega + i0^+)]$. The first important observation to be made is that contributions from sublattice A are negligibly small; the impurity induces moments predominantly on sublattice B which comprises, e.g., the sites adjacent to the impurity. The spatial distribution of the moments on this sublattice is described by the impurity contribution to the local density of states

$$\delta\rho^{\boldsymbol{R}}_{\mathrm{Zn}}(\omega) = \frac{1}{\pi}\frac{1}{|\omega|\ln^2(D/|\omega|)}\frac{\Phi_B(\boldsymbol{R})}{R^2} \quad \text{for} \quad \boldsymbol{R} \in B, \tag{2.21}$$

which is valid for $R|\omega| \ll D$. The phase factor is $\Phi_B(\boldsymbol{R}) = |\varphi_B(\boldsymbol{R})|^2 = \frac{1}{2}[1-(2R_x^2/R^2-1)\cos(\pi R_x)]$. As expected from the above general arguments, the moment is found to be broadly distributed over Cu sites, its density falling off rather slowly as $\propto R^{-2}$ with distance from the impurity. The peculiar
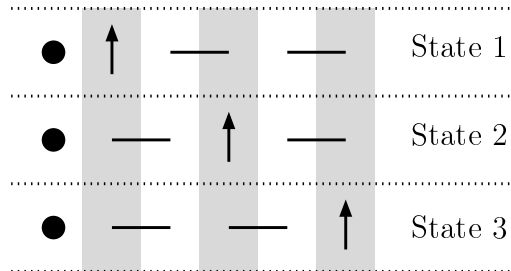
Figure 2.9: *Schematic view of spin propagation in the RVB state via the exchange of a singlet partner. The unpaired spin is denoted by an arrow, nearest-neighbor RVB singlets by horizontal lines, and the impurity by a dot. Only one spatial dimension is shown. Shaded and non-shaded sites belong to different sublattices.*

sublattice structure encountered here follows from the specific mechanism by which unpaired spins propagate through the RVB state: As mentioned above, an unpaired spin can be absorbed into the RVB ground state by forming a singlet with a new partner which simultaneously creates an unpaired spin at a different site. Since nearest-neighbor singlet correlations dominate, this mechanism preserves the sublattice label of the propagating spin to leading order (see Fig. 2.9). We finally note that the logarithmic structure which appears in the local density of states is characteristic for a disordered spin-gap system. The reason why it is not seen in the macroscopic spin susceptibility of the bound state [see Eq. (2.16)] is that the latter is effectively decoupled from the spinon system — to leading order, it behaves as a free spin-$\frac{1}{2}$. Logarithmic terms, however, do show up in higher-order corrections and, as seen in Eq. (2.21), in the local structure of the moment. Similar logarithmic dependencies are observable, e.g., in 1D spin-Peierls [FAB97] and two-leg ladder systems [NAG96, SIG96, GOG97, FUK96], where $\delta\rho(\omega) \propto 1/[|\omega| \ln^3(D/|\omega|)]$.

To summarize the results for a non-magnetic impurity, we find a bound state in the center of the pseudogap which implies a T^{-1} Curie contribution to the macroscopic susceptibility resembling a free spin-$\frac{1}{2}$. The moment is carried by Cu sites over which it is broadly distributed, its density falling off as R^{-2} with distance from the impurity. The short-ranged nature of singlet correlations implies the moment to reside predominantly on sublattice B.

2.3.2   Magnetic Impurity

We now turn to analyze an impurity with an internal $S = 1$ degree of freedom embedded in a spin-gap system as described by Hamiltonian (2.8). Spinons stemming from the initial Cu spin at site $\boldsymbol{R} = 0$ are ejected by the local

potential λ. The impurity spin, which is placed in the vacant site, is conveniently represented by two spins-$\frac{1}{2}$, i.e., $\boldsymbol{S} = \boldsymbol{S}_a + \boldsymbol{S}_b$. An infinitely strong ferromagnetic interaction $H_c = -J_c \boldsymbol{S}_a \boldsymbol{S}_b$ between these two spins is assumed. Expressing $\boldsymbol{S}_a$ and $\boldsymbol{S}_b$ in terms of new fermionic operators a_s and b_s, respectively, a mean-field decoupling of the exchange term $H_{\text{imp}} = J' \sum_{\boldsymbol{\delta}} \boldsymbol{S}_0 \boldsymbol{s}_{\boldsymbol{\delta}}$ can be performed:

$$H_{\text{imp}} = -\sum_{\boldsymbol{\delta} s} \left(\Delta'_{\boldsymbol{\delta}} \frac{a_s^\dagger + b_s^\dagger}{\sqrt{2}} f_{\boldsymbol{\delta} s} + \text{H.c.} \right) - J_c \boldsymbol{S}_a \boldsymbol{S}_b. \qquad (2.22)$$

Rather than working with the impurity operators a_s and b_s it is convenient to introduce a new set of orthogonal operators $f_{0s} = (a_s + b_s)/\sqrt{2}$ and $d_s = (a_s - b_s)/\sqrt{2}$. The impurity Hamiltonian then assumes a more intuitive form

$$H_{\text{imp}} = -\sum_{\boldsymbol{\delta} s} \left(\Delta'_{\boldsymbol{\delta}} f_{0s}^\dagger f_{\boldsymbol{\delta} s} + \text{H.c.} \right) - J_c \boldsymbol{S}_{\text{eff}} \boldsymbol{s}_0, \qquad (2.23)$$

where the impurity spins $\boldsymbol{s}_0$ and $\boldsymbol{S}_{\text{eff}}$ are expressed in terms of the operators f_{0s} and d_s, respectively. Due to the first term in Eq. (2.23), the f spinons on the impurity site hybridize with the ones on adjacent Cu sites. This process is controlled by the local mean-field parameter $\Delta'_{\boldsymbol{\delta}} = J' \sum_s \langle f_{\boldsymbol{\delta} s}^\dagger f_{0s} \rangle$ which replaces $\Delta_{\boldsymbol{\delta}}$ on bonds connecting to the impurity. A system of itinerant spinons extending over the whole lattice including the impurity site is formed. These itinerant spinons couple ferromagnetically to the localized spin $\boldsymbol{S}_{\text{eff}}$. In the limit of low energies, this coupling becomes asymptotically small. This follows from the fact that the rate at which spinons scatter on the localized spin vanishes as $\propto \omega \ln |\omega|$ in the spin-gap phase [KHA97a]. Restricting ourselves to the low-energy fixed point, itinerant spinons and localized spin $\boldsymbol{S}_{\text{eff}}$ can hence be considered as being isolated from each other. Only in the presence of a magnetic field the ferromagnetic coupling between the two systems has to be reconsidered as it leads to a polarization of spinons; this question is subject of Section 2.4.

In the remainder of the present section we analyze the properties of the spinon system, discarding for now the presence of the localized spin $\boldsymbol{S}_{\text{eff}}$. To begin with, we consider the special case of equal exchange interactions $J' = J$. With regards to the spinon sector the impurity site becomes indistinguishable from the rest of the system as $\Delta'_{\boldsymbol{\delta}} = \Delta_{\boldsymbol{\delta}}$. The spin $\boldsymbol{s}_0$ assumes the role of the original Cu spin at $\boldsymbol{R} = 0$ and a homogeneous spin liquid as described by H_{RVB} in Eq. (2.3) is formed. However, in general the two exchange integrals differ, $J' < J$, which breaks the translational invariance of the spinon system. The bond parameter then acquires an additional spatial dependence that has to be treated self-consistently. To simplify the discussion we distinguish only
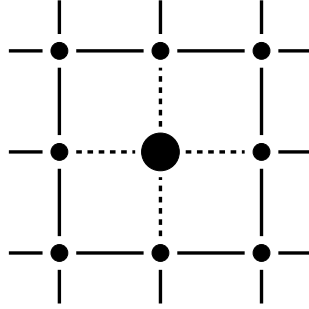
Figure 2.10: *Mean-field parameters Δ'_{δ} and Δ_{δ} are assigned to bonds that do (dashed line) or do not (solid line) connect to the impurity denoted by a large dot.*

between bonds that do or do not connect to the impurity (see Fig. 2.10),

$$\Delta_{ij} = \begin{cases} \Delta'_{\delta} & \text{for} \quad i = 0 \text{ or } j = 0, \\ \Delta_{\delta} & \text{for} \quad i, j \neq 0, \end{cases}$$

where Δ_{δ} is the mean-field parameter of the impurity-free system. The two parameters Δ'_{δ} and Δ_{δ} are assumed to exhibit the same phase relation, but in general their amplitudes differ. As a result, spinons scatter on the impurity bonds. To study this effect, we write the spinon part of Hamiltonian (2.8) as

$$H^{\text{sp}}_{\text{Ni}} = H_{\text{RVB}} + (1 - x) \sum_{\delta s} \left(\Delta_{\delta} f^{\dagger}_{0s} f_{\delta s} + \text{H.c.} \right), \tag{2.24}$$

where H_{RVB} represents the impurity-free system. The scattering amplitude $(1-x)$ with $x = |\Delta'_{\delta}/\Delta_{\delta}|$ is controlled by the ratio of J' to J. It vanishes for $J' = J$, and has to be treated self-consistently for $J' < J$. Approximately we find $x \approx J'/J$.

As in the case of a non-magnetic impurity, the spinon propagators of the pure and impurity-doped system given by Eqs. (2.9) can be related by a scattering matrix $T_{\lambda\lambda'}(i\omega)$ [see Eq. (2.10)]. It describes successive scattering of spinons on the four bonds that connect the Ni impurity site to its nearest neighbors. We obtain the following expression for the T matrix:

$$T^{\text{Ni}}_{\lambda\lambda'}(i\omega) = \frac{t_{\lambda\lambda'}(i\omega)}{i\omega G^{(0)}(i\omega) + p^2}, \tag{2.25}$$

with

$$\begin{aligned} t_{\lambda\lambda'}(i\omega) &= \frac{1-x}{1+x} G^{(0)}(i\omega)(i\omega - \xi_{\lambda})(i\omega - \xi_{\lambda'}) \\ &\quad + \frac{x}{1+x}(2i\omega - \xi_{\lambda} - \xi_{\lambda'}) - i\omega. \end{aligned}$$

The k-integrated Green's function of the pure system $G^{(0)}(i\omega)$ is defined in Eq. (2.12) and $p^2 = x^2/(1 - x^2)$. Due to the presence of the spin gap, two complex poles appear in the scattering matrix (as compared to one real pole in the case of a non-magnetic impurity). These are determined by the roots of

$$\omega G^{(0)}(i\omega \rightarrow \omega + i0^+) + p^2 = 0. \qquad (2.26)$$

One of the poles lies below the spinon chemical potential which signals the formation of a spinon bound state with finite lifetime. In analogy to the previously discussed case of a non-magnetic impurity, it describes a Cu spin left unpaired after the replacement of Cu by the impurity. The important difference is that in the case of a magnetic impurity the free Cu spins can interact with the impurity moment as is discussed in the following.

Due to the fact that J' is finite, the poles of Eq. (2.26) do not lie in the center of the pseudogap. This introduces an additional energy scale, namely the characteristic binding energy ω_K of the bound state given by the real part of the lower pole. Together with the width δ_K of the bound state, which is associated with the inverse of the life time of the bound state, we find

$$\omega_K = \frac{\pi}{4} \frac{J'}{\ln(D/J')}, \quad \delta_K = \frac{\pi}{4} \frac{\omega_K}{\ln(D/\omega_K)}, \qquad (2.27)$$

which is valid for $J' \ll J$. The two energy regions $\omega < \omega_K$ and $\omega > \omega_K$ control the physics at large and small distance from the impurity, respectively, as compared to $R_K = D/\omega_K$. These regions exhibit very different behavior: In the former case the impurity spin and the Cu moments jointly form an effective spin in what resembles an underscreened Kondo effect. At large energies this entity breaks up — impurity spin and Cu moments decouple.

First we analyze the low-energy scale $\omega < \omega_K$ that applies to low temperatures and large distances from the impurity. We calculate the impurity contribution $\delta\rho(\omega)$ to the density of states from the Green's function $\delta G(i\omega) = \sum_{\lambda\lambda'} g_\lambda^{(0)}(i\omega) T_{\lambda\lambda'}(i\omega) g_{\lambda'}^{(0)}(i\omega)$. For $\omega \ll D$ we obtain

$$\delta G_{\mathrm{Ni}}(i\omega) = \frac{\partial}{\partial i\omega} \ln[i\omega G^{(0)}(i\omega) + p^2] = \frac{2G^{(0)}(i\omega)}{i\omega G^{(0)}(i\omega) + p^2}, \qquad (2.28)$$

which yields

$$\delta\rho_{\mathrm{Ni}}(\omega) = \frac{2}{\pi}\omega_K\delta_K \frac{|\omega|}{(\omega^2 - \omega_K^2)^2 + (2\omega_K\delta_K)^2}. \qquad (2.29)$$

Figure 2.11 schematically shows the spinon density of states $\rho^{(0)}(\omega)$ and $\rho(\omega) = \rho^{(0)}(\omega) + \delta\rho(\omega)$ for the pure and impurity-doped system. The very
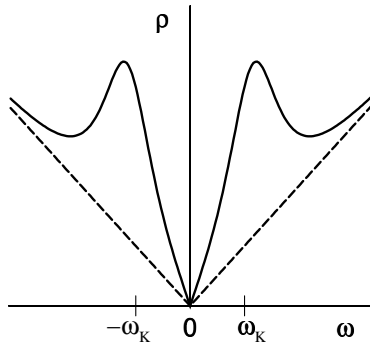
Figure 2.11: *Schematic plot of the spinon density of states for the system with a magnetic impurity (solid line) as compared to the pure system (dashed line).*

existence of a magnetic pseudogap is found to be unaffected by the presence of the impurity — $\rho^{(0)}(\omega)$ as well as $\rho(\omega)$ vanish linearly in the limit $\omega \to 0$. As a consequence, the static spin susceptibility of Eq. (2.15) vanishes as $\propto T$ at low temperatures in analogy to the impurity-free system. This indicates all spinons to participate in the formation of singlets. The spinon bound state discussed above hence partially screens the impurity spin by forming a Kondo singlet with s_0. The local spin S_{eff}, which is not part of the spinon system and therefore remains unaffected, then constitutes an effective $S = \frac{1}{2}$ impurity spin. In this underscreened Kondo problem the spinon binding energy ω_K of Eq. (2.27) plays the role of the Kondo temperature $T_K = \omega_K$. At temperatures above T_K, the impurity spin decouples from the Cu moments, while partial screening of the impurity moment occurs at temperatures below T_K. We note that the Kondo temperature exhibits an unconventional power-law dependence on the coupling parameter J' which is in contrast to the conventional exponential behavior. This peculiarity is ascribed to the fact that the impurity spin couples to bound spinons which are predominantly in localized rather than band-like states. To finish the discussion of the low-energy behavior, we point out that while the impurity does not fill the pseudogap it nevertheless renormalizes its slope. A low-energy expansion of Eq. (2.29) yields an impurity contribution to the spinon density of states that preserves the gapped structure:

$$\delta \rho_{\text{Ni}}(\omega) = \frac{1}{p^2} \rho^{(0)}(\omega),\tag{2.30}$$

which is valid for $J' \ll J$.

We now shortly turn to the energy scale $\omega > \omega_K$ which controls the behavior at large temperatures and/or small distances from the impurity site. In

(a)   (b)
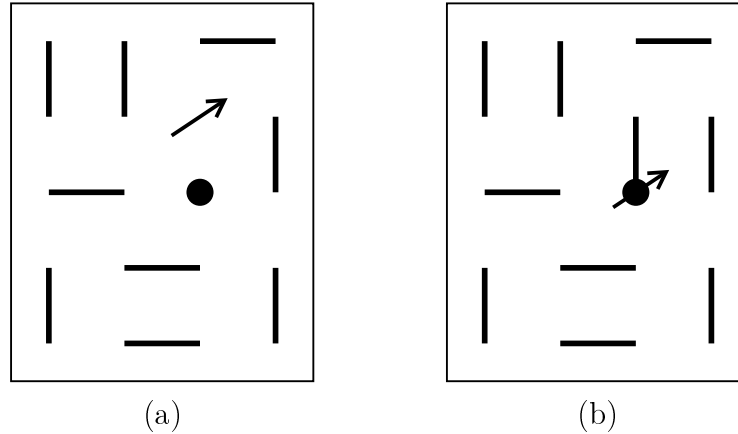
Figure 2.12: *"Snapshot" of the low-energy fixed point of a RVB liquid state with (a) a non-magnetic impurity and (b) a magnetic $S = 1$ impurity denoted by a dot. In the former case the impurity induces moments that reside on Cu sites in the proximity of the impurity. In the latter case the impurity spin is partially screened by the Cu moments. Effectively a local impurity spin-$\frac{1}{2}$ and a "healed" spin liquid results.*

this regime the impurity spin decouples from the Cu moments. The susceptibility associated with the spinon bound state is then that of a free spin-$\frac{1}{2}$, i.e., $\chi(T) = 1/(4T)$ if temperature is the leading parameter or $\chi(T) = 1/(4\omega_K)$ otherwise; simultaneously, the original $S = 1$ impurity spin is recovered. The spatial distribution of Cu moments follows the same pattern as in the case of a non-magnetic impurity.

To summarize, non-magnetic Zn and magnetic Ni impurities in a gapped spin liquid are both associated with $S = \frac{1}{2}$ magnetic moments. These are, however, of very different nature (see Fig. 2.12): In the former case the impurity induces moments that are broadly distributed over Cu sites. In the latter case the Cu moments partially screen the original $S = 1$ impurity spin in analogy to an underscreened Kondo problem. One is then left with an effective spin-$\frac{1}{2}$ located at the impurity site.

2.4 Spin Polarization

The effective impurity moments discussed in the last section can be polarized by applying an external magnetic field. In this section we analyze the incidental local response of planar Cu spins. In the case of a non-magnetic impurity, the magnetic field directly polarizes the magnetic moments induced by the impurity on the Cu sites. In the case of a magnetic impurity, the ap-

$$K_{\mathrm{Zn}}(T, \boldsymbol{R}) = \sum_{\boldsymbol{R'}} \boldsymbol{R} \qquad \boldsymbol{R'}$$

Figure 2.13: *Diagrammatic representation of the polarizability of an impurity-induced moment at site $\boldsymbol{R}$ in a uniform magnetic field.*

$$K_{\mathrm{Ni}}(T, \boldsymbol{R}) = \boldsymbol{R} \qquad \qquad 0$$

Figure 2.14: *Diagrammatic representation of the polarizability of a Cu spin at site $\boldsymbol{R}$ in a magnetic field acting on the localized moment $\boldsymbol{S}_{\mathrm{eff}}$ at site $\boldsymbol{R'} = 0$. Dashed and solid particle-hole convolution functions denote the susceptibility of the effective impurity spin and of the CuO_2 plane, respectively. The vertex function $J_c(i\omega)$ is represented by a circle.*

plied field acts on a localized impurity spin-$\frac{1}{2}$ ferromagnetically coupled to a liquid of itinerant spinons. The latter respond via a RKKY-type interaction.

We first discuss the case of a non-magnetic impurity. Here the impurity-induced moment is carried by the Cu spins which can therefore be directly polarized by the magnetic field. The static polarizability of the local moments is given by $K_{\mathrm{Zn}}(T, \boldsymbol{R}) = \sum_{\boldsymbol{R'}} [\langle T_\tau s_{\boldsymbol{R}}^z(\tau) s_{\boldsymbol{R'}}^z(0) \rangle_{\omega=0} - \langle T_\tau s_{\boldsymbol{R}}^z(\tau) s_{\boldsymbol{R'}}^z(0) \rangle_{\omega=0}^0]$. Evaluating the diagram in Fig. 2.13 we obtain

$$K_{\mathrm{Zn}}(T, \boldsymbol{R}) = \frac{1}{2\pi} \frac{\Phi(\boldsymbol{R})}{R^2} \frac{1}{T \ln(D/T)} \quad \text{for} \quad \boldsymbol{R} \in B. \qquad (2.31)$$

Equation (2.31) is valid for $\boldsymbol{R} \in B$, while contributions from sublattice A are negligibly small for reasons discussed in Section 2.3. The polarizability is found to decay slowly as R^{-2} with distance from the impurity. This behavior is reminiscent of the competition between spinon localization and spin-singlet fluctuations — a bound state forms, but it is broadly distributed. This marginal character of the Zn moment is further reflected in a logarithmic suppression of the T^{-1} Curie-like behavior of Eq. (2.31). This effect can actually be observed experimentally as is shown in Section 2.6.

Next we turn to the slightly more involved case of a magnetic impurity. Here the magnetic field acts only on the effective impurity moment $\boldsymbol{S}_{\mathrm{eff}}$ as all other spins are in a singlet configuration. The Cu spins then get polarized indirectly via the ferromagnetic coupling between spinons and effective impurity spin. The static polarization to be calculated is $K_{\mathrm{Ni}}(T, \boldsymbol{R}) = \langle T_\tau s_{\boldsymbol{R}}^z(\tau) S_{\mathrm{eff}}^z(0) \rangle_{\omega=0}$. Expressed in terms of Green's functions (see Fig. 2.14) it becomes

$$K_{\mathrm{Ni}}(T, \boldsymbol{R}) = -T^2 \sum_{\varepsilon, \varepsilon'} \Pi_d(i\varepsilon') J_c(i\varepsilon - i\varepsilon') \Pi_f(i\varepsilon, \boldsymbol{R}), \qquad (2.32)$$

with particle-hole convolution functions

$$
\begin{aligned}
\Pi_d(i\varepsilon) &= D^2(i\varepsilon), \\
\Pi_f(i\varepsilon, \boldsymbol{R}) &= G(i\varepsilon, -\boldsymbol{R}) G(i\varepsilon, \boldsymbol{R}).
\end{aligned}
$$

Here the impurity Green's function is $D(i\omega) = -\langle T_\tau d_s(\tau) d_s^\dagger(0) \rangle_{i\omega} = 1/(i\omega)$ and the inter-site spinon Green's function $G(i\omega, \boldsymbol{R}) = -\langle T_\tau f_{0s}(\tau) f_{\boldsymbol{R}s}^\dagger(0) \rangle_{i\omega}$. Operators d and f act on separated sectors of the Hilbert space. At site $\boldsymbol{R} = 0$, f spinons are polarized by the local spin $\boldsymbol{S}_{\mathrm{eff}}$ due to the ferromagnetic interaction of bare strength $J_c \to \infty$. This coupling is accounted for by the vertex function $J_c(i\omega)$. Employing a ladder approximation yields

$$J_c(i\omega) = \frac{J_c}{1 + J_c \Pi_c^{i\omega}} = \frac{1}{\Pi_c^{i\omega}}, \qquad (2.33)$$

with

$$\Pi_c^{i\omega} = -T \sum_\varepsilon D(i\varepsilon + i\omega) G(i\varepsilon, \boldsymbol{R} = 0).$$

Replacing the vertex function by its zero-frequency limit $J(i\omega) \to J(0)$, the polarizability of Eq. (2.32) can be factorized. Within this approximation, which is valid at low temperatures, one obtains

$$K_{\mathrm{Ni}}(T, \boldsymbol{R}) = \chi_{\mathrm{eff}}(T) J_c(0) \chi_{\mathrm{pl}}(T, \boldsymbol{R}). \qquad (2.34)$$

The polarizability has thus been decomposed into the magnetic suscepti-bility of the effectively free $S = \frac{1}{2}$ impurity spin $\chi_{\mathrm{eff}}(T) = 1/(4T)$, the non-local magnetic susceptibility of CuO_2 planes $\chi_{\mathrm{pl}}(T, \boldsymbol{R})$, and an effec-tive coupling parameter $J_c(0)$. The susceptibilities are defined as $\chi_{\mathrm{eff}}(T) = \langle T_\tau S_{\mathrm{eff}}^z(\tau) S_{\mathrm{eff}}^z(0) \rangle_{\omega=0} = -T \sum_\varepsilon \Pi_d(i\varepsilon)$ and $\chi_{\mathrm{pl}}(T, \boldsymbol{R}) = \langle T_\tau s_0^z(\tau) s_{\boldsymbol{R}}^z(0) \rangle_{\omega=0} = -T \sum_\varepsilon \Pi_f(i\varepsilon, \boldsymbol{R})$.

To further analyze the polarizability in Eq. (2.34), the expressions for $J_c(0)$ and $\chi_{\mathrm{pl}}(\boldsymbol{R})$ have to be evaluated. This requires the on-site and inter-site spinon Green's functions

$$G_{\mathrm{Ni}}(i\omega, \boldsymbol{R}) = \begin{cases} \left(\dfrac{p}{x}\right)^2 \dfrac{G^{(0)}(i\omega)}{i\omega G^{(0)}(i\omega) + p^2} & \text{for} \quad R = 0, \\[4mm] \dfrac{1}{x} \, G^{(0)}(i\omega, \boldsymbol{R}) & \text{for} \quad R > R_K, \end{cases} \qquad (2.35)$$

where $G^{(0)}(i\omega, \boldsymbol{R})$ is defined for the impurity-free system and is given by Eqs. (2.18) — the factor $1/x$ accounts for the renormalization of the pseudogap

in the presence of the impurity. We are now in the position to calculate the effective coupling parameter from the zero-frequency limit of Eq. (2.33) for which we obtain

$$J_c(0) = \begin{cases} D & \text{for} \quad J' = J, \\ 2\omega_K & \text{for} \quad J' \ll J. \end{cases} \qquad (2.36)$$

Furthermore, the non-local spin susceptibility of CuO_2 planes in the presence of the impurity is

$$\chi_{\text{pl}}(\boldsymbol{R}) = -\frac{3}{4\pi} \frac{1}{Jx^2} \frac{\Phi(\boldsymbol{R})}{R^3} \quad \text{for} \quad \boldsymbol{R} \in B, \qquad (2.37)$$

the latter being valid for $\boldsymbol{R} \in B$ with $R > R_K$. Finally, combining these results we obtain

$$K_{\text{Ni}}(T, \boldsymbol{R}) = -\frac{3}{16\pi} \frac{J_c(0)}{Jx^2} \frac{\Phi(\boldsymbol{R})}{R^3} \frac{1}{T} \quad \text{for} \quad \boldsymbol{R} \in B. \qquad (2.38)$$

Equation (2.38) describes the polarizability of a Cu spin at site $\boldsymbol{R}$ responding to a magnetic field that acts on the effective impurity spin $\boldsymbol{S}_{\text{eff}}$; contributions from sublattice A are again negligibly small. The polarizability is found to fall off as R^{-3} with distance from the impurity which compares to a R^{-2} behavior in the case of Zn, reflecting the delocalized nature of the Zn moment. We note that the T^{-1} Curie behavior displayed by Eq. (2.38) stems solely from the susceptibility $\chi_{\text{eff}}(T)$ of the effective impurity spin. Within the present mean-field treatment, the planar susceptibility is independent of temperature, i.e., $\chi_{\text{pl}}(T, \boldsymbol{R}) = \chi_{\text{pl}}(\boldsymbol{R})$.

In deriving Eqs. (2.31) and (2.38) for the polarizability of Cu spins we have, up to this point, built upon RVB mean-field theory. This picture accounts well for the spin-liquid features of underdoped cuprates which includes the presence of a magnetic pseudogap. Its strength lies on the description of long-range properties controlled by low-energy excitations. The mean-field treatment does, however, severely underestimate local AF correlations which reflect the proximity of a critical instability towards AF spin ordering. As a consequence, the above expressions contain no reference to the AF correlation length which was suggested to introduce a temperature dependence beyond the Curie behavior of free moments [MRR98]. Furthermore, mean-field theory yields a polarizability of Cu spins on one sublattice only, underestimating the staggered magnetization of spins on the opposite sublattice. This is in disaccord with NMR measurements [BOB97b] that yield no overall shift of the ^{17}O line as would be expected from the polarization of only one sublattice as well as with numerical studies [MAR97, LAU98].

To compensate for these deficiencies of the mean-field treatment, we simulate the closeness of the spin system towards an antiferromagnetically ordered
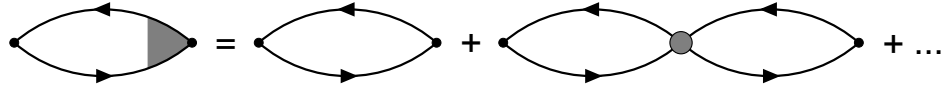
Figure 2.15: *Diagrammatic representation of the RPA approximation for the susceptibility of Cu spins. The vertex function $J_{\boldsymbol{q}}$ is denoted by a shaded dot.*

state by performing a random phase approximation (RPA) in the magnetic susceptibility. The approach is the same for magnetic and non-magnetic impurities. Here we illustrate the important points, using the case of a magnetic impurity as an example. Performing a summation of RPA diagrams in momentum space (see Fig. 2.15), the susceptibility of planar Cu spins becomes

$$\chi_{\text{pl}}^{\text{RPA}}(T, \boldsymbol{q}) = \chi_{\text{pl}}(\boldsymbol{q})S(T, \boldsymbol{q}), \tag{2.39}$$

with the Stoner enhancement factor

$$S(T, \boldsymbol{q}) = \frac{1}{1 + J_{\boldsymbol{q}}\chi_{\text{pl}}(T, \boldsymbol{q})}, \tag{2.40}$$

where $J_{\boldsymbol{q}} = 2J(\cos q_x + \cos q_y)$. We closely follow the theory of a nearly AF Fermi liquid [MON94, PIN97] which maps Eq. (2.39) onto a phenomenological expression involving the AF correlation length $\xi(T)$. Within this picture $\chi_{\text{pl}}^{\text{RPA}}(T, \boldsymbol{q})$ is assumed to be controlled solely by the momentum region close to the AF wave vector $\boldsymbol{Q} = (\pi, \pi)$. We do take a slightly different point of view in this respect: The momentum dependence of the bare susceptibility $\chi_{\text{pl}}(\boldsymbol{q})$ in Eq. (2.39), which describes the long-range characteristics of spin correlations in the presence of a magnetic pseudogap, is explicitly kept. Only the scaling function $S(T, \boldsymbol{q})$ which controls short-range AF correlations is expanded around $\boldsymbol{Q} = (\pi, \pi)$. Identifying $J\chi_{\text{pl}}(T, \boldsymbol{Q})/[1 - 4J\chi_{\text{pl}}(T, \boldsymbol{Q})] = \xi^2(T)$ and $1/[J\chi_{\text{pl}}(T, \boldsymbol{Q})] = \alpha$, Eq. (2.40) can be written in the phenomenological form

$$S(T, \boldsymbol{q}) = \frac{\alpha \xi^2(T)}{1 + (\boldsymbol{q} - \boldsymbol{Q})^2 \xi^2(T)}, \tag{2.41}$$

where $\alpha \approx 1$ on a mean-field level. We note that the explicit form of $\xi(T)$ lies beyond the accessibility of a mean-field treatment and has to be chosen according to general physical considerations.

We shortly recapitulate the essence of this new approach up to this point: We factorize the "full" susceptibility $\chi_{\text{pl}}^{\text{RPA}}(T, \boldsymbol{q})$ into two terms, the "bare" susceptibility $\chi_{\text{pl}}(T, \boldsymbol{q})$ and the scaling function $S(T, \boldsymbol{q})$. Rather than mapping the "full" susceptibility onto a phenomenological form involving the AF correlation length, we explicitly keep $\chi_{\text{pl}}(T, \boldsymbol{q})$ and only replace the scaling function $S(T, \boldsymbol{q})$. In this way we are able to preserve the spin-gap physics

contained in $\chi_{\mathrm{pl}}(T, \boldsymbol{q})$, while extending our theory to further account for the presence of AF correlations.

To finish the discussion of AF correlations, we turn back to real space. Here the non-local susceptibility is now

$$\chi_{\mathrm{pl}}^{\mathrm{RPA}}(T, \boldsymbol{R}) = \sum_{\boldsymbol{R}' \in B} \chi_{\mathrm{pl}}(\boldsymbol{R}') S(T, \boldsymbol{R} - \boldsymbol{R}'). \tag{2.42}$$

For distances $R \gg \xi(T)$ this expression can be approximated by

$$\chi_{\mathrm{pl}}^{\mathrm{RPA}}(T, \boldsymbol{R}) = \frac{1}{2} \chi_{\mathrm{pl}}(\boldsymbol{R}) \xi^2(T), \tag{2.43}$$

where an interpolation formula for the A sublattice is used: $\chi_{\mathrm{pl}}(\boldsymbol{R} \in A) = -(1/z) \sum_{\boldsymbol{\delta}} \chi_{\mathrm{pl}}(\boldsymbol{R} + \boldsymbol{\delta})$. Analogous expressions are obtained for the polarizability of moments induced by a non-magnetic impurity. Combining these results with Eqs. (2.31) and (2.38) and performing an angular average over phase factors $\Phi(\boldsymbol{R})$ which yields a factor of $\frac{1}{2}$, one finally arrives at the following expressions for the polarizability of Cu spins in the impurity-doped system:

$$K_{\mathrm{Zn}}(T, \boldsymbol{R}) = -\cos(\boldsymbol{Q}\boldsymbol{R}) \frac{1}{8\pi} \frac{1}{R^2} \frac{\xi^2(T)}{T \ln(D/T)}, \tag{2.44}$$

$$K_{\mathrm{Ni}}(T, \boldsymbol{R}) = \cos(\boldsymbol{Q}\boldsymbol{R}) \frac{3}{64\pi} \frac{J_c(0)}{J x^2} \frac{1}{R^3} \frac{\xi^2(T)}{T}. \tag{2.45}$$

These equations now hold for both sublattices $\boldsymbol{R} \in \{A, B\}$, the staggered nature of spin correlations being manifested in the alternating sign implied by $\cos(\boldsymbol{Q}\boldsymbol{R})$. Furthermore, the dependence upon the AF correlation length $\xi(T)$ is now explicitly accounted for.

2.5 Implications for NMR

The impurity-induced polarization of Cu spins in a magnetic field affects the energy levels of nuclear spins via (supertransferred) hyperfine interaction. The coupling of a given nuclear spin $\boldsymbol{I}$ to electron spins $\boldsymbol{s}_i$ on close-by Cu sites is described by

$$H_{\mathrm{hf}} = \gamma_n \gamma_e C_{\mathrm{hf}} \sum_i \boldsymbol{s}_i \boldsymbol{I}, \tag{2.46}$$

where γ_n and γ_e denote the nuclear and electron gyromagnetic ratios, respectively, and C_{hf} is the (supertransferred) hyperfine coupling constant. On a

mean-field level, $\boldsymbol{s}_i$ can be replaced by its average value $\langle \boldsymbol{s}_i \rangle = K(T, \boldsymbol{R}_i) \boldsymbol{H}_0$ with external magnetic field $\boldsymbol{H}_0$ and polarizability $K(T, \boldsymbol{R}_i)$. The coupling Hamiltonian hence becomes

$$H_{\mathrm{hf}} = \gamma_n \gamma_e C_{\mathrm{hf}} \boldsymbol{H}_0 \boldsymbol{I} \sum_i K(T, \boldsymbol{R}_i). \qquad (2.47)$$

In the following we derive expressions for the NMR Knight shift induced by a non-magnetic impurity and for the NMR line broadening induced by both magnetic and non-magnetic impurities. These expressions are compared to experimental data in Section 2.6.

2.5.1   Knight Shift

In the presence of local magnetic moments the NMR resonance frequency is

$$\Delta = \gamma_n H_0 \left[1 + \delta K(T) \right], \qquad (2.48)$$

where the dimensionless function $\delta K(T)$ defines the Knight shift — it comprises the effect of the magnetically active environment. We restrict ourselves to the Knight shift measured on the nucleus of a non-magnetic impurity (i.e., Zn or Al). The effect of AF correlations can be neglected here since the Knight shift depends predominantly on the local susceptibility of Cu moments — this quantity remains unaffected by the presence of AF correlations.

To first order the impurity nucleus is subject only to the local moments on nearest neighbor Cu sites. From Eq. (2.47) and using expression (2.31) for the local polarizability of Cu moments, one obtains in a straightforward manner the following expression for the Knight shift:

$$\delta K(T) = \frac{2}{\pi} \gamma_e C_{\mathrm{hf}} \frac{1}{T \ln(D/T)}, \qquad (2.49)$$

which applies to the NMR signal of a non-magnetic impurity nucleus.

2.5.2   Line Broadening

In a system with randomly distributed impurities the superposition of local fields induced by the multitude of impurities leads to a broadening of the NMR line. We first calculate the lineshape for a system with finite concentration of Zn or Ni impurities, employing the formalism of Ref. [WAL74]. From this we then deduce the linewidth of the NMR signal. Specifically we are interested in the signal obtained from ^{17}O nuclei. The presence of AF correlations is explicitly taken into account here.
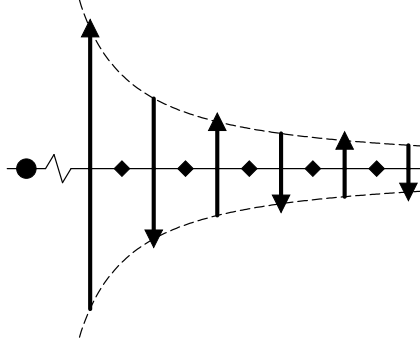
Figure 2.16: *Schematic cut through a CuO_2 plane, showing the position of O ions (diamonds) placed between two Cu sites with staggered spin polarization (arrows). The magnitude of the polarization falls off with distance from the impurity (circle) as R^{-2} in the case of Zn and as R^{-3} in the case of Ni.*

The lineshape function $g(\nu)$ is defined in Ref. [WAL74] as the Fourier transform of the characteristic or free-induction function

$$f(t) = \exp\Big[-c\sum_{\boldsymbol{R}} \Big(1 - e^{i\omega(\boldsymbol{R})t}\Big)\Big], \tag{2.50}$$

where c is the concentration of impurities and $\omega(\boldsymbol{R})$ denotes the frequency shift induced by an impurity at site $\boldsymbol{R}$. Since each ^{17}O nucleus lies symmetrically between two Cu sites that belong to different sublattices with spins polarized in opposite directions, the impurity-induced energy shift partially cancels (see Fig. 2.16). At large enough distance from the impurity, the shift is effectively determined by the spatial derivative of the polarizability:

$$\omega(\boldsymbol{R}) = \kappa \frac{\partial|K(T,\boldsymbol{R})|}{\partial R} \cos\phi, \tag{2.51}$$

where ϕ denotes the angle enclosed by $\boldsymbol{R}$ and the x or y axis and $\kappa = \gamma_n\gamma_e C_{\mathrm{hf}}^{\mathrm{O\text{-}Cu}} H_0$. The polarizability $K(T,\boldsymbol{R})$ is given by Eqs. (2.44) and (2.45) for Zn and Ni, respectively. Inserting Eq. (2.51) into (2.50) and integrating over lattice sites, one obtains

$$\ln f(t) = \begin{cases} -\Lambda_{\mathrm{Zn}}|t|^{2/3}, \\ -\Lambda_{\mathrm{Ni}}|t|^{1/2}, \end{cases} \tag{2.52}$$

with

$$\Lambda_{\mathrm{Zn}} = c\frac{2\sqrt{3}\pi^2}{\Gamma^2(1/3)}\Big[\kappa\frac{1}{8\pi}\frac{\xi^2(T)}{T\ln(D/T)}\Big]^{2/3},$$

$$\Lambda_{\mathrm{Ni}} = c\frac{2\sqrt{6}\pi\Gamma(3/4)}{\Gamma(1/4)}\Big[\kappa\frac{3}{64\pi}\frac{J_c(0)}{Jx^2}\frac{\xi^2(T)}{T}\Big]^{1/2}.$$
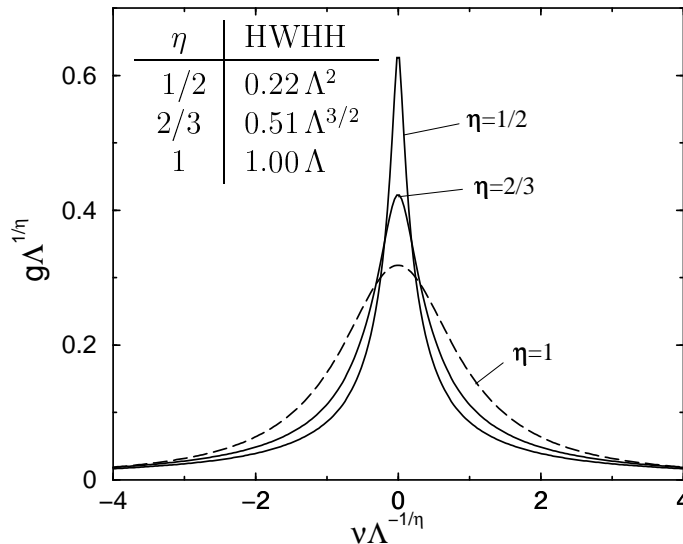
Figure 2.17: *Lineshape function $g(\nu)$ obtained by performing a Fourier transformation of the characteristic function $f(t) = \exp[-\Lambda|t|^{\eta}]$ with $\eta = \frac{1}{2}$ for Ni and $\eta = \frac{2}{3}$ for Zn. For comparison the Lorentzian lineshape of conventional RKKY theory with $\eta = 1$ is indicated by a dashed line. Numerical values for the half width at half height (HWHH) are given in the inset.*

Figure 2.17 shows the different lineshapes induced by Zn and Ni impurities as obtained by performing a Fourier transformation on $f(t)$. Comparing to the Lorentzian shape that results from $\ln f(t) \propto -|t|$ in conventional RKKY theory, one finds a marked difference in both shape and width. Using the numerical values shown in the inset of Fig. 2.17, we finally arrive at the following expressions for the full linewidth induced by non-magnetic and magnetic impurities, respectively:

$$\Delta\nu_{\mathrm{Zn}} = 2 \times 0.51 \left(\Lambda_{\mathrm{Zn}}\right)^{3/2}, \tag{2.53}$$

$$\Delta\nu_{\mathrm{Ni}} = 2 \times 0.22 \left(\Lambda_{\mathrm{Ni}}\right)^{2}. \tag{2.54}$$

2.6   Comparison with Experiment

In this section we compare expression (2.49) for the Knight shift and expressions (2.53) and (2.54) for the line broadening with experimental data. First we analyze ^{27}Al Knight-shift data by Ishida, Kitaoka, Yamazoe, *et al.* [ISD96] obtained for $\mathrm{La}_{1.85}\mathrm{Sr}_{0.15}\mathrm{CuO}_4$ at an impurity concentration of 3%. We employ Eq. (2.49) with the following parameters: The superexchange parameter is set to $J = 0.13$ eV. The supertransferred coupling constant
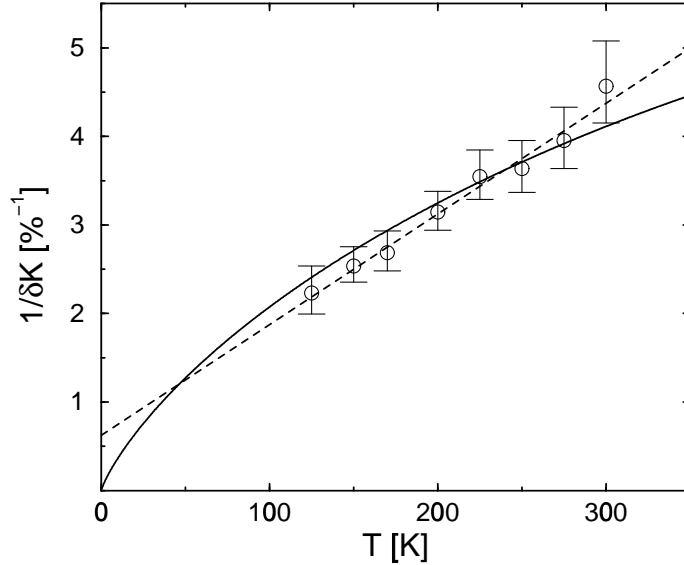
Figure 2.18: *Inverse of the impurity-induced Knight shift for ^{27}Al. The solid line is a fit of Eq. (2.49) to experimental data on $La_{1.85}Sr_{0.15}CuO_4$ [ISD96] indicated by circles. The zero-temperature offset of a linear fit (dashed line) indicates a deviation from a pure T^{-1} Curie behavior at low temperatures.*

between the ^{27}Al nuclear spin and surrounding Cu electron spins is used as a fitting parameter for which we obtain $C_{hf}^{Al\text{-}Cu} = 1.8 \text{ T}/\mu_B$. This compares well to $C_{hf}^{Al\text{-}Cu} = 1.6 \text{ T}/\mu_B$ found by Ishida *et al.* [ISD96]. Figure 2.18 shows the inverse of the impurity-induced Knight shift as a function of temperature.[2] The marginal character of the bound state leading to a logarithmic deviation from a T^{-1} Curie law becomes important at low temperatures. Due to the onset of superconductivity, this region is not directly accessible by experiment. However, the zero-temperature offset that would follow from a linear fit of the experimental data (dashed line) suggests a pronounced deviation from a T^{-1} behavior which is correctly accounted for by our theory.

Next we compare the impurity-induced ^{17}O NMR line broadening as described by Eqs. (2.53) and (2.54) to experimental data of Bobroff, Alloul, Yoshinari, *et al.* [BOB97b] obtained on $YBa_2Cu_3O_{6.6}$ doped with Zn/Ni at a concentration of 1%. The following constants are chosen: The superexchange parameters are specified by $J = 0.13$ eV for Cu-Cu interaction and $J' = J/2$ for Cu-Ni.[3] A self-consistent treatment yields a scattering ampli-

---

[2]The theoretical curve in Fig. 2.18 is obtained from Eq. (2.49) with an additional factor $f(T) = [(D/T)K_1(T/D)]^2 \approx 1$ that accounts for higher-order corrections discussed in Ref. [KHA97b].

[3]The Ni^{2+} ion with spin 1 has two holes on the 3D shell in $d_{x^2-y^2}$ and $d_{3z^2-r^2}$ orbitals.

tude $(1 - x) = 0.5$, where $\Delta = \frac{1}{4}$ has been used. The Kondo temperature is obtained by numerically solving Eq. (2.26) which gives $T_K = 560$ K. Below this temperature the Ni spin is partially screened and behaves as a spin-$\frac{1}{2}$ ferromagnetically coupled to the CuO$_2$ plane. The effective coupling constant of this interaction is $J_c(0) = 0.1$ eV as follows from Eq. (2.36). The hyperfine coupling constant between ^{17}O nuclear and Cu electron spins is specified in Ref. [MRR98] as $C_{\mathrm{hf}}^{\mathrm{O\text{-}Cu}} = 3.3$ T$/\mu_B$. The magnetic field strength used in the experiment is $H_0 = 7.5$ T, the concentration of Ni and Zn impurities is 1%. The effective impurity concentration within the CuO$_2$ planes is larger by a factor of $\frac{3}{2}$ which is due to the fact that the impurity ions predominantly enter the CuO$_2$ planes but not the one-dimensional CuO chains present in YBa$_2$Cu$_3$O$_{6.6}$; hence $c = 1.5\%$ follows. Finally, an expression for the AF correlation length $\xi(T)$ has to be specified. It is argued in Ref. [STO97] that below a critical temperature T_{cr} determined by $\xi(T_{\mathrm{cr}}) \approx 2$, the correlation length assumes the form

$$\xi(T) = \frac{1}{a + bT}, \tag{2.55}$$

where a and b are fitting constants of the theory. Saturation of $\xi(T)$ at low temperatures is neglected here.

Figure 2.19 shows the impurity-induced line broadening $\Delta\nu_{\mathrm{imp}}$ scaled with temperature. The curves are fitted to the experimental data by setting $a = 0.07$ and $b = 0.0007$ which corresponds to an AF correlation length of $\xi = 4.8$ in units of lattice spacings at $T = 200$ K. This compares well to $\xi = 5.9$ obtained in Ref. [BAR95]. No further fitting parameters are needed.

The theory correctly accounts for the peculiar experimental observation of Zn having a more pronounced effect on the NMR signal than Ni — this seems to be in contradiction to SQUID measurements on the macroscopic susceptibility [MEN94]. We are able to ascribe this behavior to the different spatial dependence of the polarizability: $K(T, \boldsymbol{R})$ decays as R^{-3} in the case of Ni, but only as R^{-2} in the case of Zn. Averaging over all impurity site this leads to an enhanced line broadening effect of Zn (see Fig. 2.17). Our theory further correctly describes the anomalous non-Curie temperature dependence exhibited by the NMR linewidth — this seems to be in disaccord with an almost perfect T^{-1} behavior exhibited by the macroscopic susceptibility [MEN94]. One can resolve this contradiction by assuming a temperature dependence of the AF correlation length $\xi(T)$ which enters the polarizability of Cu spins. Good agreement with experiment is obtained by employing $\xi(T)$ of the form given in Eq. (2.55).

Since superexchange is mainly contributed to by the $d_{x^2-y^2}$ orbital, one obtains $J'/J = 1/2$.
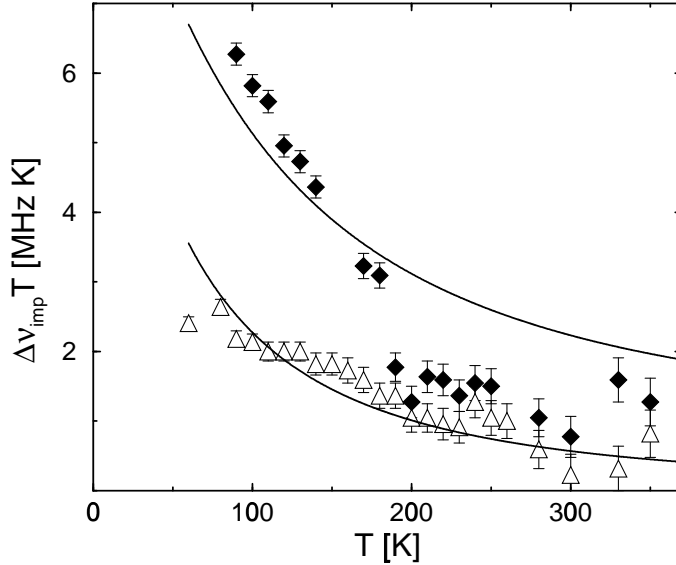
Figure 2.19: *Impurity-induced NMR line broadening $\Delta\nu_{imp}$ multiplied by temperature. The theoretical result is indicated by solid lines fitted to experimental ^{17}O data for 1% Ni-doped (triangles) and 1% Zn-doped (diamonds) $YBa_2Cu_3O_{6.6}$ [BOB97b].*

2.7 Conclusion

In summary, we have studied the local moments induced in underdoped cuprates by substituting Cu with non-magnetic ($S = 0$) Zn or magnetic ($S = 1$) Ni impurities. In the presence of a spin gap, both types of impurities are associated with $S = \frac{1}{2}$ magnetic moments in the CuO_2 planes. These are, however, of very different nature. Zn as well as Ni disturb the spin liquid formed by planar Cu spins, resulting in magnetic moments residing on Cu sites in the proximity of the impurity. In the case of Zn the moments are broadly distributed over Cu sites — macroscopically they resemble a free spin-$\frac{1}{2}$. In the case of Ni the Cu moments partially shield the internal impurity spin below a critical temperature T_K in what resembles an underscreened Kondo model; an effective impurity spin-$\frac{1}{2}$ results. Since predominantly localized rather than band-like states are involved in the screening of the impurity spin, the Kondo temperature exhibits an unconventional power-law dependence on the coupling constant. We have further investigated the RKKY-type response of Cu spins in a magnetic field. The spin polarization is found to decay as R^{-3} with distance from a Ni impurity, but only as R^{-2} in the case of Zn. This different behavior reflects the delocalized character of Zn moments and explains why Zn has a stronger impact on the NMR linewidth

than Ni. The broad distribution of the Zn moment is a manifestation of the marginal character of the bound state which also leads to a logarithmic deviation from a T^{-1} behavior in the Knight shift. This agrees with experimental data. Further, we can successfully describe the non-Curie behavior of the impurity effect on the NMR linewidth by accounting for the presence of temperature-dependent AF correlations. In general it can be concluded that the anomalous impurity properties of underdoped cuprates are a clear manifestation of the peculiar mixture of spin-singlet and antiferromagnetic correlations present in these compounds.

Chapter 3

Anomalous Optical Spectra of Ferromagnetic Manganites

3.1 Introduction

A nearly universal feature of perovskite manganites is the existence of a ferromagnetic metallic phase (see Fig. 3.1). The interplay between metallic charge motion and ferromagnetism exhibited by the system was already under investigation in the 1950's: The double-exchange mechanism discussed in Chap. 1 was identified as the link between the magnetic and the charge sector [ZEN51, AND55, DEG60]. The theory is based on the observation of a strong Hund's coupling acting between Mn $3d$ electrons which are in a $(t_{2g})^3(e_g)^1$ configuration — the transfer amplitude of itinerant e_g electrons can be maximized by ferromagnetically aligning the $S^c = \frac{3}{2}$ core spins formed out of localized t_{2g} electrons. By now it has become widely recognized that the physics of manganites is by far too rich to be explained in terms of double exchange alone. Various efforts to improve on the theory have been undertaken. Here an "inside-out" approach is followed: We believe the metallic phase to be the pivot of the phase diagram of manganites; a deeper understanding of its peculiar properties is therefore of central interest for extending the double-exchange mechanism beyond its original scope. We present here a theory of the metallic state of manganites that comprises orbital degeneracy, on-site interactions, and lattice effects. Good agreement with the anomalous optical spectra observed experimentally validates our approach.

Hund's rule coupling between itinerant e_g electrons and local t_{2g} spins is typically larger than the one-electron bandwidth in manganites. For $La_{1-x}Sr_xMnO_3$, e.g., these numbers roughly compare as 2.5 eV to 1.5 eV, respectively [HWA96]. The e_g-electron band therefore splits up into two well
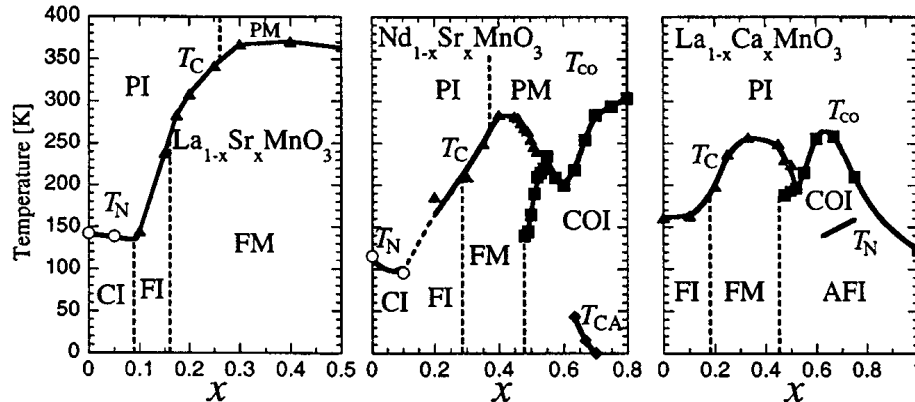
Figure 3.1: *A ferromagnetic metallic phase (FM) is observable in a variety of perovskite manganites. The other phases are denoted by: canted insulator (CI), ferromagnetic insulator (FI), charge-ordered insulator (COI), antiferromagnetic insulator (AFI), paramagnetic insulator (PI), and paramagnetic metal (PM). From [IMA98].*

separated bands (see Fig. 3.2). Transitions between the two bands dominate the optical spectrum in the paramagnetic phase at $T > T_C$ where they show up in the high-energy region (1 - 3 eV). In the ferromagnetic phase at $T < T_C$ the two bands become spin polarized. Optical inter-band transitions are then no longer allowed, leading to a collapse of spectral weight onto the low-energy region (0 - 1 eV). It is important to note that at $T \ll T_C$ the ferromagnetic moment is fully saturated and the suppression of inter-band transitions is complete. Surprisingly the e_g electrons nevertheless do not behave as a conventional spin-polarized metal: Rather than accumulating into a zero-frequency Drude peak, the spectral weight of manganites robustly extends up to ≈ 1 eV even as zero temperature is approached. This effect is remarkable not only for its energy scale that rules out a pure phononic origin but also for the magnitude of incoherent spectral weight: At low temperatures, the Drude weight accounts for only 20% of the total spectral weight, while the remaining 80% are contained in the incoherent part of the spectrum.

The orbital degeneracy of e_g electrons was proposed by several authors [SHI97, ISH97a] as one of the origins of the incoherency observed in the optical spectrum. Experimental studies in fact show collective as well as local lattice distortions to be absent in metallic manganites, suggesting orbital fluctuations be strong [BIL96, BOO98, LAN98]. Based upon this observation, Shiba, Shiina, and Takahashi [SHI97] ascribe the excitations leading to the incoherent structure of the optical conductivity to transitions between
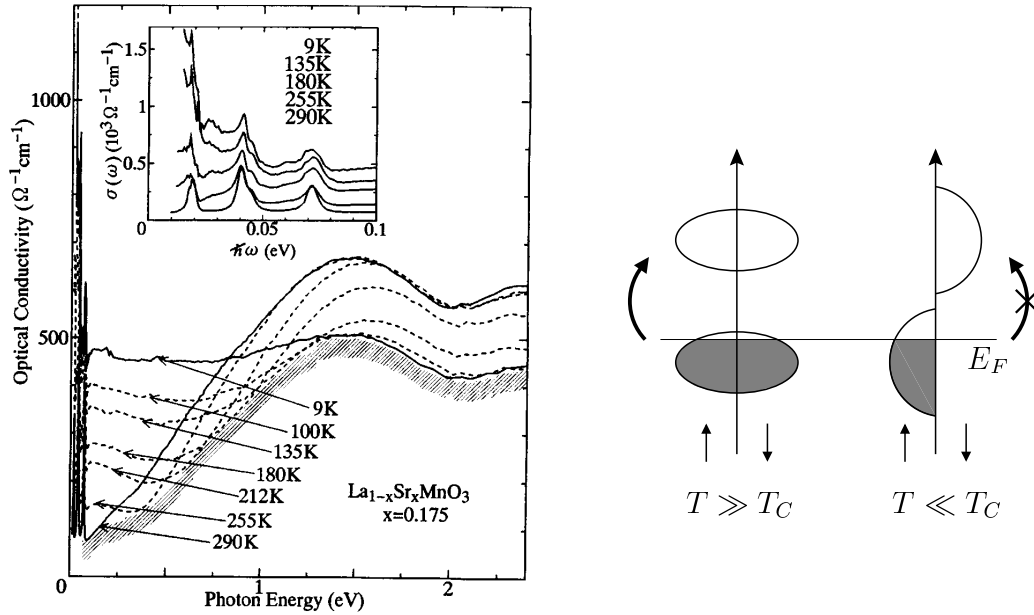
Figure 3.2: *Optical conductivity spectrum of $La_{0.825}Sr_{.175}MnO_3$ with $T_C = 238$ K: Transitions between exchange-split bands constitute the high-energy part of the spectrum at $T > T_C$. Below T_C the bands are fully spin polarized which forbids optical inter-band transitions; the spectral weight then shifts to low energies. See also Fig. 1.21. From [OKI95] (left).*

two orbital bands within spin-polarized e_g bands. While their model indicates the role of orbital degeneracy, it neglects the on-site repulsion between e_g electrons. We believe this approximation to be not well justified for the following reasons: (1) On-site interactions are strong as can be inferred from the presence of a pronounced Hund's coupling; and (2) due to the orbital degeneracy, Pauli's exclusion principle is ineffective in preventing double occupancies despite the fact that spins are aligned ferromagnetically. Hence, electrons are expected to scatter strongly on each other. A more elaborate treatment of both orbital degeneracy and on-site interactions was performed by Ishihara, Yamanaka, and Nagaosa [ISH97a, NAG98]. Led by the experimental observation of only a small discontinuity at the Fermi level in photoemission spectra [CHA93, SAI95, SAR96], the authors suggested that a conventional electronic description of metallic manganites would be insufficient. Rather, in analogy to the spin-charge separation in metallic cuprates, orbital and charge degrees of freedom should be treated on separate footings. This leads to the notion of an orbital liquid discussed in Chap. 1.

In this chapter we present the first microscopic theory of the optical con-

ductivity of manganites which combines strong correlations and orbital degeneracy. Based upon an orbital-liquid scheme, the transport properties are shown to be highly incoherent even in the ferromagnetic metallic phase. Strong scattering of charge carriers on dynamical orbital fluctuations is identified as the origin of the incoherency. This mechanism gives rise to a broad optical absorption spectrum extending up to the bare bandwidth accompanied by a pronounced suppression of the Drude weight. The theory is further extended to account for phononic degrees of freedom which are shown to play an important role in metallic manganites. Finally we argue that there is no discrepancy between the small values of specific heat found experimentally [OKI95, OKI97, WOO97, OKU98] and the strong-correlation picture employed here.

3.2 Orbital-Liquid State

The starting point for our study of the metallic state of manganites is the t-J model of an orbitally degenerate system subject to Hund's coupling — the model was introduced in Chap. 1 [see Eq. (1.13)]. Assuming complete ferromagnetic saturation and treating spins on a classical level, $\boldsymbol{S}_i\boldsymbol{S}_j$ can be replaced by the expectation value $\langle \boldsymbol{S}_i\boldsymbol{S}_j \rangle = S^2$; spin indices may then be dropped. We note that the classical treatment of spins is justified from the fact that local $S = 2$ spins are large. Hence, we obtain a simplified t-J model that depends only on orbital but not on spin quantum numbers:

$$H_{tJ} = -\sum_{\langle ij\rangle_\gamma}\sum_{\alpha\beta}\left(t_\gamma^{\alpha\beta}\hat{c}_{i\alpha}^\dagger\hat{c}_{j\beta} + \text{H.c.}\right) + J\sum_{\langle ij\rangle_\gamma}\left(\tau_i^\gamma\tau_j^\gamma - \frac{n_in_j}{4}\right). \qquad (3.1)$$

Here $\langle ij\rangle_\gamma$ denotes nearest-neighbor bonds in spatial direction $\gamma \in \{x, y, z\}$ and the indices α, β act within the orbital subspace with pseudospin $\uparrow\equiv |3z^2 - r^2\rangle$, $\downarrow\equiv |x^2 - y^2\rangle$. Constrained operators $\hat{c}_{i\alpha}^\dagger = c_{i\alpha}^\dagger(1 - n_i)$ create an electron only under the condition that the site is empty.

The first term of Eq. (3.1) describes the transfer of electrons between sites. In contrast to conventional spin models, the transfer-matrices are non-diagonal in orbital pseudospin:

$$t_{x/y}^{\alpha\beta} = t\left(\begin{array}{cc} 1/4 & \mp\sqrt{3}/4 \\ \mp\sqrt{3}/4 & 3/4 \end{array}\right), \quad t_z^{\alpha\beta} = t\left(\begin{array}{cc} 1 & 0 \\ 0 & 0 \end{array}\right).$$

The second term in Eq. (3.1) couples pseudospins between neighboring sites. The pseudospin operators are defined as

$$\tau_i^{x/y} = -\frac{1}{4}\left(\sigma_i^z \pm \sqrt{3}\sigma_i^x\right), \quad \tau_i^z = \frac{1}{2}\sigma_i^z,$$
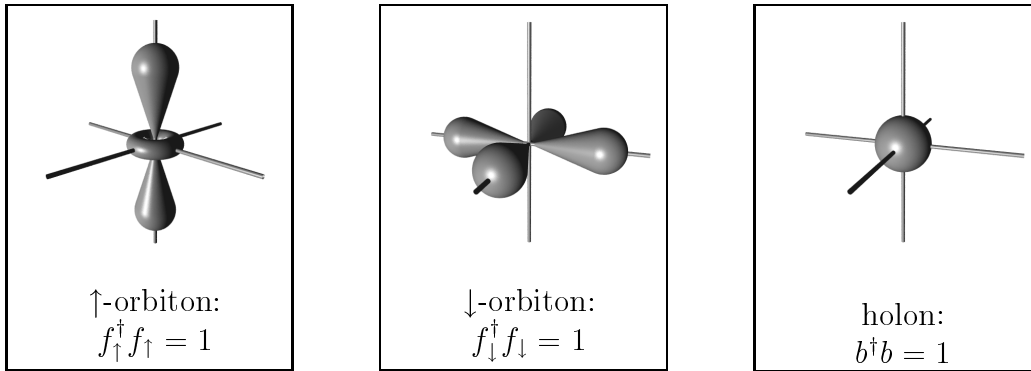
Figure 3.3: *Quasiparticles of the theory: Two fermionic orbitons with pseudospin* $\uparrow \equiv d_{3z^2-r^2}$ *and* $\downarrow \equiv d_{x^2-y^2}$ *and one bosonic holon.*

with Pauli matrices σ_i^x and σ_i^z acting on the orbital subspace. The strength of the pseudospin interaction in the above model is controlled by the super-exchange coupling constant $J = 2t^2/U_1$, where U_1 is the on-site repulsion between spin-parallel e_g electrons. We note that dynamic Jahn-Teller distortions of MnO_6 octahedra mediate an additional interaction between pseudospins that is of the same form as the above superexchange term [see Chap. 1, Eq. (1.8)]. The numerical value of J has to be chosen such as to comprise both effects.

The main problem in dealing with the t-J Hamiltonian of Eq. (3.1) is to correctly account for the constraint that forbids any sites from being doubly occupied. Following the discussion of Chap. 1, we employ an orbital-charge separation scheme that treats the constraint on average while preserving the main features of the strongly correlated state. The first step is to replace electron operators by two new quasiparticle operators:

$$c_{i\alpha}^\dagger = f_{i\alpha}^\dagger b_i. \tag{3.2}$$

Here $f_{i\alpha}^\dagger$ creates an orbiton that carries the electron's orbital quantum number and b_i destroys a holon that carries charge (see Fig. 3.3). These two types of quasiparticles are associated with orbital and charge fluctuations, respectively. At this point orbitons have to be assigned either fermionic or bosonic statistics; the holon then becomes a boson or a fermion, respectively. As we intend to describe a state in which orbital fluctuations are strong, a fermionic representation of the orbital sector is chosen. From analogy to the conventional t-J model, this scheme is expected to describe well an orbitally disordered state far from critical instabilities towards ordering. It should be noted, however, that short-range orbital correlations are not fully captured in this picture.

Orbitons and holons are subject to the local constraint $n_i^f + n_i^b = 1$ which assures that each site is either occupied by a single orbiton or holon. The major approximation step is to relax the local constraint to a global one, i.e., $\langle n_i^f \rangle + \langle n_i^b \rangle = 1$. The two types of quasiparticles can then be decoupled by introducing mean-field parameters

$$\chi = t^{-1} \sum_{\alpha\beta} t_\gamma^{\alpha\beta} \langle f_{i\alpha}^\dagger f_{j\beta} \rangle, \quad x = \langle b_i^\dagger b_j \rangle, \tag{3.3}$$

where x is the concentration of holes in the system. This yields two separate Hamiltonians that control the dynamics of orbitons and holons, respectively:

$$H_{\mathrm{orb}} = -x \sum_{\langle ij \rangle_\gamma} t_\gamma^{\alpha\beta} \left(f_{i\alpha}^\dagger f_{j\beta} + \mathrm{H.c.} \right), \tag{3.4}$$

$$H_{\mathrm{hl}} = -\chi t \sum_{\langle ij \rangle} \left(b_i^\dagger b_j + \mathrm{H.c.} \right). \tag{3.5}$$

Diagonalizing the above expressions in momentum space one obtains

$$H_{\mathrm{orb}} = \sum_{\boldsymbol{k}\nu} \xi_{\boldsymbol{k}}^\nu f_{\boldsymbol{k}\nu}^\dagger f_{\boldsymbol{k}\nu}, \tag{3.6}$$

$$H_{\mathrm{hl}} = \sum_{\boldsymbol{k}} \omega_{\boldsymbol{k}} b_{\boldsymbol{k}}^\dagger b_{\boldsymbol{k}}, \tag{3.7}$$

with index $\nu = \pm$ and dispersion functions

$$\xi_{\boldsymbol{k}}^\pm = (tx + J\chi) \left[-\epsilon_0(\boldsymbol{k}) \pm \sqrt{\epsilon_1^2(\boldsymbol{k}) + \epsilon_2^2(\boldsymbol{k})} \right],$$

$$\omega_{\boldsymbol{k}} = 6t\chi \left[1 - \frac{1}{3}\epsilon_0(\boldsymbol{k}) \right],$$

where $\epsilon_0(\boldsymbol{k}) = c_x + c_y + c_z$, $\epsilon_1(\boldsymbol{k}) = (c_x + c_y)/2 - c_z$, $\epsilon_2(\boldsymbol{k}) = \sqrt{3}(c_x - c_y)/2$ with $c_\gamma = \cos k_\gamma$. We hence obtain two fermionic bands of width $W_{\mathrm{orb}} = 6(tx + J\chi)$ and one bosonic band of half width $W_{\mathrm{hl}} = 12\chi t$; the dispersions are shown in Fig. 3.4. The two-fold degeneracy of e_g orbitals implies the existence of two orbiton bands. These do not coincide as a result of the non-diagonality of the transfer matrices $t_\gamma^{\alpha\beta}$. We note that a similar two-band structure was found by Shiba *et al.* for the case of free electrons [SHI97]. The presence of the electron-electron interaction turns these free bands into constrained Gutzwiller bands whose width is strongly quenched and now roughly scales with the concentration of holes. A similar reduction is also observable in the electronic quasiparticle weight in agreement with photoemission experiments: On a mean-field level the electronic quasiparticle weight scales with x. This follows from the fact that the electron Green's function $G^e(i\omega, \boldsymbol{k}) = -\langle T_\tau c_{\boldsymbol{k}}(\tau) c_{\boldsymbol{k}}^\dagger(0) \rangle_{i\omega}$ and the orbiton Green's function $G^{\mathrm{orb}}(i\omega, \boldsymbol{k}) = -\langle T_\tau f_{\boldsymbol{k}}(\tau) f_{\boldsymbol{k}}^\dagger(0) \rangle_{i\omega}$ are related by

$$G^e(i\omega, \boldsymbol{k}) \approx x G^{\mathrm{orb}}(i\omega, \boldsymbol{k}). \tag{3.8}$$
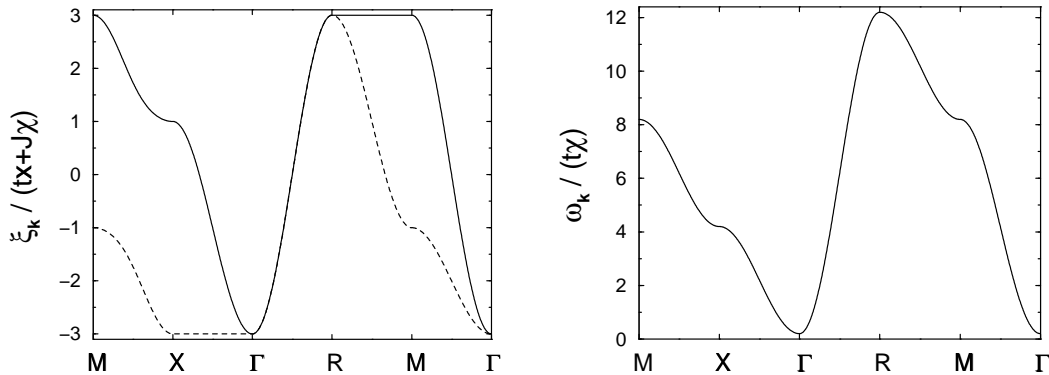
Figure 3.4: *Dispersion of orbitons (left) and holons (right) along the following direction in k space: $M(\pi, \pi, 0) \to X(0, \pi, 0) \to \Gamma(0, 0, 0) \to R(\pi, \pi, \pi) \to M(\pi, \pi, 0) \to \Gamma(0, 0, 0)$.*

3.3 Optical Conductivity

In this section we derive expressions for the optical conductivity of metallic manganites that are based on the orbital-liquid scheme discussed above. In calculating the optical conductivity, we choose to employ the memory-function formalism [GOE72, FOR75]. While not rigorous, this method yields exactly the leading terms of a high-energy expansion and is believed to give reasonably accurate results over the whole frequency range if no critical low-energy modes as in one-dimensional systems exist.

Within this framework, the optical conductivity $\sigma(\omega)$ is expressed via the memory function $M(\omega)$

$$\sigma(\omega) = \frac{i\chi_0}{\omega + M(\omega)}, \tag{3.9}$$

where $\chi_0 = \langle T_\tau J(\tau) J(0) \rangle_{i\omega \to 0^+}$ denotes the zero-frequency current-current correlation function. One of the advantages of the memory-function formalism over conventional linear-response theory is that the form of Eq. (3.9) resembles the classical Drude conductivity — the memory function $M(\omega)$ can be thought of as the quantum-mechanical counterpart of the classical relaxation rate. This suggests that the approximations necessary in calculating the memory function $M(\omega)$ preserve the overall shape of $\sigma(\omega)$. The memory function is defined as

$$M(\omega) = -\frac{1}{\omega \chi_0} \left[f(\omega) - f(0) \right], \tag{3.10}$$

where $f(\omega) = \langle T_\tau F(\tau) F(0) \rangle_{i\omega \to \omega + 0^+}$ is the correlation function of force operators F. These are given by the time derivative of the current operator

$F = [J, H]$. This commutator can, in general, be calculated without approximations, which is the second advantage of the memory-function formalism: Being based on the force-force rather than the current-current correlation function, higher order vertex corrections are automatically taken into account that would have to be inserted "by hand" in conventional linear-response theory.

The starting point of our calculation of the optical conductivity $\sigma(\omega)$ is the current operator which we commute with the Hamiltonian to obtain the force operator. Since the transport properties of metallic manganites are isotropic, we are free to choose a projection of the current operator along any spatial direction. For convenience we select the z direction in which the transfer matrix is diagonal in orbital pseudospin numbers ($\uparrow \equiv d_{3z^2-r^2}$ and $\downarrow \equiv d_{x^2-y^2}$):

$$J_z = -iet \sum_{\langle ij \rangle_z} \left(\hat{c}_{i\uparrow}^\dagger \hat{c}_{j\uparrow} - \text{H.c.} \right). \tag{3.11}$$

Next, the force operator is calculated by commuting Eq. (3.11) with the t term of Hamiltonian (3.1) — we drop the J term, assuming $J < t$ (for the superexchange contribution $J = 2t^2/U_1$ this follows from the assumption that U_1 is large). We thus obtain the following expression for the force operator:

$$F_z^t = -\frac{iet}{2} \sum_{i\gamma\delta} \sum_{\alpha\beta} \left(R_{i+\delta}^z - R_i^z \right) t_\gamma^{\alpha\beta} \left(B_{i\alpha} \hat{c}_{i+\delta\uparrow}^\dagger \hat{c}_{i+\gamma,\beta} + \text{H.c.} \right), \tag{3.12}$$

with

$$B_{i\alpha} = \left(2 - n_i + \sigma_i^z \right) \delta_{\alpha\uparrow} + \left(\sigma_i^x - i\sigma_i^y \right) \delta_{\alpha\downarrow},$$

where double occupancies of sites are excluded. We stress that the force operator of Eq. (3.12) has been calculated in an exact manner, i.e., the expression fully takes account of the local constraint. In a next step we determine the force-force correlation function which now necessitates to relax the constraint. For this we employ the orbital-liquid scheme introduced in Section 3.2. We do not go into further details here but rather refer the reader to Appendix A for the expressions obtained. At this place we only outline our approach — Fig. 3.5 shows the diagrams considered.

The diagrams of Fig. 3.5 are calculated by condensing the holon operators, i.e., substituting $b_i \approx \sqrt{x}$, and accounting for fluctuations around this mean-field value up to first order. Diagram (a) describes transitions between the two Gutzwiller bands of the orbital-degenerate system — these transitions are allowed due to the fact that the t term of Hamiltonian (3.1) is non-diagonal in orbital quantum numbers. Similar transitions were found in Ref. [SHI97] using a free-band model. The presence of electron correlations, however, strongly suppresses the spectral weight associated with this
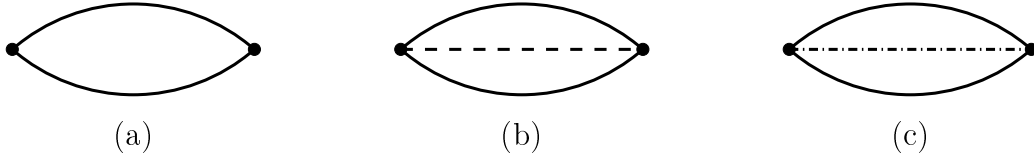
Figure 3.5: *Contributions to the force-force correlation function. Solid, dashed, and dot-dashed lines denote orbiton, holon, and pseudospin Green's functions, respectively.*
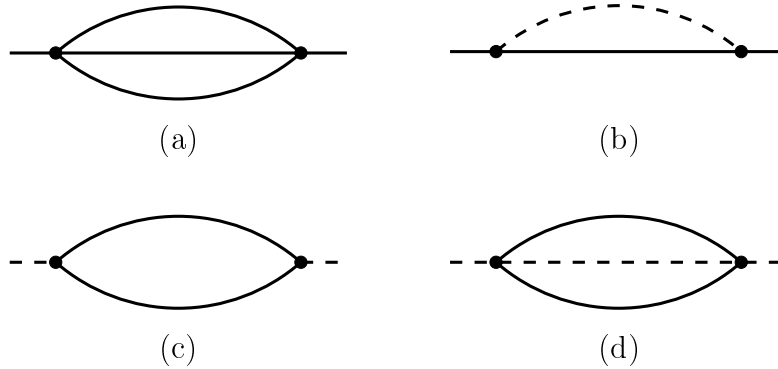
Figure 3.6: *Self energies of (a), (b) orbitons and (c), (d) holons.*

diagram and shifts its contribution to energies considerably lower than the free bandwidth. Diagram (a) is therefore not sufficient to account for the incoherency experimentally observed in the optical spectrum. Rather it is necessary to go beyond a simple Gutzwiller approximation and to consider correlation effects in a more thorough way. This is done in Diagrams (b) and (c) which purely originate from correlations among electrons. They describe transitions between highly incoherent bands. In the former diagram this incoherency stems from the composite nature of the electron, resulting in scattering of orbitons on holon fluctuations. In the latter diagram the incoherency is a consequence of fluctuations in the orbital sector which charge carriers scatter on. The contributions of Diagrams (b) and (c) to the optical conductivity spectrum extend approximately up to the bare fermionic bandwidth. They therefore play an essential role in explaining the incoherency of the optical spectrum. We note that the orbiton and holon propagators of Fig. 3.5 are "dressed," i.e., they are calculated with the self-energy corrections depicted in Fig. 3.6.

3.4   Comparison with Experiment

The absorptive part of the optical conductivity measured in experiment corresponds to the real part of Eq. (3.9). It consists of a zero-frequency Drude component

$$\sigma_D(\omega) = \pi \chi_0 \left[1 + \mathrm{Re} \left(\frac{\partial}{\partial \omega} M(\omega) \right) \right]_{\omega \to 0}^{-1} \delta(\omega) \tag{3.13}$$

and a regular part for finite frequencies

$$\sigma_{\mathrm{reg}}(\omega) = \mathrm{Re}[\sigma(\omega)]_{\omega > 0}. \tag{3.14}$$

We calculate the optical spectrum by evaluating the diagrams in Figs. 3.5 and 3.6. These contain several integrations over momentum space which we solve numerically using a Monte Carlo algorithm. The zero-frequency current-current correlation function χ_0 of Eqs. (3.9) and (3.10) is obtained from the orbiton mean-field Hamiltonian as $\chi_0 = 2x\chi te^2$. We choose a hole-doping concentration of $x = 17.5\%$ and set $J = 0.4t$. The value of the orbiton bond-order parameter is numerically determined to be $\chi = 0.25$, the lattice constant is set to 3.9 Å. The finite-frequency spectrum hence obtained is shown in Fig. 3.7 indicated by a solid line. We compare our theoretical result to experimental data of Okimoto, Katsufuji, Ishikawa, *et al.* [OKI95] represented by a dashed line. The only free parameter which we use to fit the theoretical to the experimental curve is the free fermionic bandwidth; this we fix by setting $t = 0.36$ eV consistent with band structure calculations [PIC96].

Good agreement between experiment and theory is found for intermediate and high frequencies. We stress that no additional fitting parameters are needed to obtain the correct absolute values of $\sigma_{\mathrm{reg}}(\omega)$. The total spectral weight consisting of the Drude part $\sigma_D(\omega)$ and the incoherent part $\sigma_{\mathrm{reg}}(\omega)$ is in agreement with experiment as can be seen from the effective charge-carrier concentration defined as

$$N_{\mathrm{eff}} = \frac{2m_0}{\pi e^2} \int_0^\infty d\omega [\sigma_D(\omega) + \sigma_{\mathrm{reg}}(\omega)], \tag{3.15}$$

where m_0 is the bare electron mass; theory and experiment [OKI95] both yield $N_{\mathrm{eff}} = 6\%$.

In the low-frequency region, the theoretical curve deviates from the experimental one as a pseudogap opens in the spectrum. As a consequence, our theory does not completely account for the weight transferred to the incoherent part of the spectrum: We obtain a ratio of Drude to incoherent weight of $35\% : 65\%$ which compares to $20\% : 80\%$ found experimentally [OKI95].
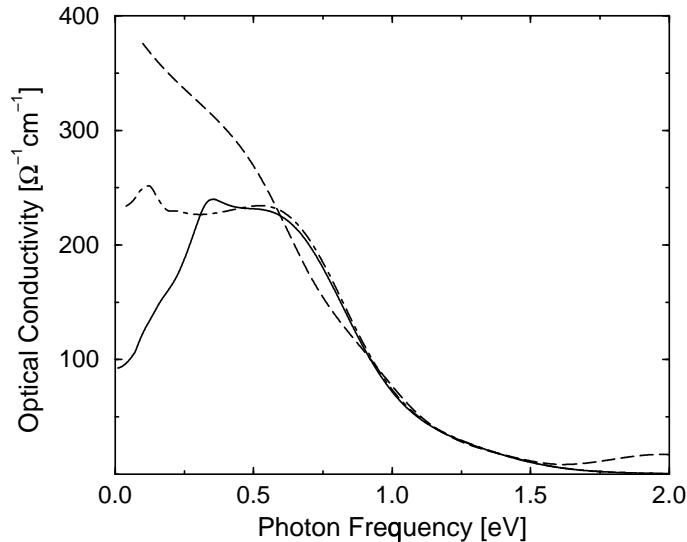
Figure 3.7: *Incoherent part of the optical conductivity $\sigma_{reg}(\omega)$ as a function of the photon frequency ω. The solid line represents the theoretical curve for $x = 17.5\%$ which is fitted to experimental data (dashed line) obtained by Okimoto et al. [OKI95] for $La_{1-x}Sr_xMnO_3$ at $T = 9$ K. The dot-dashed line corresponds to the theory including lattice effects.*

This discrepancy indicates an additional scattering mechanism to be active at low energies which is not yet incorporated in our theory. We speculate this mechanism to stem from the closeness of the real system to an orbitally ordered, Jahn-Teller-distorted state: Scattering on low-lying orbital collective modes as well as on phonons will enhance the low-energy region of the spectrum, thus filling the pseudogap. To make the latter point more explicit we calculate the conductivity including electron-phonon effects. Coupling of e_g pseudospins to double-degenerate Jahn-Teller phonons and of charge to the lattice breathing mode are described by (see Chap. 1):

$$H_{\mathrm{JT}} = -\lambda_{\mathrm{JT}} \sum_i \left[(a_i^\dagger + a_i)\sigma_i^z + i(a_i^\dagger - a_i)\sigma_i^x \right], \qquad (3.16)$$

$$H_{\mathrm{ch}} = -\lambda_{\mathrm{ch}} \sum_i (b_i^\dagger + b_i)(1 - n_i), \qquad (3.17)$$

respectively. Here $a_i^\dagger$ and $b_i^\dagger$ create Jahn-Teller and breathing-mode excitations. For simplicity phonons are considered to have dispersionless energy which we set to $\omega_0 = 0.05$ eV. Corrections to the force-force correlation function and to the fermionic self-energies are evaluated within a weak-coupling scheme, assuming the dimensionless coupling constant $\zeta = \lambda^2 N(\epsilon_F)/\omega_0$ to
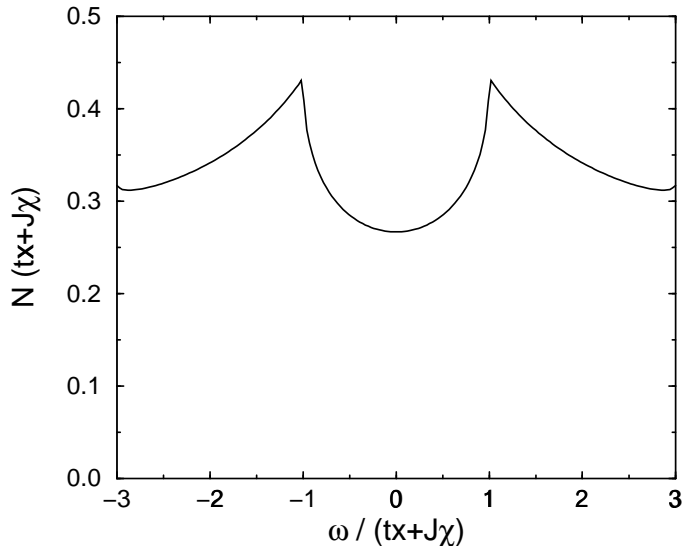
Figure 3.8: *The density of states of orbitons exhibits a pseudogap centered around the chemical potential at half filling.*

be small below T_C, where $N(\epsilon_F)$ is the total e_g density of states at the Fermi level. The result is shown for $\zeta_{JT} = \zeta_{ch} = 0.3$ by the dot-dashed line in Fig. 3.7. It suggests that lattice effects are present in the metallic ferromagnetic phase of manganites.

We finally calculate the constant of T-linear specific heat γ from the orbiton mean-field Hamiltonian which yields

$$\gamma = \frac{\pi^2}{3} N(\epsilon_F). \tag{3.18}$$

The orbiton density of states $N(\omega)$ is shown in Fig. 3.8. For $x = 17.5\%$ we find $\gamma = 7.2$ mJ/(mol K^2) as compared to experimental values 5 - 6 mJ/(mol K^2) [OKI95] and 3.3 mJ/(mol K^2) [WOO97]. While being slightly too large, our result still indicates that a strong-correlation description of the metallic phase of manganites is *not* in disaccord with the small values of specific heat observed experimentally. Our theory further correctly accounts for the experimental observation of γ being nearly independent of x. This follows from the fact that $N(\omega)(tx + J\chi)$ has a pseudogap centered around the chemical potential at half filling (see Fig. 3.8). At moderate hole-doping concentrations, γ is hence rather insensitive to changes in x. For $x = 30\%$ we in fact obtain $\gamma = 7.1$ mJ/(mol K^2).

3.5   Conclusion

In summary, we have calculated the optical absorption spectrum of ferromagnetic manganites. It is argued that there are clear experimental indications for the metallic state of manganites to be of strongly correlated nature. Employing an orbital-liquid picture to account for these correlation effects, we can successfully explain the incoherency seen in the optical spectrum that extends up to ≈ 1 eV. The theory is further in agreement with the amount of spectral weight shifted from zero to finite frequency accompanied by a strong suppression of the Drude weight. Consistency between our theory and the small values of T-linear specific heat obtained from experiment is achieved. The fact that the anomalous transport properties in the ferromagnetic phase are described well supports the validity of the orbital-liquid idea. The discrepancy between theory and experiment in the low-frequency part of the spectrum, namely the opening of a pseudogap, suggests that additional scattering mechanisms must be active. We illustrate that a phononic mechanism is capable of filling the low-frequency pseudogap, indicating the important role of lattice degrees of freedom even in the metallic state of manganites. In general it can be concluded that strong correlations play a crucial role in explaining the peculiar features of the metallic state of manganites.

Chapter 4

Magnon Softening in Ferromagnetic Manganites

4.1   Introduction

The motion of charge carriers in the metallic phase of manganites establishes a ferromagnetic interaction between spins on neighboring sites. According to the conventional theory of double exchange [ZEN51, AND55, DEG60], the spin dynamics of the ferromagnetic state that evolves at temperatures below T_C is expected to be of nearest-neighbor Heisenberg type. This picture seems to be indeed reasonably accurate for manganese oxides with high values of T_C, i.e., for compounds whose ferromagnetic metallic phase sustains up to rather high temperatures. However, recent experimental studies indicate marked deviations from this canonical behavior in compounds with low values of T_C. Quite prominent in this respect are measurements of the spin dynamics of the ferromagnetic manganese oxide $Pr_{0.63}Sr_{0.37}MnO_3$ [HWA98]: While exhibiting conventional Heisenberg behavior at small momenta, the dispersion of magnetic excitations (magnons) shows curious softening at the boundary of the Brillouin zone (see Fig. 4.1). This observation is of high importance as it indicates that some specific feature of magnetism in manganites has yet to be identified.

A comparison of the magnetic behavior of different manganese oxides further highlights the shortcomings of double-exchange theory: Assuming the magnon dispersion to be of Heisenberg type, a small-momentum fit to a quadratic dispersion relation $\omega = Dq^2$ yields the spin-wave stiffness D; in a conventional Heisenberg system the spin-wave stiffness scales with the strength of magnetic bonds $D \propto J$. Since the latter also controls the Curie temperature T_C, the ratio of D and T_C is expected to be a universal con-

High T_C → Low T_C

- Heisenberg-like magnon dispersion
- D/T_C small
- Double exchange

- Magnon softening at zone boundary
- D/T_C large
- Additional mechanism
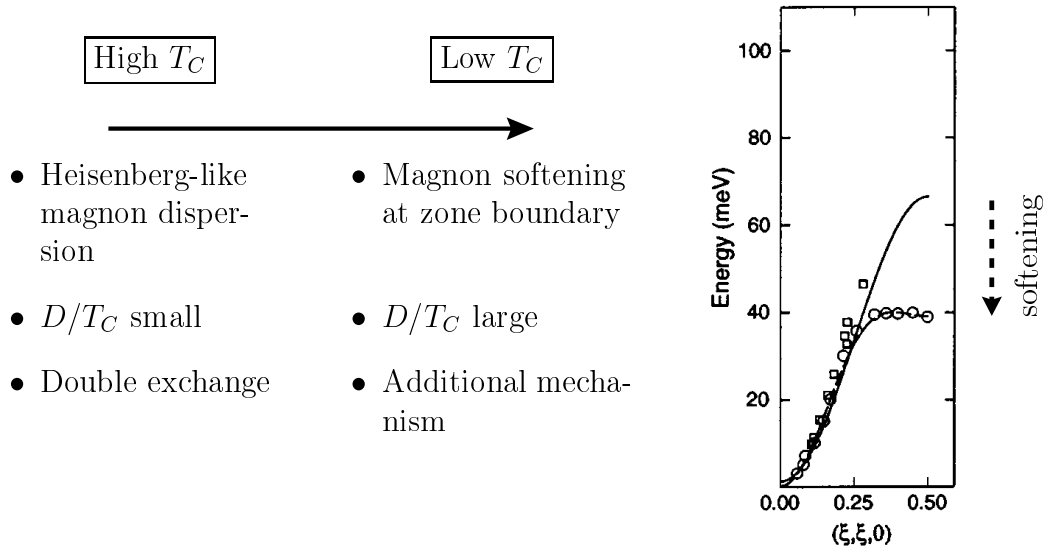
Figure 4.1: *Manganese oxides with high values of T_C (indicated by squares in the magnon dispersion on the right) exhibit nearest-neighbor Heisenberg-like spin dynamics. Compounds with low values of T_C (indicated by circles on the right), on the other hand, deviate from this behavior: The magnon dispersion softens at the Brillouin zone boundary. Low-T_C compounds further show an enhancement of the ratio of spin-wave stiffness D and Curie temperature T_C. See also Fig. 1.15 and Table 4.1. From [HWA98] (right).*

stant that depends only on the spin number. Manganites, on the other hand, exhibit a pronounced deviation from this behavior: As shown in Table 4.1, D/T_C increases significantly as one goes from compounds with high to compounds with low values of T_C [FER98]. The presence of an additional mechanism that controls the magnetic behavior of manganites is to be inferred.

In this chapter we propose a mechanism to explain the above peculiar magnetic properties of ferromagnetic manganites. Our basic idea is the following: The strength of the ferromagnetic interaction at a given bond strongly depends on the orbital quantum number of e_g electrons (see Fig. 4.2) — along the z direction, e.g., only electrons in $d_{3z^2-r^2}$ orbitals can hop between sites and can hence participate in double-exchange processes; the transfer of $d_{x^2-y^2}$ electrons is blocked due to the vanishing overlap with O $2p$ orbitals located in-between two neighboring Mn sites. Temporal fluctuations of e_g orbitals thus modulate the magnetic exchange bonds (see Fig. 4.3), thereby renormalizing the magnon dispersion. Short-wavelength magnons are most sensitive to these local fluctuations and are affected most strongly. Quantitatively the modulation of exchange bonds is controlled by the char-

Manganite	T_C [K]	D [meVÅ^2]	D/T_C [Å^2]	Ref.
$La_{0.7}Sr_{0.3}MnO_3$	378	188	5.8	[MAT96]
$La_{0.7}Pb_{0.3}MnO_3$	355	134	4.4	[PER96]
$Pr_{0.63}Sr_{0.37}MnO_3$	301	165	6.4	[FER98]
$La_{0.67}Ca_{0.33}MnO_3$	250	170	7.9	[LYN96]
$Nd_{0.7}Sr_{0.3}MnO_3$	198	165	9.7	[FER98]

Table 4.1: *The ratio of spin-wave stiffness D and Curie temperature T_C is enhanced in compounds with low values of T_C. From [FER98].*

$$J^c_{\mathrm{DE}} \propto t \qquad\qquad J^c_{\mathrm{DE}} = 0$$
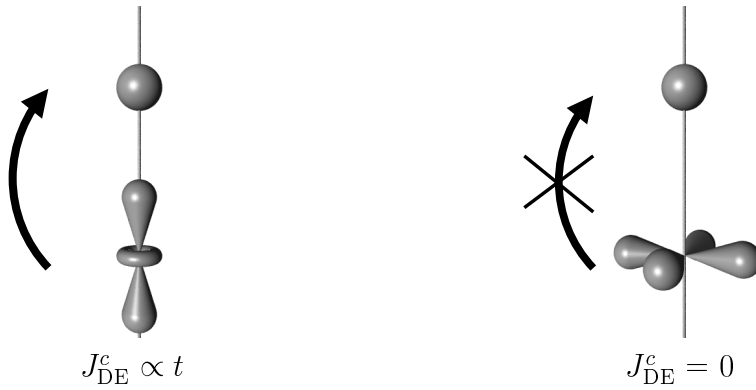
Figure 4.2: *The e_g-electron transfer amplitude, which controls the double-exchange interaction J_{DE}, strongly depends on the orbital orientation: Along the z direction, e.g., $d_{3z^2-r^2}$ electrons (bottom left) can hop into empty sites denoted by a sphere, while the transfer of $d_{x^2-y^2}$ electrons (bottom right) is forbidden.*

$$J^\perp_{\mathrm{DE}} = 0 \qqquad\qquad J^c_{\mathrm{DE}} = 0$$
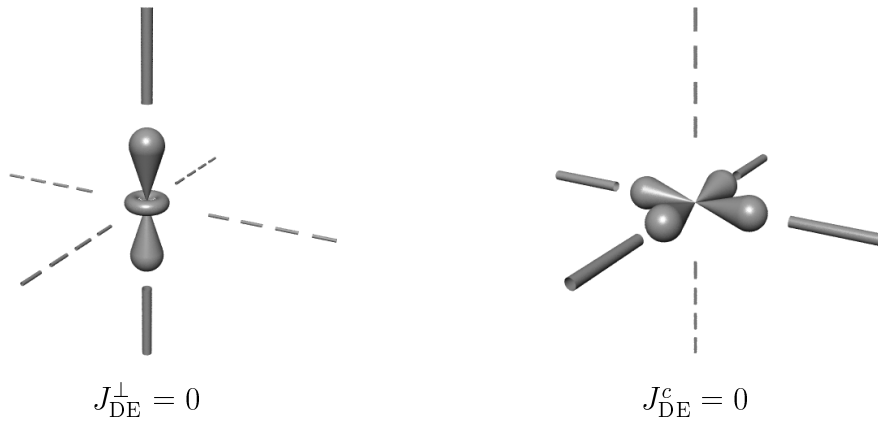
Figure 4.3: *Fluctuation of magnetic exchange bonds: Full lines denote active bonds, dashed lines inactive ones.*

acteristic time scale of orbital fluctuations: If the typical frequency of orbital fluctuations is higher than of spins fluctuations, the magnon spectrum remains mostly unrenormalized — the orbital state then effectively enters the spin dynamics only on time average which restores the cubic symmetry of exchange bonds. On the other hand, if orbitals fluctuate slower than spins, the magnon spectrum gets strongly renormalized — the anisotropy imposed upon the magnetic exchange bonds by the orbital degree of freedom now comes into play (see Fig. 4.3). The presence of Jahn-Teller phonons enhances this effect by quenching the dynamics of orbitals. The suppression of fluctuations becomes almost complete as orbitals begin to order, resulting in a distinct softening of magnons which we interprete as a precursor effect of static orbital order.

In the following we calculated the dispersion of one-magnon excitations at zero temperature. We start from the orbitally degenerate Hubbard model introduced in Chap. 1 which we treat in the limit of strong on-site repulsions. The magnetic double-exchange bonds established by the metallic motion of charge carriers are found to be further contributed to by virtual superexchange processes. Both types of magnetic interaction are of ferromagnetic nature in the orbitally degenerate system subject to a strong Hund's coupling. Employing a $1/S$ expansion of spin and an orbital-liquid scheme to handle correlation effects, three different mechanisms are analyzed with respect to their capability to renormalize the magnon spectrum: scattering of magnons on orbital fluctuations, charge fluctuations, and phonons. Within this picture we can successfully reproduce the experimentally observed softening of the magnon dispersion. Furthermore we predict the renormalization effect to become dramatic as static order in the orbital-lattice sector is approached. Recently the renormalization of the magnetic excitation spectrum by optical phonons has been investigated by Furukawa [FUR99].

4.2   Magnetic Exchange Bonds

The main aspects of the physics of manganites, i.e., the correlated motion of itinerant e_g electrons and the ferromagnetic interaction of e_g spins with a background of localized core spins, is captured by the orbitally degenerate Hubbard model introduced in Chap. 1:

$$
\begin{aligned}
H_{\text{Hub}} \;=\; & -\sum_{\langle ij\rangle_\gamma}\sum_{s\alpha\beta} t_\gamma^{\alpha\beta}\left(c_{is\alpha}^\dagger c_{js\beta}+\text{H.c.}\right)-J_H\sum_i \boldsymbol{S}_i^c \boldsymbol{s}_i \\
& +\sum_i\sum_\alpha U n_{i\uparrow\alpha}n_{i\downarrow\alpha}+\sum_i{\sum_{\alpha\neq\beta}}' \left(U'-J_H\hat{P}\right)n_{i\alpha}n_{i\beta}, \qquad (4.1)
\end{aligned}
$$

with $\hat{P} = (\boldsymbol{s}_{i\alpha}\boldsymbol{s}_{i\beta} + \frac{3}{4})$. Here $c_{is\alpha}^{\dagger}$ and $n_{is\alpha}$ denote creation and number operators of e_g electrons with spin and orbital quantum numbers s and α/β, respectively. The spatial direction of bonds is specified by $\gamma \in \{x, y, z\}$, and double counting is excluded from the primed sum. U and U' represent the intra- and inter-orbital Coulomb interaction between two e_g electrons on the same site and J_H is the strength of Hund's coupling. The spin operator $\boldsymbol{S}_i^c$ acts on core states and $\boldsymbol{s}_{i\alpha}$ on e_g electrons in orbitals α, while $\boldsymbol{s}_i = \sum_\alpha \boldsymbol{s}_{i\alpha}$. One of the important features of the orbitally degenerate model is the non-diagonal structure of the transfer matrices

$$t_{x/y}^{\alpha\beta} = t \begin{pmatrix} 1/4 & \mp\sqrt{3}/4 \\ \mp\sqrt{3}/4 & 3/4 \end{pmatrix}, \quad t_z^{\alpha\beta} = t \begin{pmatrix} 1 & 0 \\ 0 & 0 \end{pmatrix}, \quad (4.2)$$

where we have chosen a representation with respect to the orbital basis $\{|3z^2 - r^2\rangle, |x^2 - y^2\rangle\}$. Following the discussion of Chap. 1, we map Eq. (4.1) onto an orbitally degenerate t-J model applicable to strong on-site repulsions and large Hund's coupling:

$$\begin{aligned} H_{tJ} = & -\sum_{\langle ij\rangle_\gamma} \sum_{s\alpha\beta} t_\gamma^{\alpha\beta} \left(\hat{c}_{is\alpha}^{\dagger}\hat{c}_{js\beta} + \text{H.c.} \right) - J_H \sum_i \boldsymbol{S}_i^c \boldsymbol{s}_i \\ & -J_{\text{SE}} \sum_{\langle ij\rangle_\gamma} \left(\frac{1}{4} - \tau_i^\gamma\tau_j^\gamma \right) [\boldsymbol{S}_i\boldsymbol{S}_j + S(S+1)] n_i n_j. \quad (4.3) \end{aligned}$$

The orbital pseudospin operators are defined as

$$\tau_i^{x/y} = -\frac{1}{4} \left(\sigma_i^z \pm \sqrt{3}\sigma_i^x \right), \quad \tau_i^z = \frac{1}{2}\sigma_i^z,$$

with Pauli matrices $\sigma_i^{x/z}$ acting on the orbital subspace. The superexchange parameter is $J_{\text{SE}} = (2t^2/U_1)[S(2S+1)]^{-1}$, where S is the total on-site spin of $3d$ electrons and $U_1 = U' - J_H$ is the energy of the lowest-lying doubly occupied state reached by superexchange processes which is in a high-spin configuration. The constrained electron operators $\hat{c}_{is\alpha}^{\dagger} = c_{is\alpha}^{\dagger}(1 - n_i)$ in Eq. (4.3) create electrons at empty sites only.

The first line of Hamiltonian (4.3) describes the itinerant motion of correlated e_g electrons coupled ferromagnetically to the localized core spins. Due to the double-exchange mechanism, this motion establishes a ferromagnetic interaction between neighboring sites. Orbital degeneracy and the presence of on-site correlations strongly modify the conventional double-exchange picture. The second line of Hamiltonian (4.3) accounts for superexchange processes that involve virtual double occupancies of sites. As was discussed in Chap. 1, superexchange is of ferromagnetic nature in the orbitally degenerate system subject to Hund's coupling. The presence of a superexchange term
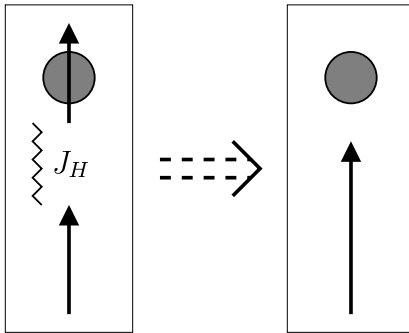
Figure 4.4: *The itinerant e_g spin (arrow top left) interacts with the localized core spins (bottom left) via Hund's coupling. In the limit $J_H \to \infty$, the former can be separated from the orbital and charge degrees of freedom of the e_g electron (circle) and be absorbed into the total spin (bottom right).*

in Eq. (4.3) is a direct consequence of the strong on-site repulsion between $3d$ electrons — conventional double-exchange theory neglects correlation effects and hence discards this contribution. In the following the two types of exchange interaction, which are jointly responsible for ferromagnetism in manganites, are treated in more detail.

4.2.1   Double-Exchange Bonds

We begin by analyzing the kinetic term of Hamiltonian (4.3),

$$H_t = - \sum_{\langle ij \rangle_\gamma} \sum_{s\alpha\beta} t_\gamma^{\alpha\beta} \left(\hat{c}_{is\alpha}^\dagger \hat{c}_{js\beta} + \text{H.c.} \right) - J_H \sum_i \boldsymbol{S}_i^c \boldsymbol{s}_i, \qquad (4.4)$$

which comprises the physics of double exchange. Due to the strong Hund's coupling core spins $\boldsymbol{S}^c$ and itinerant e_g spins $\boldsymbol{s}$ are not independent of each other but rather form a high-spin state with total on-site spin $S = S^c + \frac{1}{2}$. This unification of band and local spin subspaces suggests to decompose the e_g electron into its spin and orbital/charge components. The e_g spin can then be absorbed into the total spin, allowing an independent treatment of spin and orbital/charge degrees of freedom (see Fig. 4.4). The procedure of this separation scheme is the following: In a first step we introduce Schwinger bosons $d_{i\uparrow}$ and $d_{i\downarrow}$ (see, e.g., [AUE94]) to describe the e_g spin

$$s_i^+ = d_{i\uparrow}^\dagger d_{i\downarrow}, \quad s_i^- = d_{i\downarrow}^\dagger d_{i\uparrow}, \quad s_i^z = \frac{1}{2}(d_{i\uparrow}^\dagger d_{i\uparrow} - d_{i\downarrow}^\dagger d_{i\downarrow}), \qquad (4.5)$$

as well as Schwinger bosons $D_{i\uparrow}^\dagger$ and $D_{i\downarrow}^\dagger$ to model the total on-site spin

$$S_i^+ = D_{i\uparrow}^\dagger D_{i\downarrow}, \quad S_i^- = D_{i\downarrow}^\dagger D_{i\uparrow}, \quad S_i^z = \frac{1}{2}(D_{i\uparrow}^\dagger D_{i\uparrow} - D_{i\downarrow}^\dagger D_{i\downarrow}). \qquad (4.6)$$

These auxiliary particles are subject to the following constraint that depends on the e_g-electron occupation number n_i:

$$d^\dagger_{i\uparrow} d_{i\uparrow} + d^\dagger_{i\downarrow} d_{i\downarrow} = n_i, \tag{4.7}$$

$$D^\dagger_{i\uparrow} D_{i\uparrow} + D^\dagger_{i\downarrow} D_{i\downarrow} = 2S - 1 + n_i. \tag{4.8}$$

The creation and destruction operators for e_g-electrons can be expressed in terms of spinless fermions $c_{i\alpha}$ carrying charge as well as orbital pseudospin and Schwinger bosons carrying spin:

$$c_{is\alpha} = c_{i\alpha} d_{is}. \tag{4.9}$$

Rather than electrons the hopping term of Hamiltonian (4.4) now transfers pairs of spinless fermions and Schwinger bosons:

$$H_t = - \sum_{\langle ij \rangle_\gamma} \sum_{s\alpha\beta} t^{\alpha\beta}_\gamma \left(\hat{c}^\dagger_{i\alpha} \hat{c}_{j\beta} d^\dagger_{is} d_{js} + \text{H.c.} \right) - J_H \sum_i \boldsymbol{S}^c_i \boldsymbol{s}_i. \tag{4.10}$$

The Bose operators are subject to the constraint (4.7) that enforces the operators d_{is} and $d^\dagger_{is}$ to act only on projected Hilbert spaces with one or zero Schwinger bosons, respectively. Our aim is to absorb the e_g spin into the total spin, which requires to map the e_g-spin operators d_{is} onto D_{is} for the total spin. This is done by comparing the matrix elements of the two types of operators. On the one hand, keeping in mind that Hund's rule enforces the on-site spins to be always in a total-spin-symmetric state, the only non-vanishing matrix elements of the d_{is} operators are

$$\left\langle S - \tfrac{1}{2}, m - \tfrac{1}{2} \middle| d_\uparrow \middle| S, m \right\rangle = \sqrt{(S + m)/(2S)}, \tag{4.11}$$

$$\left\langle S - \tfrac{1}{2}, m + \tfrac{1}{2} \middle| d_\downarrow \middle| S, m \right\rangle = \sqrt{(S - m)/(2S)}. \tag{4.12}$$

In deriving the above expressions we have used the Clebsch-Gordan coefficients $\langle S^c, m^c; m^e | S, m \rangle$ to decompose the total-spin state $|S, m\rangle$ into core- and e_g-spin states $|S^c, m^c; m^e\rangle$ with $m^e = \uparrow / \downarrow$. These coefficients are given by

$$\left\langle S - \tfrac{1}{2}, m - \tfrac{1}{2}; \uparrow \middle| S, m \right\rangle = \left[\binom{S + m - 1}{2S - 1} \middle/ \binom{S + m}{2S} \right]^{1/2} = \left[\frac{S + m}{2S} \right]^{1/2},$$

$$\left\langle S - \tfrac{1}{2}, m + \tfrac{1}{2}; \downarrow \middle| S, m \right\rangle = \left[\binom{S - m - 1}{2S - 1} \middle/ \binom{S + m}{2S} \right]^{1/2} = \left[\frac{S - m}{2S} \right]^{1/2}.$$

On the other hand, the matrix elements of the D_{is} operators are

$$\left\langle S - \tfrac{1}{2}, m - \tfrac{1}{2} \middle| D_\uparrow \middle| S, m \right\rangle = \sqrt{(S + m)}, \tag{4.13}$$

$$\left\langle S - \tfrac{1}{2}, m + \tfrac{1}{2} \middle| D_\downarrow \middle| S, m \right\rangle = \sqrt{(S - m)}. \tag{4.14}$$

All other matrix elements vanish due to the constraint of Eq. (4.8).   By comparing Eqs. (4.11), (4.12) with Eqs. (4.13), (4.14) we find the mapping

$$d_{is} = \frac{1}{\sqrt{2S}} D_{is}. \tag{4.15}$$

The kinetic-energy Hamiltonian (4.10) can hence be rewritten in terms of total-spin operators D_{is}:

$$H_t = -\frac{1}{2S} \sum_{\langle ij \rangle_\gamma} \sum_{s\alpha\beta} t_\gamma^{\alpha\beta} \left(\hat{c}_{i\alpha}^\dagger \hat{c}_{j\beta} D_{is}^\dagger D_{js} + \text{H.c.} \right). \tag{4.16}$$

The Hund's coupling term of Eq. (4.10) has been dropped here as its presence is implied by the spin construction employed above.

At low temperatures the magnetic moment of ferromagnetic manganites studied here is almost fully saturated. It is therefore reasonable to expand Eq. (4.16) around a ferromagnetic groundstate. Technically this is done by condensing the spin-up Schwinger bosons (assuming the ferromagnetic moment to point along this direction) and by treating spin-wave excitations around this groundstate in leading order of $1/S$. Introducing magnon operators b_i, the following relations hold:

$$
\begin{aligned}
D_{i\uparrow} &= \sqrt{2S - b_i^\dagger b_i} \approx \sqrt{2S}\left(1 - \frac{1}{4S} b_i^\dagger b_i\right), \\
D_{i\downarrow} &= b_i.
\end{aligned}
$$

This spin representation fixes the number of Schwinger bosons per site to $2S$. The essence of the $1/S$ expansion is to consider the presence of a hole as a small perturbation which changes the spin projection S^z but not the spin magnitude S. Employing magnon operators, the kinetic-energy Hamiltonian (4.16) becomes

$$
\begin{aligned}
H_t &= -\sum_{\langle ij \rangle_\gamma} \sum_{\alpha\beta} t_\gamma^{\alpha\beta} \hat{c}_{i\alpha}^\dagger \hat{c}_{j\beta} \\
&\quad + \frac{1}{2S} \sum_{\langle ij \rangle_\gamma} \sum_{\alpha\beta} t_\gamma^{\alpha\beta} \hat{c}_{i\alpha}^\dagger \hat{c}_{j\beta} \left(\frac{1}{2} b_i^\dagger b_i + \frac{1}{2} b_j^\dagger b_j - b_i^\dagger b_j \right) \\
&\quad + \text{H.c.} \tag{4.17}
\end{aligned}
$$

The first term of Eq. (4.18) describes the motion of strongly correlated fermions in a ferromagnetic background. The second term controls the dynamics of spin excitations in the magnetic background and the interaction of these excitations with the fermionic sector. At small magnon numbers, i.e., at low

temperatures $T \ll T_C$, Eq. (4.17) can finally be mapped onto the following expression for the magnetic double-exchange bonds:

$$H_t = -\sum_{\langle ij \rangle_\gamma} \sum_{\alpha\beta} t_\gamma^{\alpha\beta} \hat{c}_{i\alpha}^\dagger \hat{c}_{j\beta} \Big[\frac{3}{4} + \frac{1}{4S^2} \left(S_i^z S_j^z + S_i^- S_j^+ \right) \Big] + \text{H.c.} \qquad (4.18)$$

The important point to be noticed here is that the amplitude of double-exchange bonds is a fluctuating complex quantity. Only when treating orbital and charge sectors on average, i.e., when replacing fermion operators $\hat{c}_{i\alpha}^\dagger \hat{c}_{i\beta}$ by their mean-field value $\langle \hat{c}_{i\alpha}^\dagger \hat{c}_{i\beta} \rangle$, an effective Heisenberg model as in a conventional mean-treatment of double exchange is obtained: $H = J_{\text{DE}} \sum_{\langle ij \rangle} \boldsymbol{S}_i \boldsymbol{S}_j$ with $J_{\text{DE}} = (2S^2)^{-1} \sum_{\alpha\beta} t_\gamma^{\alpha\beta} \langle \hat{c}_{i\alpha}^\dagger \hat{c}_{j\beta} \rangle$. In Section 4.3 we investigate in more detail the modification of this mean-field picture by fluctuations in the bond amplitude.

It is interesting to study Eq. (4.18) in the limiting case of classical spins. Replacing the spin operators by their classical counterparts $S^z = S \cos \theta$ and $S^\pm = S \sin \theta e^{\mp i\phi}$, an effective fermionic model is obtained:

$$H_t = -\sum_{\langle ij \rangle_\gamma} \sum_{\alpha\beta} \tilde{t}_\gamma^{\alpha\beta} \hat{c}_{i\alpha}^\dagger \hat{c}_{j\beta} + \text{H.c.} \qquad (4.19)$$

This model exhibits an unconventional feature, namely a phase-dependent hopping amplitude:

$$\tilde{t}_\gamma^{\alpha\beta} = t_\gamma^{\alpha\beta} \Big[\frac{3}{4} + \frac{1}{4} \left(\sin \theta_i \sin \theta_j + \sin \theta_i \sin \theta_j e^{i(\phi_i - \phi_j)} \right) \Big].$$

A similar result has been discussed in Refs. [MIL95, MUE96] in terms of a Berry-phase effect.

4.2.2   Superexchange Bonds

At low doping the virtual charge transfer across the Hubbard gap becomes of importance. These superexchange processes establish an inter-site interaction which in the limit of a strong Hunds coupling is described by [see Eq. (4.3)]:

$$H_J = -J_{\text{SE}} \sum_{\langle ij \rangle_\gamma} \left(\frac{1}{4} - \tau_i^\gamma \tau_j^\gamma \right) \left[\boldsymbol{S}_i \boldsymbol{S}_j + S(S+1) \right] n_i n_j. \qquad (4.20)$$

This term is discussed in detail in Chap. 1; here we only highlight the important features: First to be noted is the fact that Hund's coupling forbids any double occupancy of a single orbital. Pauli's exclusion principle, which is responsible for the antiferromagnetic nature of conventional superexchange,

is therefore ineffective in dictating the spin structure of the virtual intermediate state. Rather, the spin orientation in the intermediate state is controlled by Hund's coupling which favors a ferromagnetic alignment of spins. Superexchange in the present model is therefore of ferromagnetic nature. Furthermore, the amplitude of superexchange processes strongly depends on the orbital state of the e_g electrons involved — the factor $(\frac{1}{4} - \tau_i^\gamma \tau_j^\gamma)$ accounts for the specific non-diagonal structure of the transfer matrices $t_\gamma^{\alpha\beta}$ and ensures that no double occupancy of a single orbital occurs which would be forbidden by Pauli's exclusion principle and the large Hund's coupling.

For latter use we express the spin operators of Eq. (4.20) in terms of magnon operators b_i, yielding

$$
\begin{aligned}
H_J \;=\; & SJ_{\text{SE}} \sum_{\langle ij\rangle_\gamma} \left(\frac{1}{4} - \tau_i^\gamma \tau_j^\gamma\right) \\
& \times \left[\left(\frac{1}{2}b_i^\dagger b_i + \frac{1}{2}b_j^\dagger b_j - b_i^\dagger b_j + \text{H.c.}\right) - (2S+1)\right] n_i n_j. \quad (4.21)
\end{aligned}
$$

Equation (4.21) describes the interaction between magnons and orbital fluctuations and represents the superexchange counterpart of Eq. (4.17) which was derived for double-exchange bonds.

4.3   Magnon Dispersion

In the previous section the role of double-exchange and superexchange processes in promoting ferromagnetic exchange bonds in manganites was discussed. At intermediate doping levels these exchange interactions induce a ferromagnetic groundstate in a variety of manganese oxides. We now turn to analyze the propagation of magnetic excitations in this ferromagnetic phase, namely by deducing the dispersion relation of single-magnon excitations.

In a first step we derive the correct operator for creating a magnetic excitation in hole-doped double-exchange systems. It has to account for the fact that the total on-site spin depends on whether a hole or an e_g electron is present at that site: The spin number is $S - \frac{1}{2}$ in the former and S in the latter case. In general, a spin excitation is created by the operator S_i^+. Expressing this operator in terms of Schwinger bosons $S_i^+ = D_{i\uparrow}^\dagger D_{i\downarrow}$, condensing $D_{i\uparrow}$, and mapping $D_{i\downarrow}$ onto the magnon operator b_i, the following representation is obtained:

$$
S_i^+ = \begin{cases} \sqrt{2S}\, b_i & \text{for sites with } e_g \text{ electron,} \\ \sqrt{2S-1}\, b_i & \text{for sites with hole.} \end{cases} \quad (4.22)
$$

Assuming S to be the "natural" spin number of the system, the magnon operator b_i has to be rescaled by a factor $[(2S-1)/(2S)]^{1/2}$ when being applied to hole sites:

$$B_i = \begin{cases} b_i & \text{for sites with } e_g \text{ electron,} \\ \sqrt{(2S-1)/(2S)}\, b_i & \text{for sites with hole.} \end{cases} \tag{4.23}$$

The general magnon operator that automatically probes the presence of an e_g electron can finally be written as

$$B_i = b_i \left[n_i + \sqrt{\frac{2S-1}{2S}}(1-n_i) \right] \approx b_i - \frac{1}{4S}(1-n_i)\,b_i, \tag{4.24}$$

where n_i is the number operator of e_g electrons. B_i represents the true Goldstone operator of hole-doped double-exchange systems. Its composite character comprises local and itinerant spin features which is a consequence of the fact that static core and mobile e_g electrons together form the total on-site spin. While the itinerant part of B_i is of order $1/S$ only, it nevertheless is of crucial importance to ensure consistency of the spin dynamics with the Goldstone theorem, i.e., to yield an excitation mode whose energy vanishes at zero-momentum.

Having derived the correct magnon operator for doped double-exchange systems, we now study the propagation of the magnetic excitations created by this operator. The link between sites that allows a local excitation to spread throughout the system is established by the exchange-bond Hamiltonians (4.17) and (4.21). At low temperatures the dynamics of spin waves which hence develop is captured by the single-magnon dispersion. The important question we are interested in is: To which extent is the magnon spectrum affected by fluctuations in the exchange bonds? Our approach to answer this question is discussed in the following. We express the full magnon spectrum $\tilde{\omega}_{\boldsymbol{p}}$ in terms of the mean-field dispersion $\omega_{\boldsymbol{p}}$ and the magnon self energy $\Sigma(\omega, \boldsymbol{p})$:

$$\tilde{\omega}_{\boldsymbol{p}} = \omega_{\boldsymbol{p}} + \text{Re}[\Sigma(\omega_{\boldsymbol{p}}, \boldsymbol{p})]. \tag{4.25}$$

Fluctuation are considered only on average in the former but are explicitly accounted for in the latter term. The mean-field dispersion $\omega_{\boldsymbol{p}}$ as well as the scattering vertices needed to construct $\Sigma(\omega, \boldsymbol{p})$ can be derived by commuting the magnon operator B_i with the Hamiltonian. To be specific we explicitly perform this commutation, for now restricting ourselves to the double-exchange Hamiltonian H_t given by Eq. (4.17). In the momentum representation we obtain

$$[B_{\boldsymbol{p}}, H_t] = \omega_{\boldsymbol{p}} B_{\boldsymbol{p}} + \frac{t}{2S} \sum_{\boldsymbol{q}} \sum_{\alpha\beta} A_{\boldsymbol{p}}^{\alpha\beta}(\boldsymbol{k}) \hat{c}_{\boldsymbol{k}\alpha}^{\dagger} \hat{c}_{\boldsymbol{k}-\boldsymbol{q},\beta} B_{\boldsymbol{p}+\boldsymbol{q}}. \tag{4.26}$$

The two terms on the r.h.s. of Eq. (4.26) are derived by expanding the fermionic operators $\hat{c}_{i\alpha}^{\dagger}\hat{c}_{j\beta}$ around their average value:

$$\hat{c}_{i\alpha}^{\dagger}\hat{c}_{j\beta} \rightarrow \langle\hat{c}_{i\alpha}^{\dagger}\hat{c}_{j\beta}\rangle + \delta\left(\hat{c}_{i\alpha}^{\dagger}\hat{c}_{j\beta}\right).$$

The mean-field magnon dispersion $\omega_{\boldsymbol{p}}$ in the first term of Eq. (4.26) is of conventional nearest-neighbor Heisenberg form

$$\omega_{\boldsymbol{p}} = zD(1 - \gamma_{\boldsymbol{p}}), \tag{4.27}$$

with the form factor $\gamma_{\boldsymbol{p}} = z^{-1}\sum_{\boldsymbol{\delta}}\exp(i\boldsymbol{p}\boldsymbol{\delta})$, where $z = 6$, and the spin-wave stiffness constant $D = SJ_{\text{DE}}$. Exchange-bond fluctuations enter the coupling constant J_{DE} only on average: $J_{\text{DE}} = (2S^2)^{-1}\sum_{\alpha\beta} t_{\gamma}^{\alpha\beta}\langle\hat{c}_{i\alpha}^{\dagger}\hat{c}_{j\beta}\rangle$. The second term in Eq. (4.26) is the scattering vertex needed to construct the magnon self energy $\Sigma(\omega, \boldsymbol{p})$. It describes the interaction between magnons and orbital/charge fluctuations. The vertex function is

$$A_{\boldsymbol{p}}^{\alpha\beta}(\boldsymbol{k}) = \gamma_{\boldsymbol{k}}^{\alpha\beta} - \gamma_{\boldsymbol{k}+\boldsymbol{p}}^{\alpha\beta},$$

with form factors $\gamma_{\boldsymbol{k}}^{\alpha\beta} = (zt)^{-1}\sum_{\boldsymbol{\delta}} t_{\delta}^{\alpha\beta}\exp(i\boldsymbol{k}\boldsymbol{\delta})$.

Before we can engage in evaluating the magnon self energy associated with the scattering vertex in Eq. (4.26), the problem of dealing with the correlated nature of fermionic operators $\hat{c}_{i\alpha}^{\dagger} = c_{is}^{\dagger}(1 - n_i)$ has to be addressed. To handle the constraint that allows only for one e_g electron per site, we employ the orbital-liquid scheme introduced in Chap. 1: Orbital and charge degrees of freedom of the e_g electron are treated on separate footings by introducing "orbiton" and "holon" quasiparticles. To describe an orbitally disordered state in which orbitals fluctuate strongly, orbitons f_i are assigned fermionic and holons h_i bosonic statistics. The original fermion operators are hence reexpressed by

$$c_{i\alpha}^{\dagger} = f_{i\alpha}^{\dagger}h_i. \tag{4.28}$$

It is now possible to relax the local no-double-occupancy constraint to a global one:

$$n_i^f + n_i^h = 1 \quad \rightarrow \quad \langle n_i^f\rangle + \langle n_i^h\rangle = 1.$$

The main feature associated with the constrained nature of electrons, namely the separation of energy scales of orbital and charge dynamics, sustains this procedure due to the fact that two different types of quasiparticles are being used. Introducing mean-field parameters

$$\chi = t^{-1}\sum_{\alpha\beta} t_{\gamma}^{\alpha\beta}\langle f_{i\alpha}^{\dagger}f_{j\beta}\rangle, \quad x = \langle b_i^{\dagger}b_j\rangle, \tag{4.29}$$

where x is the concentration of holes, orbitons and holons can be decoupled as was shown in Chap. 1. We note that the two mean-field parameters in Eq. (4.29) are approximately related by $\chi = \frac{1}{2}(1 - x)$.

Employing representation (4.28), we reexpress the commutator of Eq. (4.26) in terms of orbiton and holon operators. Further taking into account the magnetic bonds stemming from superexchange processes as described by H_J in Eq. (4.21), we obtain

$$
\begin{aligned}
[B_{\boldsymbol{p}}, H] \;=\; & \omega_{\boldsymbol{p}} B_{\boldsymbol{p}} \\
& + \frac{t}{2S} \sum_{\boldsymbol{q}} \sum_{\alpha\beta} \left[x A_{\boldsymbol{p}}^{\alpha\beta}(\boldsymbol{k}) + x_0 B_{\boldsymbol{p}}^{\alpha\beta}(\boldsymbol{k}, \boldsymbol{q}) \right] f_{\boldsymbol{k}\alpha}^{\dagger} f_{\boldsymbol{k}-\boldsymbol{q},\beta} B_{\boldsymbol{p}+\boldsymbol{q}} \\
& + \frac{t\chi}{2S} \sum_{\boldsymbol{q}} C_{\boldsymbol{p}}(\boldsymbol{k}) h_{\boldsymbol{k}} h_{\boldsymbol{k}-\boldsymbol{q}}^{\dagger} B_{\boldsymbol{p}+\boldsymbol{q}},
\end{aligned}
\tag{4.30}
$$

where $H = H_t + H_J$ and $x_0 = 2\chi t / U_1$. Superexchange processes leave the mean-field magnon dispersion $\omega_{\boldsymbol{p}}$ qualitatively unaffected but enhance the spin-wave stiffness which now becomes $D = S(J_{\mathrm{DE}} + J_{\mathrm{SE}}) = t\chi(x + x_0)/(2S)$. Orbitons and holons have been decoupled in Eq. (4.30) by employing the mean-field parameters of Eq. (4.29). This yields two different types of scattering vertices, one describing the interaction between magnons and orbitons, the other between magnons and holons. The vertex functions are defined as

$$
\begin{aligned}
A_{\boldsymbol{p}}^{\alpha\beta}(\boldsymbol{k}) \;&=\; \gamma_{\boldsymbol{k}}^{\alpha\beta} - \gamma_{\boldsymbol{k}+\boldsymbol{p}}^{\alpha\beta}, \\
B_{\boldsymbol{p}}^{\alpha\beta}(\boldsymbol{k}, \boldsymbol{q}) \;&=\; \gamma_{\boldsymbol{k}}^{\alpha\beta} + \gamma_{\boldsymbol{k}-\boldsymbol{q}}^{\alpha\beta} - \gamma_{\boldsymbol{k}+\boldsymbol{p}}^{\alpha\beta} - \gamma_{\boldsymbol{k}-\boldsymbol{q}-\boldsymbol{p}}^{\alpha\beta}, \\
C_{\boldsymbol{p}}(\boldsymbol{k}) \;&=\; \gamma_{\boldsymbol{k}} - \gamma_{\boldsymbol{k}+\boldsymbol{p}}.
\end{aligned}
$$

The two contributions to the magnon self energy corresponding to the magnon-orbiton and magnon-holon scattering vertices of Eq. (4.30) are shown in Figs. 4.5(a) and (b). These capture the renormalization of the magnon spectrum due to orbital and charge fluctuations in the magnetic exchange bonds, respectively. The expressions corresponding to the Feynman diagrams in Fig. 4.5 are given in Appendix B.

An important piece of physics is still missed in the above considerations, namely the coupling of orbitals to the lattice. As is discussed in Chap. 1, the interaction between orbitals and two orthogonal Jahn-Teller lattice modes Q_2 and Q_3 is described by

$$
H_{\mathrm{JT}} = -\sum_i \left(g_2 Q_{2i} \sigma_i^x + g_3 Q_{3i} \sigma_i^z \right),
\tag{4.31}
$$

where the Pauli matrices $\sigma_i^{x/z}$ again act on the orbital subspace and the coupling constants $g_2 \approx g_3$. The crystal deformation energy including the
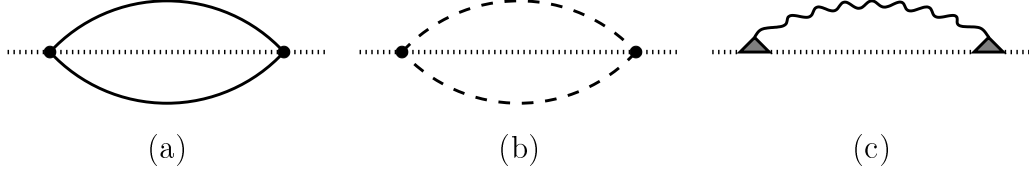
Figure 4.5: *Magnon self energies describing the effect of magnon scattering on (a) orbital fluctuations, (b) charge fluctuations, and (c) phonons. Solid, dashed, dotted, and wiggled lines denote orbiton, holon, magnon, and phonon propagators, respectively.*

effect of inter-site correlations is

$$H_{\text{ph}} = \frac{K}{2} \sum_i \boldsymbol{Q}_i^2 + K_1 \sum_{\langle ij \rangle_\gamma} Q_i^\gamma Q_j^\gamma, \qquad (4.32)$$

with $Q_i^{x/y} = (Q_{3i} \pm \sqrt{3} Q_{2i})/2$, $Q_i^z = Q_{3i}$, and $\boldsymbol{Q}_i = (Q_{2i}, Q_{3i})$. Equation (4.32) can be diagonalized in the momentum representation, yielding

$$H_{\text{ph}} = \sum_{\boldsymbol{k}\nu} \omega_{\boldsymbol{k}}^\nu a_{\boldsymbol{k}\nu}^\dagger a_{\boldsymbol{k}\nu}, \qquad (4.33)$$

with index $\nu = \pm$ and the phonon dispersions

$$\omega_{\boldsymbol{k}}^\pm = \omega_0 \left(\kappa_{1\boldsymbol{k}} \pm \sqrt{\kappa_{2\boldsymbol{k}}^2 + \kappa_{3\boldsymbol{k}}^2} \right)^{1/2}. \qquad (4.34)$$

Here $\kappa_{1\boldsymbol{k}} = 1 + k_1(c_x + c_y + c_z)$, $\kappa_{2\boldsymbol{k}} = k_1 \eta_{\boldsymbol{k}}^{(2)}$, $\kappa_{3\boldsymbol{k}} = k_1 \eta_{\boldsymbol{k}}^{(3)}$ with $k_1 = K_1/K$ and $\eta_{\boldsymbol{k}}^{(2)} = -\sqrt{3}(c_x - c_y)/2$, $\eta_{\boldsymbol{k}}^{(3)} = c_z - \frac{1}{2}c_x - \frac{1}{2}c_y$ with $c_\alpha = \cos k_\alpha$.

While there is no direct coupling between spins and phonons in the present system, lattice modes nevertheless strongly affects the spin dynamics. The link between spin and lattice is established via the orbital channel: The coupling of orbitals to the lattice imposing low phononic frequencies onto orbital fluctuations which enhances the modulation of magnetic exchange bonds. Thereby the effect of phonons extends onto the spin sector. To study this mechanism in more detail, we construct an effective spin-phonon coupling Hamiltonian from which we then calculate the phononic contribution to the magnon self energy. Combining the spin-orbital coupling term of the double-exchange Hamiltonian (4.17) with the orbital-lattice Hamiltonian (4.31) we obtain (see Fig. 4.6):

$$H_{\text{s-ph}} = -\sum_{\boldsymbol{pq}\nu} g_{\boldsymbol{pq}}^\nu (a_{\boldsymbol{q}\nu}^\dagger + a_{\boldsymbol{q}\nu}) B_{\boldsymbol{p}}^\dagger B_{\boldsymbol{p}+\boldsymbol{q}}. \qquad (4.35)$$

Figure 4.6: *Effective spin-phonon coupling vertex. The dominant contribution shown on the right stems from a combination of spin-orbital (filled dot $\propto t$) and orbital-lattice (open dot $\propto g_2$) coupling vertices. The orbital susceptibility depicted by a bubble controls the coupling strength. Solid, dotted and wiggled lines represent orbiton, magnon, and phonon propagators, respectively.*

The coupling constants in Eq. (4.35) are

$$
g_{\boldsymbol{pq}}^{+} = \left(\frac{E_{\mathrm{JT}}a_0^2\omega_0}{S^2}\right)^{1/2}\left(\frac{\omega_0}{\omega_{\boldsymbol{q}}^{+}}\right)^{1/2}\left(\lambda_{\boldsymbol{pq}}^{(3)}\cos\Theta_{\boldsymbol{q}} - \lambda_{\boldsymbol{pq}}^{(2)}\sin\Theta_{\boldsymbol{q}}\right),
$$

$$
g_{\boldsymbol{pq}}^{-} = \left(\frac{E_{\mathrm{JT}}a_0^2\omega_0}{S^2}\right)^{1/2}\left(\frac{\omega_0}{\omega_{\boldsymbol{q}}^{-}}\right)^{1/2}\left(\lambda_{\boldsymbol{pq}}^{(3)}\sin\Theta_{\boldsymbol{q}} + \lambda_{\boldsymbol{pq}}^{(2)}\cos\Theta_{\boldsymbol{q}}\right),
$$

with $\lambda_{\boldsymbol{pq}}^{(\alpha)} = (\eta_{\boldsymbol{q}}^{(\alpha)} - \eta_{\boldsymbol{p}}^{(\alpha)} - \eta_{\boldsymbol{p+q}}^{(\alpha)})$ and

$$
\cos\Theta_{\boldsymbol{q}} = \frac{1}{\sqrt{2}}\left(1 + \frac{\kappa_{3\boldsymbol{q}}}{\sqrt{\kappa_{2\boldsymbol{q}}^2 + \kappa_{3\boldsymbol{q}}^2}}\right)^{1/2},
$$

$$
\sin\Theta_{\boldsymbol{q}} = \frac{1}{\sqrt{2}}\left(1 - \frac{\kappa_{3\boldsymbol{q}}}{\sqrt{\kappa_{2\boldsymbol{q}}^2 + \kappa_{3\boldsymbol{q}}^2}}\right)^{1/2}\mathrm{sign}(\kappa_{2\boldsymbol{q}}).
$$

The strength of the spin-lattice interaction is controlled by the orbital susceptibility $\langle(f_{i+z,\uparrow}^{\dagger}f_{i\uparrow})(\sigma_i^z)\rangle_\omega$ which enters the parameter $a_0 = t(x + x_0)\langle(f_{i+z,\uparrow}^{\dagger}f_{i\uparrow})(\sigma_i^z)\rangle_{\omega=0}$; the zero-frequency limit is justified under the assumption that the energy scale of orbital fluctuations exceeds that of phonons. The phononic contribution to the magnon self energy that follows from Hamiltonian (4.35) is depicted in Fig. 4.5(c). The final expression for the self energy is given in Appendix B.

4.4   Comparison with Experiment

We are now in the position to evaluate the self energies of Fig. 4.5. Charge and orbital susceptibilities are calculated using mean-field Green's functions

in slave boson h_i and fermion f_i subspaces. For the spectral density of Jahn-Teller phonons in Fig. 4.5(c) we employ the expression

$$\rho_\pm^{\mathrm{ph}}(\omega, \boldsymbol{q}) = \frac{1}{\pi} \frac{\omega}{\omega_{\boldsymbol{q}}^\pm} \frac{\Gamma}{(\omega - \omega_{\boldsymbol{q}}^\pm)^2 + \Gamma^2}, \qquad (4.36)$$

which phenomenologically accounts for the damping Γ of phonons due to their coupling to orbital fluctuations. The phonon dispersion $\omega_{\boldsymbol{q}}^\pm$ is given by Eq. (4.34).

The expressions obtained from the diagrams in Fig. 4.5 contain summations over momentum space which we perform numerically using a Monte-Carlo algorithm. The result is shown in Fig. 4.7 by a solid line which we compare to experimental data of Ref. [HWA98] marked by circles. Furthermore, the bare mean-field dispersion $\omega_{\boldsymbol{p}}$ and the one containing only charge effects are shown by long-dashed and dashed lines, respectively. The following parameters are chosen: The hopping amplitude $t = 0.4$ eV is adjusted to fit the spin stiffness in $Pr_{0.63}Sr_{0.37}MnO_3$; further we use $U_1 = 4$ eV [FEI99]. The phonon contribution depends on the quantity $E_{\mathrm{JT}}a_0^2 \equiv (g_2 a_0)^2 / 2K$. We set $E_{\mathrm{JT}}a_2^2 = 0.004$ eV,[1] $\omega_0 = 0.08$ eV,[2] $\Gamma = 0.04$ eV, and $k_1 = -0.33$.

The effect of charge fluctuations onto the magnon spectrum is found to be quite featureless and moderate (see dashed line in Fig. 4.7). We attribute this to the fact that the spectral density of charge fluctuations lies well above the magnon band. On contrary, the fluctuations of the orbital ($\propto xt$) and lattice ($\propto \omega_0^{\mathrm{ph}}$) degrees of freedom are of rather low frequency and are hence found to affect the spin-wave dispersion in a pronounced way, particularly in $(0, 0, q)$ and $(0, q, q)$ directions. A key observations is the crucial effect of inter-site correlations of Jahn-Teller distortions — these are captured by the phononic dispersion being controlled by the parameter k_1. In order to explain the experimental data of Ref. [HWA98], we are forced to assume these correlations to be of *ferro-type*, i.e., $k_1 < 0$. We interpret this surprising result in the following way: Conventionally one would expect $k_1 > 0$ associated with a tendency of the orbital/lattice sector to develop antiferro-type order [KUG82]. In the hole-doped system this effect competes against charge mobility which prefers a ferro-type orbital orientation. The latter allows to minimize the kinetic energy by maximizing the transfer amplitude between sites. While Jahn-Teller lattice effects prevail at low doping, we believe the kinetic energy to dominate at large enough hole concentrations. This competition between Jahn-Teller effect and kinetic energy can be simulated by tuning the parameter k_1. We note that a layered ferro-type orbital

---

[1]A mean-field calculation gives $a_0 \approx 0.1$. Our fitting then implies a reasonable Jahn-Teller binding energy $E_{\mathrm{JT}} \approx 0.4$ eV.

[2]This number is consistent with optical reflectivity data in Ref. [OKI95].
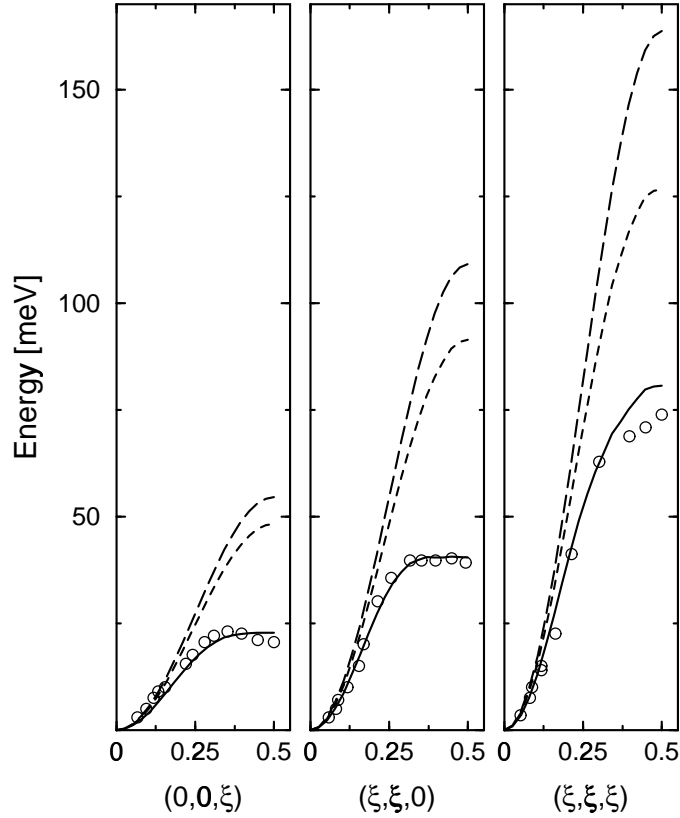
Figure 4.7: *Magnon dispersion along $(0,0,\xi)$, $(\xi,\xi,0)$, and (ξ,ξ,ξ) directions, where $\xi = 0.5$ at the cubic zone boundary. Solid lines represent the theoretical result obtained from a nearest-neighbor Hamiltonian including charge, orbital, and lattice effects and are fitted to experimental data denoted by circles (from Ref. [HWA98]). For comparison, the bare magnon dispersion and the one including only charge effects are indicated by long-dashed and dashed lines, respectively.*

order should be accompanied by a layered antiferromagnetic spin structure; the latter is fact experimentally observed at doping levels of about $x = 0.5$ [KAW97, MOT98]. As an instability towards an orbital-lattice ordered state is approached, exchange-bond fluctuations become very weak. In the magnon spectrum this is reflected by a strong enhancement of the renormalization effect as is shown in Fig. 4.8 for $k_1 \to -\frac{1}{3}$. We finally note that the softening of magnons at the zone boundary leads to a reduction of T_C. Remarkably, the small-q spin stiffness D remains unaffected which explains the anomalous enhancement of the D/T_C ratio in low-T_C manganites [FER98].

Figure 4.8: *Magnon dispersion including charge, orbital, and lattice effects. Different values for k_1 controlling the phonon dispersion are used. The softening enhances as $k_1 \to -\frac{1}{3}$ corresponding to a ferro-type orbital-lattice order. We set $E_{JT}a_0^2 = 0.006\ eV$.*
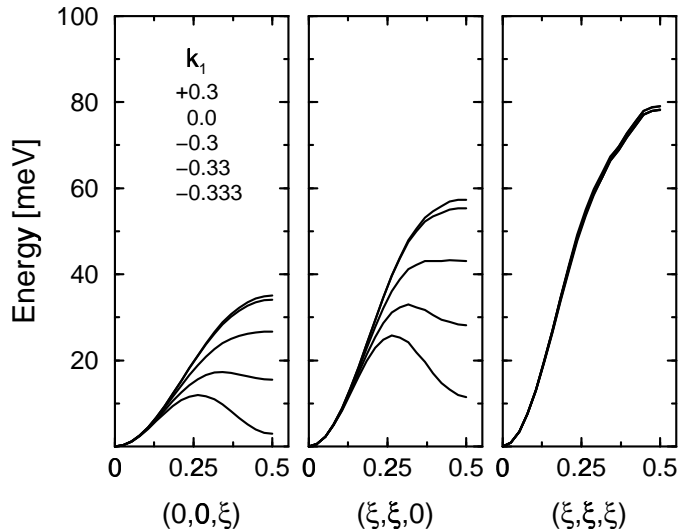
4.5 Conclusion

In summary, we have presented a theory of the spin dynamics in ferromagnetic manganites. Taking into account the orbital degeneracy and the correlated nature of e_g electrons, we analyzed the structure of magnetic exchange bonds; these are established by the inter-site transfer of electrons in coherent double-exchange and virtual superexchange processes. Orbital and charge fluctuations are shown to strongly modulate the exchange bonds, leading to a softening of the magnon excitation spectrum close to the Brillouin zone boundary. The presence of Jahn-Teller phonons further enhances the effect. This peculiar interplay between double-exchange physics and orbital-lattice dynamics becomes dominant close to the instability towards an orbital-lattice ordered state. The unusual magnon dispersion experimentally observed in low-T_C manganites can hence be understood as a precursor effect of orbital-lattice ordering. While the softening of magnons at the zone boundary is responsible for reducing the value of T_C, the small-momentum spin dynamics that enters the spin-wave stiffness D remains virtually unaffected. This explains the enhancement of the ratio D/T_C observed in low-T_C compounds. In general it can be concluded that strong correlations and orbital fluctuations play a crucial role in explaining the peculiar magnetic properties of manganites.

Chapter 5

Metal-Insulator Transition in Manganites

5.1 Introduction

The doping dependence of the properties of manganese oxides poses some
of the most interesting open problems in the physics of these compounds.
First to be noticed is the peculiar asymmetry of the phase diagram that is
most pronounced in the charge sector (see Fig. 5.1): Regions of high ($x >
0.5$) and low ($x < 0.5$) concentration of holes are characterized by such
contrasting phenomena as charge ordering and metalicity, respectively. In
the latter region — which we wish to focus on — the metallic state can be
turned into an insulating one by raising the temperature above the Curie
temperature T_C. Introducing the notion of double exchange which associates
the relative orientation of localized Mn t_{2g} spins with the mobility of itinerant
e_g electrons, early work has identified this transition to be controlled by the
loss of ferromagnetic order inherent to the metallic state [ZEN51, AND55,
DEG60]. It is believed that lattice effects are also of crucial importance in
this transition. Within the lattice-polaron double-exchange picture [ROE96,
MIL96a, MIL96b, MIL96c], the crossover from metallic to insulating behavior
is controlled by the ratio of polaron binding energy E_b to the kinetic energy
E_{kin} of charge carriers (see Fig. 5.2):

$$\lambda = \frac{E_b}{E_{\text{kin}}}. \tag{5.1}$$

When forming a bound state with the lattice, charge carriers loose part of
their kinetic energy. Hence, polarons are stable only if this loss in energy
is more than compensated by the gain in binding energy, i.e., if $\lambda > 1$. In
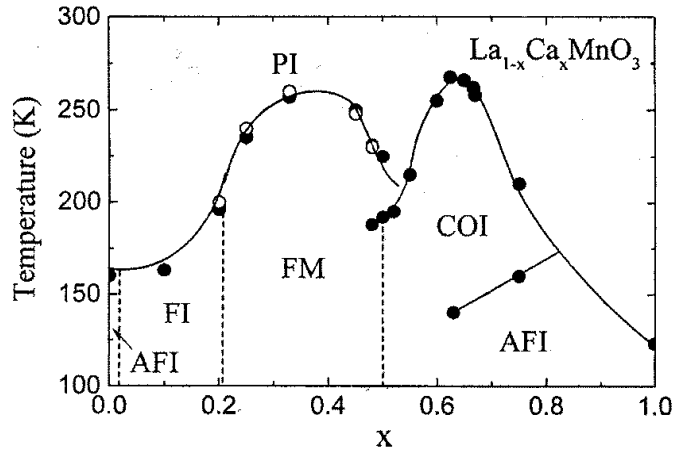a double-exchange system, this critical coupling strength may be reached

Figure 5.1: *Phase diagram of $La_{1-x}Ca_xMnO_3$. The phases are denoted by: anti-ferromagnetic insulator (AFI), ferromagnetic insulator (FI), ferromagnetic metal (FM), charge-ordered insulator (COI), and paramagnetic insulator (PI). From [RAM97].*

$E_{kin} > E_b$	$E_{kin} < E_b$
$\lambda < 1$	$\lambda > 1$
Metal	Insulator
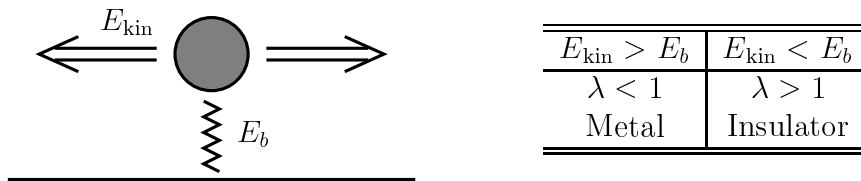
Figure 5.2: *Localization criterion in the lattice-polaron picture: Charge carriers localize if the energy gain E_b due to polaron formation exceeds the loss in kinetic energy E_{kin}. In double-exchange systems, E_{kin} can be tuned by temperature.*

by raising the temperature — the double-exchange mechanism then acts to reduce the kinetic energy and hence to increase λ. Spin disorder and spin-polaron effects further enhance the carrier localization above T_C [VAR96]. The doping dependence of the metal-insulator transition, however, is not fully captured in this picture. Namely the complete breakdown of metalicity at hole concentrations below $x_{crit} \approx 0.15$ - 0.2 that occurs despite the fact that ferromagnetism is fully sustained remains an open problem which we address in this chapter.

The effective coupling constant λ in Eq. (5.1) has originally been intro-duced for non-interacting electrons. The itinerant e_g electrons in mangan-ites, on the other hand, are subject to strong on-site repulsions which neces-sitates to accommodate the definition of λ. According to numerical studies [CAP99a, CAP99b], the basic physics underlying Eq. (5.1) remains valid even in correlated systems: As in the free-electron case, the metal-insulator transi-

Orbital Disorder-Order Transition	Orbital-Polaron Scenario

Low x	High x		Low x	High x
←			←	

orbital order	orbital disorder		slow orbital fluctuations	fast orbital fluctuations

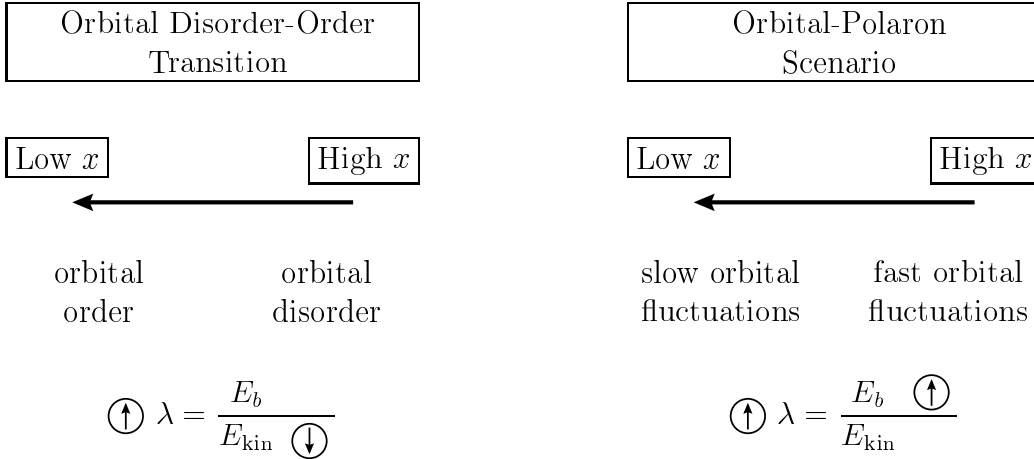$$\textcircled{\uparrow}\, \lambda = \frac{E_b}{E_{\text{kin}} \,\textcircled{\downarrow}}$$

$$\textcircled{\uparrow}\, \lambda = \frac{E_b \;\textcircled{\uparrow}}{E_{\text{kin}}}$$

Figure 5.3: *Possible mechanisms behind the doping dependence of the localization process: (Left) Below a critical value of x, an orbital disorder-order transition quenches the kinetic energy of holes, thereby enhancing the effective coupling constant λ. (Right) Holes polarize the orbital background and tend to form orbital-hole bound states. The binding energy is largest at low x where orbital fluctuations are weak.*

tion is controlled by the competition between the polaron binding energy and the kinetic energy of charge carriers. Nevertheless, correlation effects might renormalize these two relevant energy scales, presumably introducing a doping dependence. In fact, the Gutzwiller bandwidth of correlated electrons scales with the concentration of doped holes; one could therefore be inclined to set $E_{\text{kin}} \propto xt$, where t denotes the hopping amplitude. But this approach reaches too short: The Gutzwiller picture describes only the average kinetic energy of the system. In contrast, the relevant quantity for localizing the holes doped into a Mott-Hubbard system is the characteristic energy scale of charge fluctuations which remains $\propto t$ [DAG94]. Pictorially this quantity corresponds to the kinetic energy of a single hole. We thus conclude that a more thorough treatment of correlation effects is needed in order to explain the peculiar doping dependence of the metal-insulator transition in manganites.

In this chapter we analyze two mechanisms that could drive the localization of charge carriers at small hole concentrations x (see Fig. 5.3). First we explore the possibility of the metal-insulator transition to be controlled by a disorder-order crossover in the e_g-orbital sector. The idea is the following: Orbital fluctuations are induced by the motion of holes and hence possess an energy scale $\propto xt$. At large x, orbitals fluctuate strongly and inter-site

orbital correlations are weak. As the concentration of holes is reduced, fluctuations slow down until a critical value of x has been reached — promoted by Jahn-Teller and superexchange coupling, an orbital-lattice ordered state now evolves. We analyze the extent to which this transition in the orbital-lattice sector affects the itineracy of holes. Finding almost similar values for the kinetic energy of doped holes in orbitally ordered and disordered states we are lead to conclude that the development of orbital-lattice order is not sufficient to trigger the localization process. Next we turn to analyze a second scenario of the metal-insulator transition for which we introduce the concept of orbital polarons. Similar to spin polarons in correlated spin systems, orbital polarons are a natural consequence of strong electron correlations and the double degeneracy of on-site levels — in manganites the latter follows from the degeneracy of e_g orbitals. We argue that holes polarize the orbital state of e_g electrons on neighboring sites: A splitting of orbital levels is evoked by a displacement of oxygen ions and also by the Coulomb force exerted by the positively charged holes. Being comparable in magnitude to the kinetic energy of holes, the orbital-hole binding energy can be large enough for holes and surrounding orbitals to form a bound state. The important point is that the stability of these orbital polarons competes not only against the kinetic energy of holes but also against the fluctuation rate $\propto xt$ of orbitals: The faster the latter fluctuate, the less favorable it is to form a bound state in which orbitals have to give up part of their fluctuation energy. Combining this new orbital-polaron picture with that of conventional lattice polarons we are able to explain well the phase diagram of manganites at low and intermediate doping levels.

5.2   Orbital Disorder-Order Transition

In this section we analyze the impact of a disorder-order transition in the orbital-lattice sector onto the itineracy of holes. Our motivation is that a sudden freezing out of orbital fluctuations below a critical doping concentration could significantly impede the motion of holes, hence initiating the metal-insulator transition. By comparing the bandwidth of holes both in orbitally ordered and disordered states, we are able to refute this idea: The orbital sector is shown to have only little influence onto the charge mobility in manganites.

5.2.1 Disordered State

We begin by investigating the bandwidth of holes in a strongly fluctuating, orbitally disordered state. Our starting point is the t-J model of double-degenerate e_g electrons which, via Hund's coupling, interact ferromagnetically with an array of localized $S = 3/2$ core spins (see Chap. 1). The model accounts for the presence of strong on-site repulsions that forbids more than one e_g electron to occupy the same Mn site as well as for the double-degeneracy of e_g levels. At low temperatures and intermediate doping levels, the double-exchange mechanism induces a parallel alignment of spins. Treating deviations from this ferromagnetic ground state only on a mean-field level as is discussed below, the core spins can be discarded and the spin indices of e_g electrons may be dropped; the t-J Hamiltonian then becomes (see Chap. 3)

$$H_{tJ} = -\sum_{\langle ij \rangle_\gamma} \left(t_\gamma^{\alpha\beta} \hat{c}_{i\alpha}^\dagger \hat{c}_{j\beta} + \text{H.c.} \right) + \frac{2J}{z} \sum_{\langle ij \rangle_\gamma} \tau_i^\gamma \tau_j^\gamma, \tag{5.2}$$

with $z = 6$. Nearest-neighbor bonds along spatial directions $\gamma \in \{x, y, z\}$ are denoted by $\langle ij \rangle_\gamma$. We use constrained operators $\hat{c}_{i\alpha}^\dagger = c_{i\alpha}^\dagger (1 - n_i)$ which create an e_g electron at site i in orbital α only under the condition that the site is empty. The first term in Eq. (5.2) describes the inter-site transfer of constrained e_g electrons. The transfer amplitude depends upon the orientation of orbitals at a given bond as is reflected by the transfer matrices

$$t_{x/y}^{\alpha\beta} = t \begin{pmatrix} 1/4 & \mp\sqrt{3}/4 \\ \mp\sqrt{3}/4 & 3/4 \end{pmatrix}, \quad t_z^{\alpha\beta} = t \begin{pmatrix} 1 & 0 \\ 0 & 0 \end{pmatrix};$$

a representation with respect to the orbital basis $\alpha \in \{|3z^2 - r^2\rangle, |x^2 - y^2\rangle\}$ has been chosen here. Due to its non-diagonal structure, orbital quantum numbers are not conserved by Hamiltonian (5.2) – inter-site transfer processes induce fluctuations in the orbital sector. The second term in Eq. (5.2) accounts for processes involving the virtual occupation of sites by two e_g electrons. This superexchange mechanism establishes an inter-site coupling between orbital pseudospins of overall strength $J = zt^2/U_1$, where U_1 is the on-site repulsion between spin-parallel e_g electrons. The pseudospin operators are

$$\tau_i^{x/y} = -\frac{1}{4}(\sigma^z \pm \sqrt{3}\sigma^x), \quad \tau_i^z = \frac{1}{2}\sigma^z, \tag{5.3}$$

with Pauli matrices $\sigma_i^{x/z}$ acting on the orbital subspace. Jahn-Teller phonons mediate an additional interaction between orbital pseudospins which is of the exact same form as the superexchange term (see Chap. 1). The numerical

value of J has to be chosen such as to comprise both effects. We finally note that deviations from the ferromagnetic ground state underlying Hamiltonian (5.2) are treated within conventional double-exchange theory. The transfer amplitude t then depends on the normalized magnetization m via [KUB72, MIL95]

$$t = t_0\sqrt{(1 + m^2)/2}, \tag{5.4}$$

where t_0 denotes the hopping amplitude between spin-parallel Mn sites.

To observe the strongly correlated nature of e_g electrons, it is convenient to introduce separate particles for charge and orbital degrees of freedom [ISH97a]. As was shown in the last two chapters, the metallic phase of manganites can be well described within an orbital-liquid picture that accounts for orbital fluctuations by employing a slave-boson representation of electron operators:

$$c_{i\alpha}^\dagger = f_{i\alpha}^\dagger b_i.$$

Here orbital pseudospin is carried by fermionic orbitons $f_{i\alpha}$ and charge by bosonic holons b_i. Introducing mean-field parameters $\chi = t^{-1}\sum_{\alpha\beta} t_\gamma^{\alpha\beta}\langle f_{i\alpha}^\dagger f_{i\beta}\rangle$ and $x = \langle b_i^\dagger b_j\rangle$, where x is the concentration of holes and $\chi \approx \frac{1}{2}$, the two types of quasiparticles can be decoupled:

$$H_{\mathrm{orb}} = -\left(x + \frac{2\chi J}{zt}\right)\sum_{\langle ij\rangle_\gamma} t_\gamma^{\alpha\beta}\left(f_{i\alpha}^\dagger f_{j\beta} + \mathrm{H.c.}\right), \tag{5.5}$$

$$H_{\mathrm{hl}} = -\chi t\sum_{\langle ij\rangle}\left(b_i^\dagger b_j + \mathrm{H.c.}\right). \tag{5.6}$$

Diagonalizing the above expressions in the momentum representation one obtains

$$H_{\mathrm{orb}} = \sum_{\boldsymbol{k}\nu}\xi_{\boldsymbol{k}}^\nu f_{\boldsymbol{k}\nu}^\dagger f_{\boldsymbol{k}\nu}, \quad H_{\mathrm{hl}} = \sum_{\boldsymbol{k}}\omega_{\boldsymbol{k}} b_{\boldsymbol{k}}^\dagger b_{\boldsymbol{k}},$$

with index $\nu = \pm$ and dispersion functions

$$\xi_{\boldsymbol{k}}^\pm = (xt + \frac{2\chi J}{z})\left[-\epsilon_0(\boldsymbol{k}) \pm \sqrt{\epsilon_1^2(\boldsymbol{k}) + \epsilon_2^2(\boldsymbol{k})}\right],$$

$$\omega_{\boldsymbol{k}} = 6\chi t\left[1 - \frac{1}{3}\epsilon_0(\boldsymbol{k})\right],$$

where $\epsilon_0(\boldsymbol{k}) = c_x + c_y + c_z$, $\epsilon_1(\boldsymbol{k}) = (c_x + c_y)/2 - c_z$, $\epsilon_2(\boldsymbol{k}) = \sqrt{3}(c_x - c_y)/2$ with $c_\gamma = \cos k_\gamma$. The essence of this slaved-particle mean-field treatment is that orbital and charge fluctuations are assigned different energy scales. This is reflected by the bandwidths of orbiton and holon quasiparticles, respectively:

$$W_{\mathrm{orb}} = 6xt + J, \tag{5.7}$$

$$W_{\mathrm{hl}} = 6t. \tag{5.8}$$

The former quantity W_{orb} sets the energy scale of orbital fluctuations — the terms proportional to xt and J describe fluctuations induced by the motion of holes and by the coupling between pseudospins, respectively. The latter quantity W_{hl} finally defines the itineracy of holes in the orbital-liquid state. The variation of the holon bandwidth with the onset of orbital order is in the focus of our interest in the remainder of this section.

5.2.2 Instability Toward Orbital Order

The above treatment of orbital and charge fluctuations is based upon the notion of a strongly fluctuating orbital state that is far from any instability towards orbital order. In real systems such instabilities do exist: Jahn-Teller phonons and superexchange processes mediate a coupling between orbitals on neighboring sites which introduces a bias towards orbital-lattice ordering (see Chap. 1). Competing against the energy scale of orbital fluctuations $\propto xt$, order in the orbital sector is expected to evolve below a critical doping concentration x_{crit}. We investigate this instability of the orbital-liquid state by introducing the inter-site coupling term

$$H_J = -\frac{2J}{z} \sum_{\langle ij \rangle_\gamma} \tau_i^\Theta \tau_j^\Theta \, e^{iQ\gamma}, \tag{5.9}$$

with $z = 6$ and $\tau_i = (\sin\Theta\sigma_i^x + \cos\Theta\sigma_i^z)/2$ acting on the orbital subspace. We note that Eq. (5.9) is a simplification of the superexchange coupling term in Hamiltonian (5.2) — internal frustration makes the latter difficult to handle. For $\Theta = \pi/2$ and $\boldsymbol{Q} = (\pi, \pi, 0)$, the pseudospin interaction in Eq. (5.9) favors a staggered-type orbital orientation

$$|\Theta\rangle^\pm = \left(|3z^2 - r^2\rangle \pm |x^2 - y^2\rangle\right)/\sqrt{2} \tag{5.10}$$

within xy planes repeating itself along the z direction; this closely resembles the type of order observed experimentally in LaMnO$_3$ [MUR98] (see Fig. 5.4). The breakdown of the orbitally disordered state, i.e., the development of orbital order, is signaled by a singularity in the static orbital susceptibility $\langle\sigma_{\boldsymbol{Q}}^x \sigma_{-\boldsymbol{Q}}^x\rangle_{\omega=0}$. Employing a random-phase approximation (see Fig. 5.5), the latter can be expressed as

$$\langle\sigma^x\sigma^x\rangle_{\boldsymbol{Q}} = \frac{\langle\sigma^x\sigma^x\rangle_{\boldsymbol{Q}}^0}{1 + J_{\boldsymbol{Q}}\langle\sigma^x\sigma^x\rangle_{\boldsymbol{Q}}^0/2}, \tag{5.11}$$

with vertex function $J_{\boldsymbol{q}} = J\left(\cos q_x + \cos q_y - \cos q_z\right)/3$ and the shorthand notation $\langle\sigma^x\sigma^x\rangle_{\boldsymbol{Q}} = \langle\sigma_{\boldsymbol{Q}}^x\sigma_{-\boldsymbol{Q}}^x\rangle_{\omega=0}$. Bare orbital susceptibilities $\langle\ldots\rangle^0$ are evaluated using orbiton propagators associated with the mean-field Hamiltonian
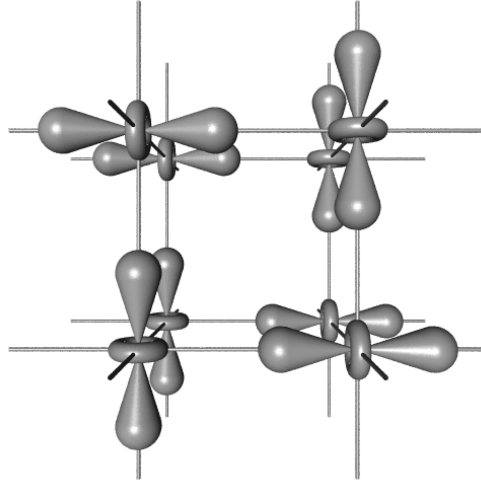
Figure 5.4: *Experimentally a staggered type of orbital order is observed within xy planes of LaMnO$_3$ which repeats itself along the z direction [MUR98].*
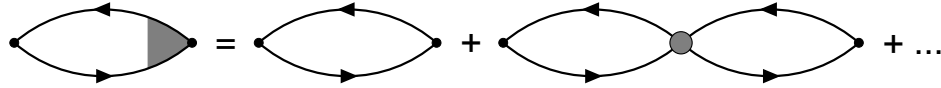

Figure 5.5: *Diagrammatic representation of the RPA expansion of the orbital susceptibility $\langle \sigma_{\boldsymbol{Q}}^x \sigma_{-\boldsymbol{Q}}^x \rangle_\omega$. The vertex function $J_{\boldsymbol{q}}$ is denoted by a circle.*

(5.5). Numerically solving for the pole in Eq. (5.11), we find the following expression for the critical doping concentration:

$$x_{\mathrm{crit}} \approx \frac{J}{4t}, \qquad (5.12)$$

which is valid for $x_{\mathrm{crit}} \ll 0.5$. At concentrations below this critical value an orbitally ordered state is to be expected. With $J = 0.13$ eV as estimated from the structural phase transition observed in LaMnO$_3$ at $T = 780$ K [MUR98] and $t = 0.36$ eV we obtain a critical doping concentration of $x_{\mathrm{crit}} = 9\%$. This result indicates that the metallic state of manganites is indeed instable towards orbital-lattice ordering at doping concentrations that are not too far from those at which the system is observed to become insulating.

5.2.3   Ordered State

Up to this point we have studied the bandwidth of holes in an orbitally disordered state and the instability of the system towards orbital-lattice order. In the following we analyze to which extent the itineracy of holes is
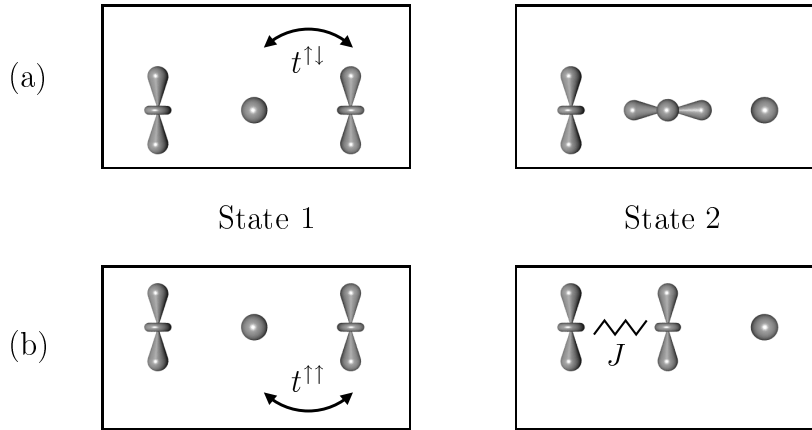
Figure 5.6: *Coherent (a) and incoherent (b) hole motion in antiferro-type orbital order. Incoherent processes involve the creation of an orbital excitation of energy J.*

affected by this disorder-order transition in the orbital sector. Namely we are interested in the bandwidth of holes moving through an orbitally ordered state; this quantity is then compared to our previous result of Eq. (5.8) for an orbital liquid. Foremost an important difference between models with orbital pseudospin and conventional spin is to be noticed here: In the latter systems, spin is conserved when electrons hop between sites. This implies that hole motion is constrained in a staggered spin background. In contrast, the transfer Hamiltonian (5.2) of the orbital model is non-diagonal in orbital pseudospin — an orbital basis in which all three transfer matrices $t_x^{\alpha\beta}$, $t_y^{\alpha\beta}$, and $t_z^{\alpha\beta}$ are of diagonal structure does not exist. This allows holes to move coherently even within an antiferro-type orbital arrangement [see Fig. 5.6(a)]. For this reason only a moderate suppression of the hole bandwidth is to be expected in the presence of orbital order. We calculate the bandwidth for the specific type of orbital order introduced in Eq. (5.10). Starting from the transfer part of Hamiltonian (5.2) and keeping only the hopping matrix elements that allow for a coherent movement of holes (i.e., projecting out all orbitals which do not comply with the ordered state) we obtain

$$W_{\mathrm{hl}}^{\mathrm{coh}} = 4t. \tag{5.13}$$

This result indicates a reduction of the holon bandwidth by $\approx 30\%$ as compared to the disordered state [see Eq. (5.8)]. While not being dramatic, a quenching of the bandwidth by one third should nevertheless be sufficient to induce the localization process, e.g., via the formation of lattice polarons.

However, it is important to note that Eq. (5.13) accounts solely for the co-
herent motion of holes; incoherent processes involving the creation and sub-
sequent absorption of orbital excitations are neglected [see Fig. 5.6(b)]. Only
if the ordered state is robust, i.e., if it costs a large amount of energy for
an electron to occupy an orbital that does not comply with the long-range
orbital alignment, these incoherent processes become negligible. This limit
does not apply to manganites where the orbital excitation energy is $J < t$
only. Before a conclusion about the role of orbital order in the metal-insulator
transition can be drawn, these incoherent processes have to be investigated
in more detail.

In the following we study the influence of incoherent processes onto the
motion of holes, employing an "orbital wave" approximation: Starting from
the assumption that long-range orbital order has developed and that fluctu-
ations around this ordered state are weak, we use a slave-fermion represen-
tation of the electron operators in the transfer Hamiltonian (5.2):

$$c_{i\alpha}^{\dagger} = b_{i\alpha}^{\dagger} f_i.$$

Within this picture, the orbital pseudospin is assigned to bosonic orbitons and
charge to fermionic holons. The lattice is then divided into two sublattices
which are ascribed different preferred pseudospin directions [see Eq. (5.10)]:

$$\uparrow \ \equiv \ \left(|3z^2 - r^2\rangle + |x^2 - y^2\rangle \right)/\sqrt{2} \quad \text{on sublattice } A,$$

$$\downarrow \ \equiv \ \left(|3z^2 - r^2\rangle - |x^2 - y^2\rangle \right)/\sqrt{2} \quad \text{on sublattice } B.$$

In analogy to conventional spin-wave theory [AUE94], excitations around this
ground state can be treated by employing the following mapping of orbiton
operators $b_{i\alpha}$ onto "orbital-wave" operators β_i:

$$b_{i\uparrow} = \left\{ \begin{array}{ll} 1 & \text{sublattice } A, \\ \beta_i & \text{sublattice } B, \end{array} \right. \qquad b_{i\downarrow} = \left\{ \begin{array}{ll} \beta_i & \text{sublattice } A, \\ 1 & \text{sublattice } B. \end{array} \right.$$

In the momentum representation the transfer Hamiltonian (5.2) then be-
comes

$$H_t = \sum_{\boldsymbol{k}} \omega_{\boldsymbol{k}} f_{\boldsymbol{k}}^{\dagger} f_{\boldsymbol{k}} + \sum_{\boldsymbol{k}\boldsymbol{p}} \left[\gamma_{\boldsymbol{k}} \beta_{\boldsymbol{p}}^{\dagger} + \gamma_{\boldsymbol{k}+\boldsymbol{p}} \beta_{-\boldsymbol{p}} \right] f_{\boldsymbol{k}}^{\dagger} f_{\boldsymbol{k}+\boldsymbol{p}}. \qquad (5.14)$$

Here $\omega_{\boldsymbol{k}} = -t(c_x + c_y - 2c_z)/2$ and $\gamma_{\boldsymbol{k}} = t[(2 - \sqrt{3})c_x + (2 + \sqrt{3})c_y + 2c_z]/2$
with $c_\gamma = \cos k_\gamma$. The first term in Eq. (5.14) describes the coherent motion
of holes within a band of width $W_{\text{hl}}^{\text{coh}} = 4t$. The second term describes the
interaction of holes with excitations of the orbital background. The dynamics
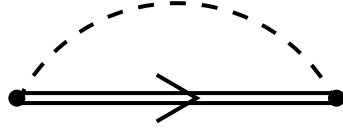
Figure 5.7: *Born approximation of the holon self energy: The double line denotes the "dressed" holon propagator with self-energy contributions, the dashed line represents the "orbital-wave" Green's function.*

of the latter is controlled by the inter-site coupling Hamiltonian (5.9) which in the momentum representation becomes

$$H_J = J \sum_{\boldsymbol{k}} \beta_{\boldsymbol{k}}^{\dagger} \beta_{\boldsymbol{k}}. \tag{5.15}$$

Hamiltonian (5.15) describes dispersionless, non-propagating orbital excitations of energy J. The local nature of orbital excitations follows from the absence of frustration effects in the inter-site orbital coupling term (5.9).

The interaction of holes with orbital degrees of freedom changes the character of the hole motion: Scattering on orbital excitations leads to a suppression of the coherent quasiparticle weight and a simultaneous widening of the holon band. In analogy to studies of spin systems [KAE89, MAZ91], we analyze these effects by employing a self-consistent Born approximation for the self energy of holes — within this method all non-crossing diagrams of the self energy are summed up to infinite order while crossing diagrams are neglected. Restricting ourselves to the case of a single hole moving at the bottom of the band, we obtain the following expression for the holon self energy (see Fig. 5.7):

$$\Sigma(i\omega) = t^2 \sum_{\boldsymbol{p}} \gamma_{\boldsymbol{p}}^2 \, G(i\omega - J, \boldsymbol{p}). \tag{5.16}$$

The Matsubara frequencies are defined as $i\omega = i(2n+1)\pi T$, where T denotes temperature and n an integer number.

Our first aim is to study the loss of coherency in the hole motion. This can be done by employing a dominant-pole approximation [KAE89]: We split the holon propagator in Eq. (5.16) into its coherent and incoherent parts,

$$G(i\omega, \boldsymbol{k}) = \frac{a_{\boldsymbol{k}}}{i\omega - \tilde{\omega}_{\boldsymbol{k}}} + G^{\mathrm{inc}}(i\omega, \boldsymbol{k}), \tag{5.17}$$

where $a_{\boldsymbol{k}}$ denotes the quasiparticle weight and $\tilde{\omega}_{\boldsymbol{k}}$ the not-yet-known renormalized holon dispersion. Keeping only the coherent part and using $a_{\boldsymbol{k}} =$

$[1 - (\partial/\partial\omega)\Sigma'(\omega)]^{-1}$ with $\Sigma'(\omega) = \mathrm{Re}[\Sigma(i\omega \to \omega + i0^+)]$, the following recursion relation for the quasiparticle weight is obtained:

$$a_{\bar{\boldsymbol{q}}} = \left[1 + t^2 \sum_{\boldsymbol{p}} \gamma_{\boldsymbol{p}}^2 \frac{a_{\boldsymbol{p}}}{(\tilde{\omega}_{\bar{\boldsymbol{q}}} - \tilde{\omega}_{\boldsymbol{p}} - J)^2}\right]^{-1}, \qquad (5.18)$$

with $\bar{\boldsymbol{q}} = (0, 0, \pi)$ at the bottom of the band. Equation (5.18) can be approximately solved by expanding the integrand around $\bar{\boldsymbol{q}}$, which yields

$$a_{\bar{\boldsymbol{q}}} = \begin{cases} 1 - \dfrac{1}{\sqrt{2\pi^2}} \left(\dfrac{t}{J}\right)^{1/2} & \text{for } J \gg t, \\[2mm] \sqrt[4]{2\pi^2} \left(\dfrac{J}{t}\right)^{1/4} & \text{for } J \ll t. \end{cases} \qquad (5.19)$$

In the limit $J/t \to \infty$, orbitals become static and coherent hole motion with $a_{\bar{\boldsymbol{q}}} = 1$ is recovered. In the opposite limit $J/t \to 0$, the holon quasiparticle weight is completely lost, indicating strong scattering of holes on orbital fluctuations.

Next we turn to study the renormalization of the holon bandwidth. Inserting $G(i\omega, \boldsymbol{k}) = [i\omega - \omega_{\boldsymbol{k}} - \Sigma(i\omega)]^{-1}$ into Eq. (5.16) leads to a recursion relation for the holon self energy:

$$\Sigma(i\omega) = t^2 \sum_{\boldsymbol{p}} \frac{\gamma_{\boldsymbol{p}}^2}{i\omega - \omega_{\boldsymbol{p}} - J - \alpha\Sigma(i\omega - J)}. \qquad (5.20)$$

The factor $\alpha = (z - 1)/z$ partially accounts for the constraint that forbids more than one orbital excitation per site — the hole may therefore not return to a previously visited site unless to reabsorb an excitation. We solve Eq. (5.20) numerically and determine the spectral function $\rho_{\bar{\boldsymbol{q}}}(\omega) = -\frac{1}{\pi}\mathrm{Im}[G(i\omega \to \omega + i0^+, \bar{\boldsymbol{q}})]$ at the bottom of the band. The result is shown in Fig. 5.8. Different values of J/t are used. In the limit $J/t \to 0$, the spectrum is completely incoherent and extends down to $\omega_{\mathrm{min}} = -3t$ corresponding to a holon bandwidth of $W_{\mathrm{hl}} = 2|\omega_{\mathrm{min}}| = 6t$.[1] In this limit the hole creates its own disorder and effectively moves within an orbital-liquid state characterized by strong orbital fluctuations. In the opposite case $J/t \to \infty$, all spectral weight accumulates in a quasiparticle peak (denoted by a vertical line) at $\omega_{\mathrm{QP}} = -2t$ which corresponds to a bandwidth of $W_{\mathrm{hl}} = 2|\omega_{\mathrm{QP}}| = 4t$. The orbital state is static here and excitations are completely suppressed. At finite values of J/t, the total spectral weight is divided into coherent and

---

[1]The factor $\alpha = (z - 1)/z$ in Eq. (5.20) compensates only partially for the mean-field treatment of the constraint that forbids more than one orbital excitation per site. The bandwidth numerically obtained for $J/t \to 0$ is therefore slightly larger than $W_{\mathrm{hl}} = 6t$.
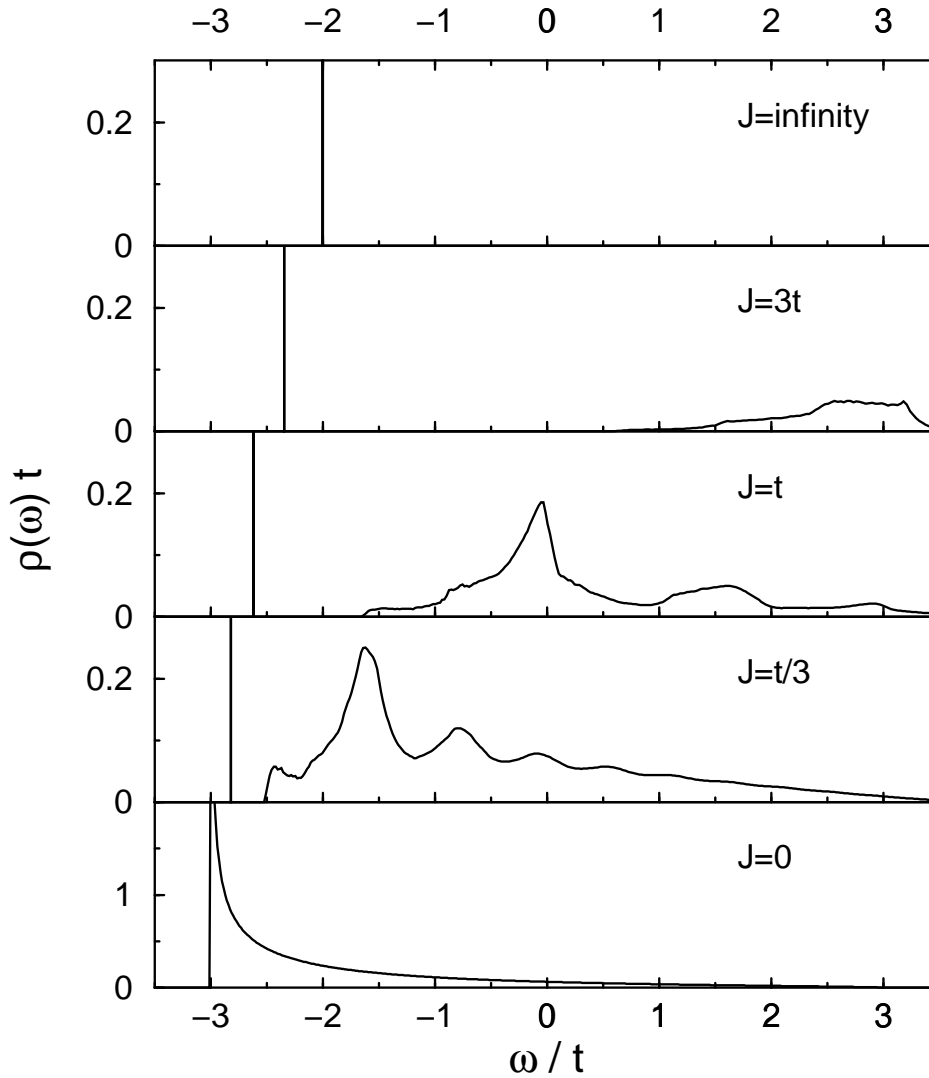
Figure 5.8: *Spectral function of a hole moving at the bottom of the band. Different values of J/t are used: The spectrum is completely incoherent for J = 0, having a lower bound at $\omega_{min} = -3t$. With increasing values of J/t, spectral weight is shifted from the incoherent part of the spectrum to a coherent quasiparticle peak (denoted by a vertical line). In the limit $J/t \to \infty$, the quasiparticle peak is at $\omega_{QP} = -2t$ and has accumulated all spectral weight.*

incoherent parts. The latter is separated from the quasiparticle peak by the orbital excitation energy J. Processes in which the hole creates more than one orbital excitation are reflected by a succession of peaks in the incoherent spectrum. For $J = t/3$ which is realistic to manganites, the quasiparticle peak accounts for $\approx 65\%$ of the spectral weight and the width of the holon band is

$$W_{\mathrm{hl}} \approx 5.7t. \tag{5.21}$$

Comparing the above number with our previous result $W_{\mathrm{hl}} = 6t$ for the orbital-liquid state, we find a reduction of about 5%. We therefore conclude that a disorder-order crossover in the orbital sector has only a secondary effect on the kinetic energy of charge carriers, ruling it out as a possible driving mechanism to initiate the metal-insulator transition in manganites.

5.3   Orbital Polarons

In the preceeding section we have considered charge carriers to interact with the orbital sector via the transfer part of Hamiltonian (5.2). While this coupling was shown to be responsible for a shift of spectral weight from the coherent to the incoherent part of the holon spectrum, the effect onto the full bandwidth was found to be only small. In the following we point out that in an orbitally degenerate Mott-Hubbard system there also exists a direct coupling between holes and orbitals stemming from a polarization of e_g orbitals in the neighborhood of a hole. This coupling is strong enough for holes to form a bound state with the surrounding orbitals at low doping concentrations. Based upon this picture we show that a strong reduction of the bandwidth comes into effect as orbital-hole bound states begin to form.

5.3.1   Polarization of Orbitals

The cubic symmetry of perovskite manganites is locally broken in the vicinity of holes which results in a lifting of the e_g degeneracy on sites adjacent to a hole (see Fig. 5.9). Here we discuss two mechanisms that are foremost responsible for this level splitting: (1) a displacement of oxygen ions that move towards the empty site; and (2) the Stark splitting of e_g states which is induced by the Coulomb force between "positive" hole and negative electrons. The magnitude of the degeneracy lifting $\Delta = \Delta^{\mathrm{ph}} + \Delta^{\mathrm{ch}}$ is estimated as follows: The former phonon contribution Δ^{ph} originates in the coupling of holes to the lattice breathing mode Q_1 and of e_g electrons to two Jahn-Teller
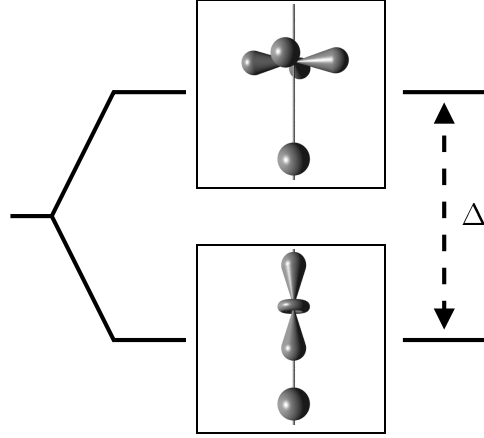
Figure 5.9: *Polarization of e_g levels on sites next to a hole: Phonons and Coulomb interaction induce a splitting of energy $\Delta = \Delta^{ph} + \Delta^{ch}$.*

modes Q_2 and Q_3 (see Chap. 1):

$$H_{\text{el-ph}} = -\sum_i \left(g_1 Q_{1i} n_i^h + g_2 Q_{2i} \sigma_i^x + g_3 Q_{3i} \sigma_i^z + \frac{K}{2} \boldsymbol{Q}_i^2 \right), \qquad (5.22)$$

where n_i^h denotes the number operator for holes and the Pauli matrices $\sigma_i^{x/z}$ act on the orbital subspace. The coupling constants are g_1 and $g_2 \approx g_3$ and K is the lattice spring constant. Hamiltonian (5.22) mediates an interaction between empty and occupied sites. The effective Hamiltonian describing this coupling is obtained by integrating Eq. (5.22) over oxygen displacements $\boldsymbol{Q}_i = (Q_{1i}, Q_{2i}, Q_{3i})$. For a given bond along the z direction this yields $H^z = -\frac{1}{2}\Delta^{\text{ph}} n_i^h \sigma_j^z$ with

$$\Delta^{\text{ph}} = g_1 g_2 \sqrt{2}/(3K) \approx (g_1/g_2) E_{\text{JT}}. \qquad (5.23)$$

A lower bound for this quantity is given by the Jahn-Teller energy, i.e., $\Delta^{\text{ph}} \geq E_{\text{JT}} \approx 0.2$ eV [DES98], assuming that coupling to the breathing mode is at least as strong as coupling to the Jahn-Teller modes. Next we estimate the contribution to the e_g-level splitting that follows from the Coulomb interaction between a positively charged hole and an e_g electron on a neighboring site. The magnitude Δ^{ch} of this splitting is assessed by taking into account the covalence of Mn $3d$ and O $2p$ orbitals, which gives

$$\Delta^{\text{ch}} \approx \frac{3}{4}\gamma^2 R_{\text{Mn-Mn}}^{-1}. \qquad (5.24)$$

The covalency factor $\gamma = t_{pd}/\Delta_{pd}$ can be obtained from the transfer amplitude and the charge gap between Mn and O sites, $t_{pd} \approx 1.8$ eV and
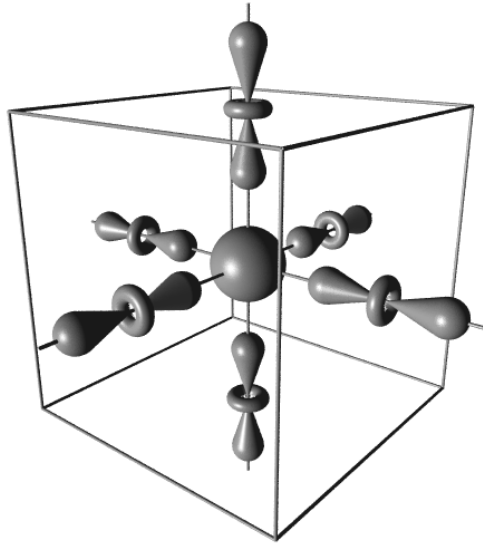
Figure 5.10: *Orbital polaron in the strong-coupling limit: Six e_g states point towards a central hole.*

$\Delta_{pd} \approx 4.5$ eV [SAI95]. Together with a lattice spacing of $R_{\text{Mn}-\text{Mn}} = 3.9$ Å this leads to $\Delta^{\text{ch}} \approx 0.4$ eV. In total the polarization of e_g levels on sites next to a hole yields an energy splitting $\Delta \approx 0.6$ eV. Being comparable in magnitude to the transfer amplitude t this number strongly indicates a direct coupling of charge and orbital degrees of freedom to be of importance in manganites.

The splitting of e_g levels effects all six sites surrounding a hole. From the above Hamiltonian for a bond along the z axis, analogous expressions for x and y directions are derived by a rotation in orbital isospin space (see Chap. 1). The complete Hamiltonian for the cubic system is then

$$H_{\text{ch-orb}} = -\Delta \sum_{\langle ij \rangle_\gamma} n_i^h \tau_j^\gamma, \qquad (5.25)$$

with orbital pseudospin operators given by Eq. (5.3). Hamiltonian (5.25) promotes the formation of orbital polarons. For low enough hole concentrations these consist of a bound state between a central hole and the surrounding e_g orbitals pointing towards the hole as is shown in Fig. 5.10. This configuration also yields a large amplitude of virtual excursions of e_g electrons onto the empty site. Thus, besides minimizing the interaction energy of Hamiltonian (5.25), it also allows to lower the kinetic energy. We note that these virtual hopping processes locally enhance the magnetic moments of core and e_g spins via the double-exchange mechanism, providing a large effective spin of the
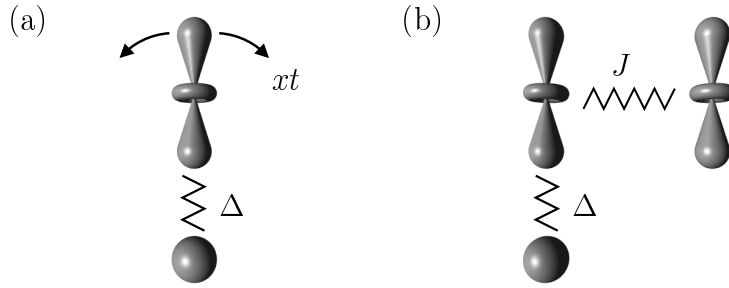
Figure 5.11: *(a) Orbital fluctuations with an energy scale $\propto xt$ and (b) inter-site correlations $\propto J$ compete against the orbital-hole binding energy Δ.*

orbital polaron. This naturally explains the development of ferromagnetic clusters experimentally observed at temperatures above T_C [TER97].

5.3.2 Binding Energy

In conventional lattice-polaron theory, the binding energy is a function of the coupling constant g and the stiffness of the lattice which is controlled by the spring constant K: The energy gain stemming from the interaction between charge carriers and the lattice competes against the deformation energy of the crystal. In the case of orbital polarons, the underlying picture is very similar. Here the coupling constant is given by the orbital-charge interaction energy Δ, while the energy scale $W_{\mathrm{orb}} = 6xt + J$ is a measure of the "stiffness" of the orbital sector. These two quantities are expected to determine the binding energy of the orbital polaron:

$$E_b^{\mathrm{orb}} = f(\Delta, W_{\mathrm{orb}}). \tag{5.26}$$

The role of W_b^{orb} can be illustrated as follows (see Fig. 5.11): In an orbital-liquid state, orbitals have to give up part of their fluctuation energy in order to form a bound state with a hole. As a consequence, polarons are stable only if orbital fluctuations are weak. Furthermore, polarons have a frustrating effect on inter-site orbital correlations. The local orientation of orbitals favored by Hamiltonian (5.25) does in general not comply with the orientation that would minimize the Jahn-Teller and superexchange coupling between orbitals on nearest- and next-nearest-neighbor sites of the hole. Thus, in order to form a bound state orbitals have to give up part of their inter-site correlation energy J as well. The fact that the polaron binding energy is controlled by the orbital energy scale $W_{\mathrm{orb}} = 6xt + J$ has direct implications for the phase diagram of manganites: Due to the doping dependence of W_{orb}, orbital polarons

are stable only at low hole concentrations where fluctuations are weak. The tendency of the system to form polarons is therefore most pronounced in the lower part of the phase diagram.

To derive an expression for the polaron binding energy, the following approach is used: First we consider a static hole placed in an ordered state without fluctuations. We then calculate the reduction of the total energy due to the interaction Hamiltonian (5.25). All approximations made in the following aim at discarding terms reminiscent of a specific type of orbital order, while preserving the most general structure of the orbital-hole binding energy. We focus on a single site located next to the hole in the z direction. The orbital configuration at this site is determined by the coupling to the hole described by Eq. (5.25) as well as by the orientation of neighboring orbitals which couple via superexchange and Jahn-Teller effect; the latter interaction is determined by Hamiltonian (5.9). Treating all orbitals except the one explicitly considered here on a mean-field level, the following Hamiltonian is obtained for the selected site:

$$H_\delta^z = - \left(\Delta \tau_\delta^z + J \tau_\delta^\Theta \right). \tag{5.27}$$

Here $\tau_i^\Theta = (\sin\Theta \sigma_i^x + \cos\Theta \sigma_i^z)/2$ fixes the orbital orientation which would minimize the interaction energy with the orbital background — for the type of order used in Eq. (5.10), e.g., $\Theta = \pm\pi/2$. In general, this orientation does not coincide with the $|3z^2 - r^2\rangle$ configuration favored by the orbital polaron which is described by the first term in brackets. The state actually chosen by the system then depends on the ratio of Δ and J as well as on the angle Θ. We determine the energy of this state and, since we are not interested in any specific type of order, average over the angle Θ. Finally subtracting the $\Delta \to 0$ limit and multiplying with the number of bonds connecting the hole to its surrounding, the following expression for the polaron binding energy is obtained:

$$E_b^{\mathrm{orb}} = 3 \left[\sqrt{\Delta^2 + J^2} - J \right]. \tag{5.28}$$

In the limit $J/\Delta \to \infty$, the orbital state is very stiff and cannot be polarized by the hole; the binding energy then vanishes as $3\Delta^2/(2J)$. On the other hand, the polarization is complete in the limit $J/\Delta \to 0$, yielding a maximum value $E_b^{\mathrm{orb}} = 3\Delta$ for the binding energy. A plot of E_b^{orb} is shown in Fig. 5.12 (upper curve). We note that the functional form of Eq. (5.28) differs from the conventional lattice-polaron case where $E_b^{\mathrm{ph}} = g^2/(2K)$. This is due to the fact that there exists an upper limit of the orbital polarization in which the orbitals around a hole have been fully reoriented to point towards the empty site (see Fig. 5.10); technically the existence of this upper bound is reflected by the hard-core nature of the Pauli operators in Eq. (5.27). The familiar
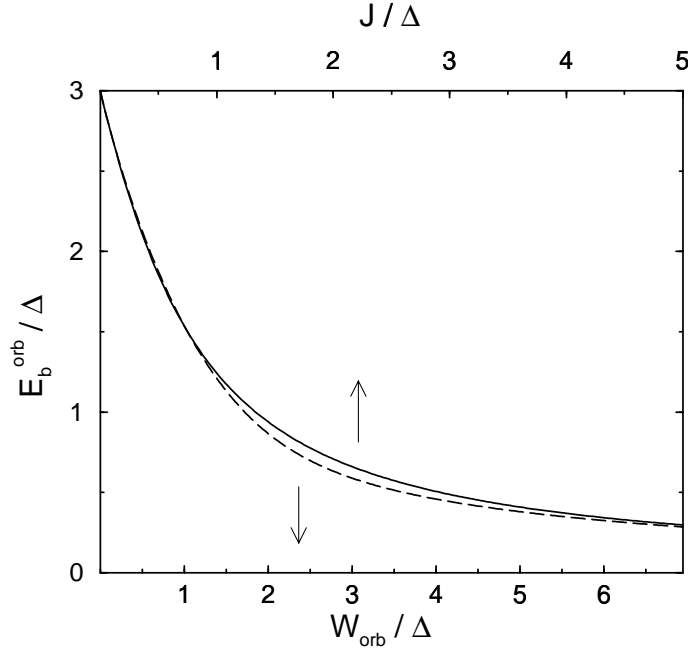
Figure 5.12: *Polaron binding energy E_b^{orb}: The solid curve is a plot of Eq. (5.28) for the orbitally ordered state as a function of J (upper axis), the dashed curve corresponds to Eq. (5.34) for the orbital-liquid state and is plotted as a function of W_{orb} (lower axis).*

form of the binding energy $\propto \Delta^2/J$ is recovered only for the weak-coupling limit in which orbital distortions around the hole are small.

Next we consider a static hole placed in a strongly fluctuating orbital-liquid state. Hamiltonian (5.25) imposes a splitting of e_g levels on the sites next to the hole. The orbiton quasiparticles of Sec. 5.2 scatter on these local potentials, which may lead to the formation of an orbiton-hole bound state. To calculate the polaron stabilization energy we again consider a single site next to the hole in the z direction. The local potential imposed by the close-by hole is of the form

$$H_\delta^z = -\Delta \tau_\delta^z, \tag{5.29}$$

where $\tau_i^z = \frac{1}{2}\sigma_i^z$. We calculate the effect of successive scattering of orbitons on the above potential employing a T-matrix formalism; interference between different scattering centers is neglected here. The correction to the orbiton Green's function that seizes the effect of Hamiltonian (5.29) is given by

$$\delta G_{\mathrm{orb}}(i\omega; \boldsymbol{R}, \boldsymbol{R}) = G_{\mathrm{orb}}^0(i\omega; \boldsymbol{R}, \delta)T_\delta(i\omega)G_{\mathrm{orb}}^0(i\omega; \delta, \boldsymbol{R}), \tag{5.30}$$

with the scattering matrix

$$T_\delta(i\omega) = -\frac{\sigma^z \Delta/2}{1 - \sigma^z \Delta G^0_{\text{orb}}(i\omega)/2}.$$

Here $G^0_{\text{orb}}(i\omega; \boldsymbol{R}, \boldsymbol{R}')$ denotes the orbiton propagator of the system in the absence of the scattering potential. The elements of this 2×2 matrix are given by $[G^0_{\text{orb}}(i\omega; \boldsymbol{R}, \boldsymbol{R}')]^{\alpha\beta} = -\langle T_\tau f_{\boldsymbol{R}\alpha} f^\dagger_{\boldsymbol{R}'\beta} \rangle^0_{i\omega}$ and are controlled by the mean-field Hamiltonian (5.5). The on-site Green's function is $G^0_{\text{orb}}(i\omega) = \frac{1}{2}\text{Tr}[G^0_{\text{orb}}(i\omega; \delta, \delta)]$. Integrating over lattice sites, Eq. (5.30) becomes

$$
\begin{aligned}
\delta G(i\omega) &= -\frac{\Delta}{4} \left[\frac{\partial}{\partial i\omega} G^0(i\omega) \right] \\
&\quad \times \left(\frac{1}{1 - \Delta G^0(i\omega)/2} - \frac{1}{1 + \Delta G^0(i\omega)/2} \right),
\end{aligned}
\tag{5.31}
$$

with $\delta G_{\text{orb}}(i\omega) = \frac{1}{2}\sum_{\boldsymbol{R}} \text{Tr}[\delta G_{\text{orb}}(i\omega; \boldsymbol{R}, \boldsymbol{R})]$. The change in the total energy of the system which is induced by the scattering potential can now be obtained from Eq. (5.31) by employing

$$\delta E = 2 \int_{-\infty}^{\mu} dw \, (\omega - \mu) \, \delta\rho(\omega), \tag{5.32}$$

where $\delta\rho(\omega) = -(1/\pi)\text{Im}[\delta G(i\omega \to \omega + i0^+)]$ denotes the scattering contribution to the density of states. The orbiton chemical potential is set to $\mu = 0$ in the following. We evaluate Eq. (5.32) by approximating the on-site Green's function by

$$G^0(i\omega) \approx -\frac{1}{W_{\text{orb}}} \ln \left[\frac{i\omega - W_{\text{orb}}/2}{i\omega + W_{\text{orb}}/2} \right]. \tag{5.33}$$

This expression yields a constant density of states for the translationally invariant system which resembles the result that can be obtained numerically from the mean-field Hamiltonian (5.5). Approximately solving the integral in Eq. (5.32) and multiplying the result with the number of nearest neighbors of the hole, we finally arrive at the following expression for the polaron binding energy:

$$E_b^{\text{orb}} = 3\Delta \left[y \, (\text{cth}\, y - 1) + \frac{y \ln 2}{y^2 + (\pi/2)^2} \right], \tag{5.34}$$

with $y = W_{\text{orb}}/\Delta$. Equation (5.34) describes the polaron stabilization energy in a strongly fluctuating orbital-liquid state. A plot of this function is shown in Fig. 5.12 (lower curve). The binding energy reaches its maximum $E_b^{\text{orb}} =$

3Δ if orbital fluctuations are weak, while it vanishes as $3\ln 2(\Delta^2/W_{\text{orb}})$ in the opposite limit where fluctuations are strong.

In the last two paragraphs we have calculated the polaron binding energy in an orbitally ordered as well as in an orbital-liquid state. Although very different approaches were used to describe these complementary cases, the expressions obtained closely coincide: As can be seen in Fig. 5.12, the two functions are almost indistinguishable if one identifies J in Eq. (5.28) with νW_{orb} in Eq. (5.34), where $\nu \approx 0.72$ is a numerical fitting factor. Motivated by the observation that $W_{\text{orb}} = 6xt + J$ reduces to J in the limit of strong orbital correlations $J \gg xt$, we discard the fitting factor in the following by setting $\nu = 1$. We believe these two cases to be smoothly connected as should come out in a more elaborate treatment of the problem. Based upon these considerations, we conclude that Eq. (5.28) can be used to model the polaron binding energy of both the fluctuating and the static orbital state:

$$E_b^{\text{orb}} = 3(1-x)\left[\sqrt{\Delta^2 + W_{\text{orb}}^2} - W_{\text{orb}}\right], \qquad (5.35)$$

where $W_{\text{orb}} = 6xt + J$ in former and $W_{\text{orb}} = J$ in the latter case. We finally note that in deriving expressions (5.28) and (5.34) for the binding energy, all six sites surrounding the static hole were assumed to be occupied. Since at finite doping the probability of a site being occupied is only $(1-x)$, we renormalize Eq. (5.35) by this average occupation factor.

To summarize, E_b^{orb} in Eq. (5.35) represents the energy to be gained by polarizing the orbital background around a static hole. This number depends on the orbital energy scale $W_{\text{orb}} = 6xt + J$, i.e., on orbital fluctuations and inter-site orbital correlations which both tend to suppress the polaron binding energy. W_{orb} is to be considered as the counterpart of the lattice stiffness K in conventional polaron theory. The important difference is that W_{orb} explicitly depends on x which has important consequences for the phase diagram of manganites: Orbital polarons can form only at low doping concentrations where orbital fluctuations are weak and the binding energy is consequently large.

5.3.3   Polaron Bandwidth

The orbitally degenerate Mott-Hubbard system is instable towards the formation of orbital-hole bound states at low doping concentrations. In this small-polaron regime, holes are pinned by the binding potential and can move only if being thermally activated. At low temperatures these processes can be neglected; coherent charge motion is then possible solely due to quantum tunneling. Since the polaron is a composite object consisting of a hole

and several orbitals, the amplitude of these tunneling processes is expected to be small as is indeed shown in this section.

Here we restrict ourselves to polarons moving in an orbitally ordered state. Our analysis is based upon the following idea: By allowing a hole to polarize the surrounding orbitals, the system reduces its ground state energy by E_b^{orb}. This energy is mostly lost if the hole hops to another site since the orbital sector cannot immediately adopt to the new position — orbital fluctuations are slow compared to those of holes. After a short time the system returns to the ground state, most likely by transferring the hole back to its original location. But there is also a small probability for the hole to keep its new position while the orbital sector adapts to the relocation. This is possible due to the non-orthogonality of configurations in which orbitals point towards the old and the new location of the hole, respectively (see Fig. 5.13). The polaron tunneling amplitude is then given by the transfer amplitude t of holes multiplied by the overlap between states with orbitals pointing towards the old and new position of the hole, respectively. This overlap is calculated as follows: We use Hamiltonian (5.27) to determine the orientation of a single orbital next to the hole — all other orbitals are treated on a mean-field level. As the hole hops, this orbital has to change its orientation from pointing towards the hole to being aligned with the background. The projection between these two states is

$$p = \frac{1}{\sqrt{2}} \left[1 + \frac{J}{\sqrt{\Delta^2 + J^2}} \right]^{1/2}. \tag{5.36}$$

An average over the angle Θ specifying the type of orbital order in Eq. (5.27) has been performed here. Other orbitals undergo the reversed process: Originally being aligned with the background, they turn towards the hole as the latter hops onto a neighboring site. In total there are $2(z - 1) \approx 2z$ orbitals that have to reorient. The overlap between the initial and the final state is then given by $P = p^{2z}$, yielding

$$P = \frac{1}{2^z} \left[1 + \frac{J}{\sqrt{\Delta^2 + J^2}} \right]^z. \tag{5.37}$$

We rewrite Eq. (5.37) as

$$\begin{aligned} P &= \left[1 - \frac{\sqrt{\Delta^2 + J^2} - J}{2\sqrt{\Delta^2 + J^2}} \right]^z \\ &\approx \exp\left[-3\frac{\sqrt{\Delta^2 + J^2} - J}{\sqrt{\Delta^2 + J^2}} \right], \end{aligned} \tag{5.38}$$
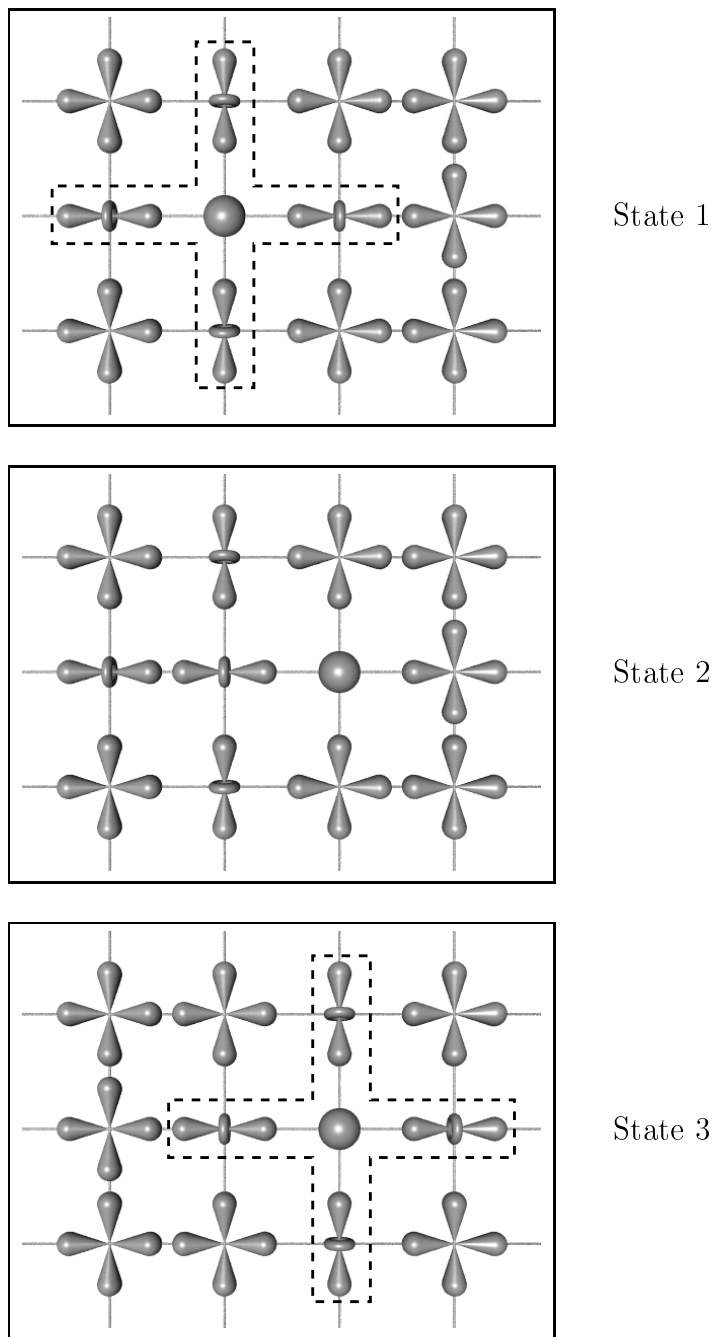
Figure 5.13: *Orbital polarons can move by tunneling. In state 1 the hole forms a polaron with the surrounding orbitals encircled by a dashed line. When the hole hops one site to the right configuration 2 is reached — this state is not favored since orbitals no longer point towards the hole. However, there is a small but finite overlap with state 3 in which hole and orbitals again form a polaron. In this example a ferro-type alignment of $|x^2 - y^2\rangle$ orbitals is assumed in the background.*

Figure 5.14: *Ratio of polaron and holon bandwidth $e^{-\eta}$. The solid line is based on the exponential form in Eq. (5.39), the dashed line represents Eq. (5.37). The polaron bandwidth shrinks which decreasing values of J/Δ associated with an enhanced orbital polarizability.*
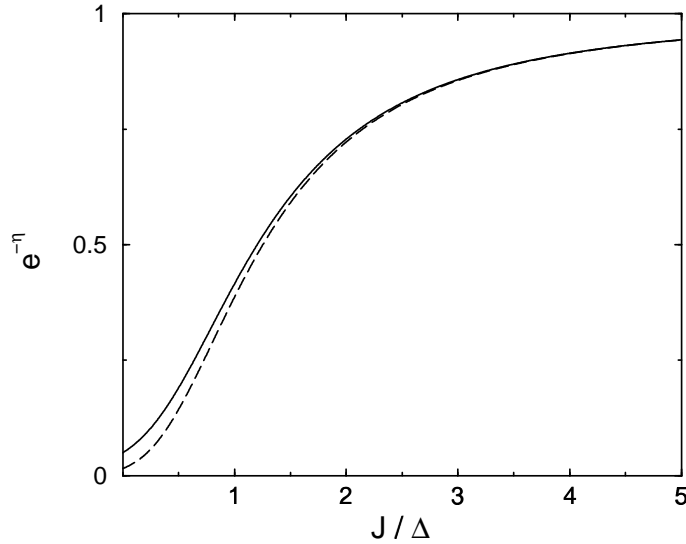
where the exponential form becomes exact for large coordination number which has been set to $z = 6$. The denominator in the exponent is identified as the orbital binding energy given by Eq. (5.28). Hence we finally arrive at the following compact expression for $P \equiv e^{-\eta}$:

$$e^{-\eta} = \exp\left[-\frac{E_b^{\mathrm{orb}}}{\sqrt{\Delta^2 + J^2}}\right]. \tag{5.39}$$

A plot of this function is shown in Fig. 5.14. The physical significance of $e^{-\eta}$ is that it relates the holon to the polaron bandwidth:

$$W_{\mathrm{pol}} = W_{\mathrm{hl}}\, e^{-\eta}. \tag{5.40}$$

As the system becomes critical towards the formation of orbital-hole bound states, polarons replace holes as charge carriers. Our result shows that this transition is accompanied by an exponential suppression of the bandwidth. Strictly speaking the translationally invariant system remains a metal; in reality, however, the small bandwidth makes polarons susceptible to localization, e.g., by trapping in the random potential of impurities. The suppression of the bandwidth is most pronounced if the polaron binding energy is large: The orbitals around the hole are then strongly distorted, which necessitates a

significant reorientation to allow the hole to hop. We note that the expression in Eq. (5.39) is similar to the result obtained in conventional lattice-polaron theory where $e^{-\eta} = \exp\left(-E_b^{\mathrm{ph}}/\omega_0\right)$. Here $E_b^{\mathrm{ph}} = g^2/(2K)$ denotes the polaron binding energy and ω_0 the phonon frequency; the latter corresponds to $(\Delta^2 + J^2)^{1/2}$ in our orbital-polaron theory.

Equation (5.39) has been derived for a static, non-fluctuating orbital state. Following the discussion in deriving the polaron binding energy, we generalize the result to account for orbital fluctuations as well. This is done by replacing the inter-site correlation energy J by the more general orbital energy scale $W_{\mathrm{orb}} = 6xt + J$. Hence we obtain

$$e^{-\eta} = \exp\left[-\frac{E_b^{\mathrm{orb}}}{\sqrt{\Delta^2 + W_{\mathrm{orb}}^2}}\right], \tag{5.41}$$

where the polaron binding energy E_b^{orb} is now given by Eq. (5.35).

To summarize, the development of orbital polarons leads to a sharp reduction of the bandwidth. In this regime the orbital-hole bound state can move only as an entity via quantum-tunneling processes. Since the polaron extends over several lattice sites, the transfer amplitude is exponentially small. The bandwidth reduction is controlled by the ratio $E_b^{\mathrm{orb}}/[\Delta^2 + W_{\mathrm{orb}}^2]^{1/2}$ which is a measure of the orbital distortions around a hole. Strong orbital fluctuations and inter-site orbital correlations weaken the polaron effect by suppressing these distortions.

5.4 Metal-Insulator Transition

As was shown in the preceeding section, the formation of orbital-hole bound states leads to an exponential suppression of the bandwidth which makes the system prone to localization. In a double-exchange system, this crossover from a free-carrier to a small-polaron picture can be initiated either by a reduction of the doping concentration or by an increase in temperature; the former acts via an enhancement of the polaron binding energy, the latter by constricting the motion of holes via the double-exchange mechanism. In this section we combine our orbital-polaron picture with the theory of conventional lattice polarons to develop a scheme of the metal-insulator transition in manganites.

The transition from a free-carrier to a small-polaron picture is governed by the dimensionless coupling constant $\lambda_{\mathrm{orb}} = E_b^{\mathrm{orb}}/D_{\mathrm{hl}}$, where E_b^{orb} is the polaron binding energy given by Eq. (5.35) and $D_{\mathrm{hl}} = W_{\mathrm{hl}}/2 = 3t$ is the half-bandwidth of holes. The lattice breathing mode of Eq. (5.22) adds an

additional contribution $\lambda_{\mathrm{ph}} = E_b^{\mathrm{ph}}/D_{\mathrm{hl}}$ with $E_b^{\mathrm{ph}} = g_1^2/(2K)$, which further promotes the formation of polarons. The coupling constant thus becomes

$$\lambda = \frac{E_b^{\mathrm{orb}} + E_b^{\mathrm{ph}}}{D_{\mathrm{hl}}}. \tag{5.42}$$

The critical value that separates free-carrier and small-polaron regimes is $\lambda = 1$. For $\lambda \gg 1$ small polarons have fully developed and the bandwidth is reduced by an exponential factor

$$e^{-\eta} = \exp\left[-\gamma\left(\frac{E_b^{\mathrm{orb}}}{\sqrt{\Delta^2 + W_{\mathrm{orb}}^2}} + \frac{E_b^{\mathrm{ph}}}{\omega_0}\right)\right], \tag{5.43}$$

with $\gamma = 1$. We note that interference effects between orbital and lattice coupling are neglected in Eq. (5.43). For $\lambda < 1$ the free-carrier picture is recovered and holes move in a band of width $W_{\mathrm{hl}} = 6t$. This implies $\gamma = 0$ in Eq. (5.43), yielding $e^{-\eta} = 1$. To simulate the crossover between the two regimes, we phenomenologically employ the function

$$\gamma = \begin{cases} \beta - \dfrac{\ln[\lambda(1+\beta)]}{\lambda^2} & \text{for} \quad \lambda > 1, \\[2ex] 0 & \text{for} \quad \lambda < 1, \end{cases} \tag{5.44}$$

with $\beta = [1 - 1/\lambda^2]^{1/2}$. This function has been proposed for strongly coupled electron-phonon systems (see, e.g., Ref. [ALE94]) and avoids an unphysical sudden drop of the bandwidth as $\lambda = 1$ is reached. The crossover hence obtained for $e^{-\eta}$ is depicted in Fig. 5.15.

Up to this point we have mainly focused on the role of the orbital energy scale W_{orb} in the formation of small polarons. We now turn to analyze in more detail the effect of temperature. The latter controls the bandwidth W_{hl} via the double-exchange mechanism: At low temperatures all spins are ferromagnetically aligned and the transfer amplitude reaches its maximum. With increasing temperature the ferromagnetic moment weakens, constricting the motion of charge carriers. Specifically, the transfer amplitude changes with the normalized magnetization m as

$$t = t_0\sqrt{(1 + m^2)/2}. \tag{5.45}$$

The magnetization depends on temperature via the self-consistent equation

$$m = B_S(\alpha m) \quad \text{with} \quad \alpha = \frac{3S}{1+S}\frac{T_C}{T}, \tag{5.46}$$
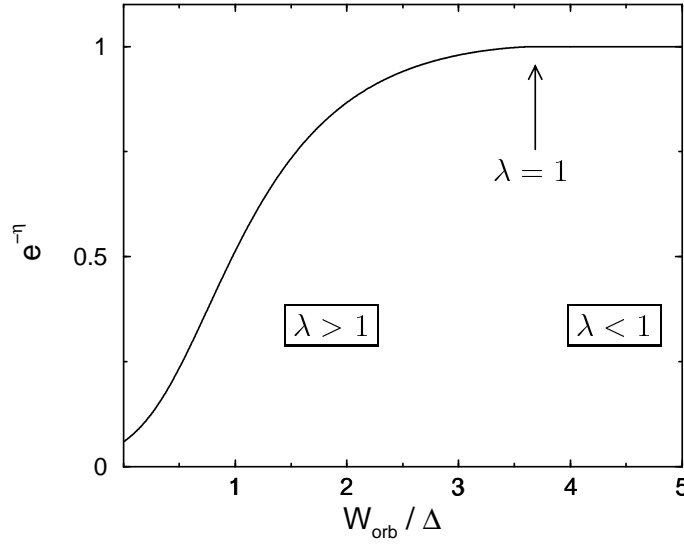
Figure 5.15: *Crossover from the free-carrier to the small-polarons regime. At $\lambda < 1$ polarons are unstable and the bare holon bandwidth is recovered. At $\lambda > 1$ orbital polarons form, leading to an exponential suppression of the bandwidth. To avoid an abrupt drop of the bandwidth at $\lambda = 1$, Eq. (5.44) is used to connect the two regimes. Phonon contributions are neglected here by setting $E_b^{ph} = 0$.*

where

$$B_S(y) = \frac{2S+1}{2S} \operatorname{cth}\left[\frac{2S+1}{2S}\, y\right] - \frac{1}{2S} \operatorname{cth}\left[\frac{1}{2S}\, y\right]$$

denotes the Brillouin function. The average magnetic moment per site varies with doping: The moments $S^c = 3/2$ and $s = 1/2$ of core and e_g spins combine on average as

$$S = \frac{3}{2} + \frac{1}{2}(1 - x). \tag{5.47}$$

Finally, the Curie temperature T_C in Eq. (5.46) is controlled by the strength J_{eff} of ferromagnetic exchange bonds via

$$T_C = \frac{\nu z}{3} S(S + 1) J_{\text{eff}}. \tag{5.48}$$

The fitting parameter ν compensates for an overestimation of T_C in the mean-field treatment. Double-exchange as well as superexchange processes are responsible for establishing the ferromagnetic links between sites. The magnitude of this coupling in the limit of large Hund's coupling is (see Chaps. 1 and 4)

$$J_{\text{eff}} = \frac{1}{2S^2}\left[x(1 - x)\chi t e^{-\eta} + (1 - x)^2 \frac{2\chi^2 t_0^2}{U_1}\right]. \tag{5.49}$$

The first term in squared brackets of Eq. (5.49) stems from the coherent motion of holes/polarons and represents the conventional double-exchange contribution to T_C. The factor $e^{-\eta}$ accounts for the rescaling of the coherent bandwidth as the small-polaron regime is entered. The second term is due to superexchange processes. It describes the high-energy virtual hopping of e_g electrons which is insensitive to a polaronic reduction of the bandwidth. It is also noticed that superexchange in an orbitally degenerate system is of ferromagnetic nature because of the large Hund's coupling present in manganites [MAE98a, END99, KHA99b]. Superexchange hence dominates the ferromagnetic interaction in the small-polaron regime.

The system of equations presented above controls the electronic and magnetic behavior of manganites at low and intermediate doping levels. A critical coupling $\lambda = 1$ leading to the formation of polarons can be reached either by lowering the doping concentration or by increasing the temperature — the former enhances E_b^{orb}, the latter quenches W_{hl}. The equations are interrelated and have to be solved recursively. As a result of this self consistency, the breakdown of the metallic bandwidth at $\lambda = 1$ is expected to be rather sharp: With the evolution of small polarons, the coherent band width shrinks, thereby weakening the magnetic exchange links. Double exchange then drives the system even farther towards the strong-coupling limit.

5.5   Comparison with Experiment

To illustrate the interplay between the system of equations presented in the preceeding section, we numerically extract from them the T-x phase diagram. While it is obvious that $T = T_C$ is a suitable criterion to separate the low-temperature ferromagnetic from the high-temperature paramagnetic state, more care has to be taken to distinguish between metallic and insulating behavior. Our theory describes the reduction of the bandwidth which follows from the formation of small polarons. However, strictly speaking, the system remains metallic even in the strong-coupling limit since polarons can still move by tunneling. It is therefore necessary to define a critical value of the bandwidth beyond which additional effects such as pinning to impurities are implicitly assumed to set in and finally turn the system into an insulator. The specific criterion used here is only of marginal importance, as feedback effects discussed above induce a quick collapse of the bandwidth once a critical coupling $\lambda = 1$ is reached. For simplicity we define $\lambda < 1$ to be a metal and $\lambda > 1$ to be an insulator.

The following parameters are chosen for calculating the phase diagram: The orbital polarization energy is set to $\Delta = 0.55$ eV, yielding a binding
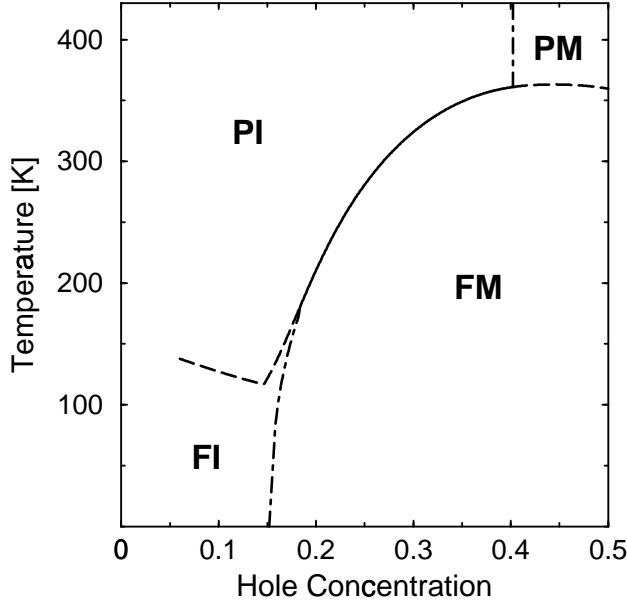
Figure 5.16: *Magnetic and electronic phase diagram obtained within the present theory. Dashed and dot-dashed lines represent magnetic and electronic transitions, respectively, the simultaneous transition in both channels is denoted by a solid line. The phases are: paramagnetic insulator (PI), paramagnetic metal (PM), ferromagnetic metal (FM), and ferromagnetic insulator (FI).*

energy comparable to the phononic one $E_b^{\mathrm{ph}} = 0.45$ eV; the phonon frequency is $\omega_0 = 0.05$ eV, the interaction between orbitals $J = 0.13$ eV, the bare transfer amplitude $t_0 = 0.36$ eV, and $U_1 = 4.0$ eV. The fitting parameter $\nu = 0.55$ is adjusted [2] to reproduce the values of T_C observed for $\mathrm{La}_{1-x}\mathrm{Sr}_x\mathrm{MnO}_3$ [URU95]. The result is shown in Fig. 5.16. For comparison the experimental phase diagram of $\mathrm{La}_{1-x}\mathrm{Sr}_x\mathrm{MnO}_3$ is shown in Fig. 5.17.

Our most important observation is that the doping dependence of orbital polarons makes the system more insulating at low and more metallic at high doping levels. Convincingly this is seen in the complete absence of metalicity at $x < 0.15$ and the appearance of a metallic phase above T_C at $x > 0.4$. The region $0.15 < x < 0.4$ in which colossal magnetoresistance is experimentally observed is characterized by a simultaneous magnetic and electronic transition from a ferromagnetic metal to a paramagnetic insulator [SCH95]. The role of polarons in this transition is most pronounced at low hole concentrations. This can be seen from the behavior of the magnetiza-

---

[2]This factor is partly attributed to the fluctuation correction $\nu = 0.7$ to the mean-field value of T_C which follows from Eq. (5.4) in Ref. [RUS74].
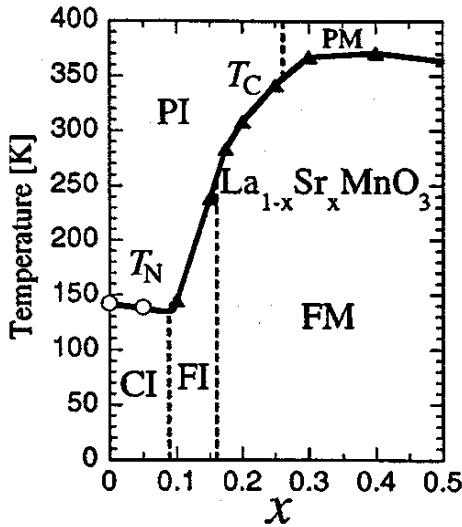
Figure 5.17: *Experimental phase diagram of $La_{1-x}Sr_xMnO_3$. From [IMA98].*

tion as T_C is approached from below (see Fig. 5.18): At low x, the polaron binding energy is large and the system is close to localization. A small reduction of the bandwidth via double exchange is then sufficient to trigger the formation of polarons, resulting in a sudden collapse of the magnetic moment. Such a sharp drop signals the presence of a localization mechanism beyond double exchange and is indeed seen experimentally (see, e.g., Refs. [SCH95, ZHO96, FRA99, CHE99]). On the other hand, at larger hole concentrations the polaron binding energy is comparably small. Thus, a significant suppression of the bandwidth via double exchange is needed before polaron formation can set in. The magnetization curve now closely resembles the one predicted by double-exchange theory.

Clearly beyond the grasp of conventional double-exchange theory lies the emergence of ferromagnetism in the insulating phase at low doping. Mostly responsible for this are superexchange processes which mediate a ferromagnetic interaction even in the insulating phase. Ferromagnetism is further promoted by the existence of orbital polarons: Charge fluctuations inside the polaron provide a strong local ferromagnetic coupling between sites close to a hole, hence establishing ferromagnetic clusters seen in experiment [TER97]. At sufficiently large hole densities these clusters start to interact, thereby forming a ferromagnetic state.

As was discussed above, orbital fluctuations are predominantly induced by the motion of holes. The loss of charge mobility in the insulating phase should therefore trigger static orbital order. A long-range orbitally ordered
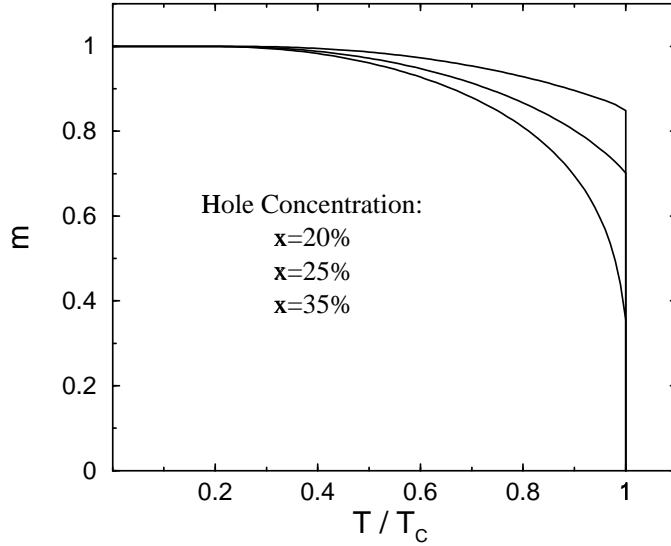
Figure 5.18: *Variation of the normalized magnetization m with temperature. At low hole concentrations (upper curve), the system is close to a transition to the small-polaron regime — a small increase in temperature then already sufficiently impedes the hole motion for polarons to form, resulting in a sharp drop of the magnetization. At large x (lower curve), the conventional double-exchange picture is recovered.*

state has in fact been experimentally detected in the insulating regions of $La_{0.88}Sr_{0.12}MnO_3$ [END99]. However, in general such an ordered state is expected to have orbital and Jahn-Teller glass features due to the presence of quenched orbital polarons, thereby reducing the uniform component of Jahn-Teller distortions. Finally it is worth to notice that the phase diagram in this theory is highly sensitive to the transfer amplitude t_0 as this parameter enters in the polaron binding energy.

5.6   Conclusion

In summary, we have shown that a spontaneous development of orbital-lattice order is in general insufficient to trigger the localization process in manganites. Rather an additional mechanism was identified: Orbital polarons were illustrated to represent an intrinsic feature of an orbitally degenerate Mott-Hubbard system and to play an important role in the physics of manganites. The binding energy of these orbital-hole bound states depends on the rate of orbital fluctuations and hence on the concentration of doped holes: Polarons can form at low doping levels where orbitals fluctuate only weakly

but they become unstable at higher levels of x. This scheme naturally introduces the hole concentration as an additional variable into the localization process. Most striking in this respect is the complete breakdown of metalicity observed below a critical hole concentration despite the fact that the system remains ferromagnetically ordered. On the other hand, orbital polarons become negligible at larger doping levels where the theory presented here converges onto a lattice-polaron double-exchange picture. Accounting for both orbital and lattice effects we are finally able to reproduce well the important aspects of the phase diagram of manganites. In general it can be concluded that a direct coupling between holes and surrounding orbitals is of crucial importance for the physics of manganites; its implications extend clearly beyond the metallic phase alone and can be expected to play an important role throughout the whole phase diagram.

Summary and Outlook

The central interest of our research presented in this thesis lies on transition metal oxides in which metalicity competes against a strong mutual repulsion between electrons. The groundstate of these correlated systems has to accommodate the tendency of electrons to blur their position and the local nature of the repulsive Coulomb potentials. This duality of itinerant and local features of the electronic state puts clear imprints onto the properties of these compounds. Throughout this thesis we have employed a simple yet powerful tool which allows us to handle these correlation effects in a transparent way: Electrons are decomposed into separate quasiparticles for spin, charge, and orbital degrees of freedom which are then treated starting from a mean-field level. While looking artificial at first sight, this theoretical approach has an analogue in the real world: Experiments indicate that spin and charge channels in high-T_c cuprates are, to a certain extent, decoupled from each other. Beyond this direct correspondence, the decoupling scheme is to be considered as an analytical instrument that makes correlated systems accessible by simple methods while preserving their characteristic features throughout the approximation procedure.

Specifically we have investigated the metallic state of high-T_c cuprates and of perovskite manganese oxides. The former are experimentally known to exhibit unconventional magnetic properties which are most pronounced at low hole-doping concentrations. Seizing the notion of a spin liquid, we are able to describe the different aspects of magnetism in the CuO_2 planes: (1) Spins form local singlets which are subject to strong fluctuations; (2) low-energy excitations are suppressed as a pseudogap opens in the spin sector; and (3) antiferromagnetic correlations signal the closeness to an antiferromagnetically ordered Néel state. In order to establish a link with experiment, we have studied the response of Cu spins to the insertion of impurities into the planes. Both magnetic and non-magnetic impurities are found to induce local magnetic moments in the proximity of the substitute ions. However, a detailed investigation shows these to be of different nature. In deriving expressions for the impurity effect onto NMR measurements, we were thereby

able to explain previously puzzling discrepancies in the behavior of magnetic and non-magnetic impurities. Furthermore, a curious non-Curie behavior exhibited by the impurity-induced NMR line broadening could be ascribed to the presence of antiferromagnetic correlations. We understand these results to clearly manifest the peculiar mixture of spin-singlet and antiferromagnetic correlations present in underdoped cuprates. In summary, our analysis shows that the magnetic properties of cuprates can be well described within a spin-liquid picture. However, at its present stage the approach overstates the separation of spin and charge. It therefore falls short in dealing with the recent discovery of residual Fermi-surface pieces deep inside the spin-gap regime. A theory that starts from spin-charge separation therefore has to be extended to allow for a temporary recombination of the two types of quasiparticles to form an electron. These very unconventional properties of the Fermi surface surely represent one of the most important challenges for future research on high-T_c cuprates.

Manganese oxides, just as cuprates, are subject to a strong on-site repulsion between itinerant electrons. However, the two systems differ in an important aspect: Manganites are double-exchange active, i.e., spins are ferromagnetically aligned in the metallic state at low temperatures. Only due to the double-degeneracy of orbital levels, two electrons can simultaneously occupy a single site and can hence sense the local interaction. To describe the strongly correlated nature of the metallic state of manganites, we are therefore lead to build upon the notion of an orbital liquid: In analogy to the separate treatment of spin and charge in a spin liquid, distinguished quasiparticles are assigned to orbital and charge degrees of freedom here. The validity and utility of this scheme is demonstrated by the results presented here which explain several peculiar aspects of metallic manganites that have previously eluded convincing explanations.

Employing an orbital-liquid picture, we are able to successfully ascribe the incoherency seen in the optical conductivity spectra of metallic manganites to scattering processes between correlated electrons. These are shown to lead to a strong suppression of the coherent Drude weight and to the appearance of a broad incoherent spectral tail extending up to frequencies comparable to the bare electronic bandwidth. Furthermore, we have estimated the constant of T-linear specific heat. Close correspondence with experiment clearly shows that this data does not rule out a correlated state as has been previously conjectured. In conclusion, our results imply that strong correlations are an important ingredient in the physics of manganites. Nevertheless, the multifaceted structure of the phase diagram alludes to a complex entanglement of different mechanisms that lie beyond the grasp of strong correlations alone. First to be noted in this respect is the important role of lattice modes: Due

to the orbital degeneracy, manganites are Jahn-Teller active and are therefore subject to a strong electron-phonon coupling. The interplay between correlated electrons and these lattice modes has important implications for the physics of manganites and deserves deeper insight.

The magnetic properties of metallic manganites are controlled by the double-exchange mechanism: The transfer of itinerant electrons interacting with localized core spins establishes ferromagnetic exchange links between neighboring sites. Strong correlations and orbital degeneracy superimpose on this exchange mechanism, thereby altering the magnetic behavior of the metallic state. Employing an orbital-liquid scheme, we have shown that the peculiar softening of the magnon spectrum seen in experiment is indeed a clear manifestation of the strongly correlated nature of degenerate e_g electrons. The presence of Jahn-Teller phonons further enhances the effect, which supports our previous assumption that lattice modes play an important role even in the metallic state of manganites. This interplay between double-exchange physics and orbital-lattice dynamics was found to become dominant close to a transition to orbital-lattice order. We thus conclude that the metallic state of manganites cannot be considered as being detached from the rest of the phase diagram; rather, instabilities that signal the imminent breakdown of metalicity intervene close to a phase transition. An important aspect of our analysis is the necessity to assume an instability towards *ferro-type* orbital-lattice ordering in order to fit the experimental data. This point had to be treated on a phenomenological level as our theory only accounts for *antiferro-type* orbital correlations mediated by Jahn-Teller and superexchange processes. What is missed is the role of kinetic energy in aligning the orbitals: A parallel orientation maximizes the inter-site transfer amplitude and hence stabilizes ferro-type orbital correlations at finite doping levels. A thorough study of the competition between Jahn-Teller effect and kinetic energy in controlling the character of orbital correlations is an important objective for future research in the field.

Finally, we have presented a theory of the metal-insulator transition in manganites that does, for the first time, account for the doping dependence of the phase diagram at low and intermediate hole concentrations. This work introduces the picture of orbital polarons: In an orbitally degenerate Mott-Hubbard system holes can polarize their orbital background. The metallic state hence becomes instable towards the formation of orbital-hole bound states below a critical doping level. This transition to a small-polaron regime goes hand in hand with a sharp drop of the bandwidth, making the system susceptible to localization. We study the interplay of polaron and double-exchange physics, extending our scheme to further account for a coupling between holes and lattice modes. Thereby we can successfully explain the

complete breakdown of metalicity below a critical hole concentration and the peculiar doping dependence of the Curie temperature in the colossal magnetoresistance regime. Furthermore, the experimental observation that ferromagnetism can prevail even in an insulating phase could be traced back to virtual exchange processes which lie beyond the access of conventional double-exchange theory. In summary, our results strongly suggest a direct orbital-hole coupling to be an intrinsic feature of manganites. While having elaborated on the implications for the phase diagram at low doping levels, a theory that extends to larger hole concentrations is still at lack. Recent experiments show an interrelation between orbital and charge structures in the charge-ordered regime at concentrations above 50%. We believe this observation to be closely related to the polarization effect underlying our orbital-polaron theory. In general, extensive research on manganites is still needed in order to gain deeper insight into the complex variation of the behavior as the full doping range is passed through.

Appendix A

Force-Force Correlation Functions

In this appendix we present the expressions for the force-force correlation functions that correspond to the Feynman diagrams in Fig. 3.5 of Chap. 3. Only the imaginary part is shown, the real part can be obtained by a Kramers-Kronig transformation. The following definitions are being used:

$$
\begin{aligned}
\omega_{\boldsymbol{k}} &= 2t\chi \left[3 - \epsilon_0(\boldsymbol{k}) \right] \\
\xi_{\boldsymbol{k}}^{\pm} &= (tx + J\chi) \left[-\epsilon_0(\boldsymbol{k}) \pm \sqrt{\epsilon_1^2(\boldsymbol{k}) + \epsilon_2^2(\boldsymbol{k})} \right] \\
u_{\boldsymbol{k}}^2 &= \frac{1}{2} \left[1 + \epsilon_1(\boldsymbol{k}) \big/ \sqrt{\epsilon_1^2(\boldsymbol{k}) + \epsilon_2^2(\boldsymbol{k})} \right] \\
v_{\boldsymbol{k}}^2 &= \frac{1}{2} \left[1 - \epsilon_1(\boldsymbol{k}) \big/ \sqrt{\epsilon_1^2(\boldsymbol{k}) + \epsilon_2^2(\boldsymbol{k})} \right] \\
\epsilon_0(\boldsymbol{k}) &= c_x + c_y + c_z \\
\epsilon_1(\boldsymbol{k}) &= \frac{1}{2}(c_x + c_y) - c_z \\
\epsilon_2(\boldsymbol{k}) &= \frac{\sqrt{3}}{2}(c_x - c_y) \\
\gamma_{\boldsymbol{k}} &= \frac{1}{2}(c_x + c_y) \\
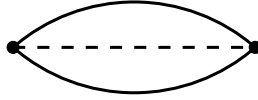\eta_{\boldsymbol{k}} &= \frac{1}{2}(c_x - c_y)
\end{aligned}
$$

with $c_\gamma = \cos k_\gamma$.

$$f''(\omega > 0) = -3\pi t^4 x^2 \sum_{\boldsymbol{k}} (\sin k_z \eta_{\boldsymbol{k}})^2 \, \Delta_\omega(\xi_{\boldsymbol{k}}^-, \xi_{\boldsymbol{k}}^+)$$

$$f''(\omega < 0) = -f''(\omega > 0)$$

with

$$\Delta_\omega(x, y) = \Theta_{-x}\Theta_y \delta(\omega + x - y).$$

$$f''(\omega > 0) = -16\pi t^4 x \sum_{\boldsymbol{kp}} \sin^2 p_z$$

$$\times \; \Big\{ (u_{\boldsymbol{k}} u_{\boldsymbol{k'}})^2 \Delta_\omega(\xi_{\boldsymbol{k}}^+, \xi_{\boldsymbol{k'}}^+) + (v_{\boldsymbol{k}} v_{\boldsymbol{k'}})^2 \Delta_\omega(\xi_{\boldsymbol{k}}^-, \xi_{\boldsymbol{k'}}^-)$$

$$+ (u_{\boldsymbol{k}} v_{\boldsymbol{k'}})^2 \Delta_\omega(\xi_{\boldsymbol{k}}^+, \xi_{\boldsymbol{k'}}^-) + (v_{\boldsymbol{k}} u_{\boldsymbol{k'}})^2 \Delta_\omega(\xi_{\boldsymbol{k}}^-, \xi_{\boldsymbol{k'}}^+) \Big\}$$

$$-3\pi t^4 x \sum_{\boldsymbol{kp}} (\sin k'_z \eta_{\boldsymbol{k'}})^2$$

$$\times \; \Big\{ (u_{\boldsymbol{k}} v_{\boldsymbol{k'}} - v_{\boldsymbol{k}} u_{\boldsymbol{k'}})^2 \left(\Delta_\omega(\xi_{\boldsymbol{k}}^+, \xi_{\boldsymbol{k'}}^+) + \Delta_\omega(\xi_{\boldsymbol{k}}^-, \xi_{\boldsymbol{k'}}^-) \right)$$

$$+ (u_{\boldsymbol{k}} u_{\boldsymbol{k'}} + v_{\boldsymbol{k}} v_{\boldsymbol{k'}})^2 \left(\Delta_\omega(\xi_{\boldsymbol{k}}^+, \xi_{\boldsymbol{k'}}^-) + \Delta_\omega(\xi_{\boldsymbol{k}}^-, \xi_{\boldsymbol{k'}}^+) \right) \Big\}$$

$$f''(\omega < 0) = -f''(\omega > 0)$$

with $\boldsymbol{k'} = \boldsymbol{k} + \boldsymbol{p}$ and

$$\Delta_\omega(x, y) = \Theta_{-x}\Theta_y \delta(\omega - \omega_{\boldsymbol{p}} + x - y).$$

$$
\begin{aligned}
f''(\omega > 0) \;=\;& -4\pi t^4 x^2 \sum_{\boldsymbol{kp}} \\
\times\;& \Big\{ a_{11}\Delta_\omega^{zz}(\xi_{\boldsymbol{k}}^+,\xi_{\boldsymbol{k'}}^+) + a_{22}\Delta_\omega^{zz}(\xi_{\boldsymbol{k}}^-,\xi_{\boldsymbol{k'}}^-) \\
& +a_{12}\Delta_\omega^{zz}(\xi_{\boldsymbol{k}}^+,\xi_{\boldsymbol{k'}}^-) + a_{21}\Delta_\omega^{zz}(\xi_{\boldsymbol{k}}^-,\xi_{\boldsymbol{k'}}^+) \Big\} \\[2ex]
& -12\pi t^4 x^2 \sum_{\boldsymbol{kp}} \\
\times\;& \Big\{ b_{11}\Delta_\omega^{xy}(\xi_{\boldsymbol{k}}^+,\xi_{\boldsymbol{k'}}^+) + b_{22}\Delta_\omega^{xy}(\xi_{\boldsymbol{k}}^-,\xi_{\boldsymbol{k'}}^-) \\
& +b_{12}\Delta_\omega^{xy}(\xi_{\boldsymbol{k}}^+,\xi_{\boldsymbol{k'}}^-) + b_{21}\Delta_\omega^{xy}(\xi_{\boldsymbol{k}}^-,\xi_{\boldsymbol{k'}}^+) \Big\} \\[2ex]
f''(\omega < 0) \;=\;& -f''(\omega > 0)
\end{aligned}
$$

with $\boldsymbol{k'} = \boldsymbol{k} + \boldsymbol{p}$ and

$$
\begin{aligned}
a_{11} \;=\;& \sin^2 k_z' \left(\gamma_{\boldsymbol{k}} u_{\boldsymbol{k}} u_{\boldsymbol{k'}} - \sqrt{3}\eta_{\boldsymbol{k}} v_{\boldsymbol{k}} u_{\boldsymbol{k'}} \right)^2 + \sin^2 k_z \left(\gamma_{\boldsymbol{k'}} u_{\boldsymbol{k}} u_{\boldsymbol{k'}} - \sqrt{3}\eta_{\boldsymbol{k'}} u_{\boldsymbol{k}} v_{\boldsymbol{k'}} \right)^2 \\
a_{22} \;=\;& \sin^2 k_z' \left(\gamma_{\boldsymbol{k}} v_{\boldsymbol{k}} v_{\boldsymbol{k'}} + \sqrt{3}\eta_{\boldsymbol{k}} u_{\boldsymbol{k}} v_{\boldsymbol{k'}} \right)^2 + \sin^2 k_z \left(\gamma_{\boldsymbol{k'}} v_{\boldsymbol{k}} v_{\boldsymbol{k'}} + \sqrt{3}\eta_{\boldsymbol{k'}} v_{\boldsymbol{k}} u_{\boldsymbol{k'}} \right)^2 \\
a_{12} \;=\;& \sin^2 k_z' \left(\gamma_{\boldsymbol{k}} u_{\boldsymbol{k}} v_{\boldsymbol{k'}} - \sqrt{3}\eta_{\boldsymbol{k}} v_{\boldsymbol{k}} v_{\boldsymbol{k'}} \right)^2 + \sin^2 k_z \left(\gamma_{\boldsymbol{k'}} u_{\boldsymbol{k}} v_{\boldsymbol{k'}} + \sqrt{3}\eta_{\boldsymbol{k'}} u_{\boldsymbol{k}} u_{\boldsymbol{k'}} \right)^2 \\
a_{21} \;=\;& \sin^2 k_z' \left(\gamma_{\boldsymbol{k}} v_{\boldsymbol{k}} u_{\boldsymbol{k'}} + \sqrt{3}\eta_{\boldsymbol{k}} u_{\boldsymbol{k}} u_{\boldsymbol{k'}} \right)^2 + \sin^2 k_z \left(\gamma_{\boldsymbol{k'}} v_{\boldsymbol{k}} u_{\boldsymbol{k'}} - \sqrt{3}\eta_{\boldsymbol{k'}} v_{\boldsymbol{k}} v_{\boldsymbol{k'}} \right)^2 \\[2ex]
b_{11} \;=\;& \sin^2 k_z' \left(\eta_{\boldsymbol{k}} u_{\boldsymbol{k}} u_{\boldsymbol{k'}} - \sqrt{3}\gamma_{\boldsymbol{k}} v_{\boldsymbol{k}} u_{\boldsymbol{k'}} \right)^2 + \sin^2 k_z \left(\eta_{\boldsymbol{k'}} u_{\boldsymbol{k}} u_{\boldsymbol{k'}} - \sqrt{3}\gamma_{\boldsymbol{k'}} u_{\boldsymbol{k}} v_{\boldsymbol{k'}} \right)^2 \\
b_{22} \;=\;& \sin^2 k_z' \left(\eta_{\boldsymbol{k}} v_{\boldsymbol{k}} v_{\boldsymbol{k'}} + \sqrt{3}\gamma_{\boldsymbol{k}} u_{\boldsymbol{k}} v_{\boldsymbol{k'}} \right)^2 + \sin^2 k_z \left(\eta_{\boldsymbol{k'}} v_{\boldsymbol{k}} v_{\boldsymbol{k'}} + \sqrt{3}\gamma_{\boldsymbol{k'}} v_{\boldsymbol{k}} u_{\boldsymbol{k'}} \right)^2 \\
b_{12} \;=\;& \sin^2 k_z' \left(\eta_{\boldsymbol{k}} u_{\boldsymbol{k}} v_{\boldsymbol{k'}} - \sqrt{3}\gamma_{\boldsymbol{k}} v_{\boldsymbol{k}} v_{\boldsymbol{k'}} \right)^2 + \sin^2 k_z \left(\eta_{\boldsymbol{k'}} u_{\boldsymbol{k}} v_{\boldsymbol{k'}} + \sqrt{3}\gamma_{\boldsymbol{k'}} u_{\boldsymbol{k}} u_{\boldsymbol{k'}} \right)^2 \\
b_{21} \;=\;& \sin^2 k_z' \left(\eta_{\boldsymbol{k}} v_{\boldsymbol{k}} u_{\boldsymbol{k'}} + \sqrt{3}\gamma_{\boldsymbol{k}} u_{\boldsymbol{k}} u_{\boldsymbol{k'}} \right)^2 + \sin^2 k_z \left(\eta_{\boldsymbol{k'}} v_{\boldsymbol{k}} u_{\boldsymbol{k'}} - \sqrt{3}\gamma_{\boldsymbol{k'}} v_{\boldsymbol{k}} v_{\boldsymbol{k'}} \right)^2
\end{aligned}
$$

$$
\begin{aligned}
\Delta_\omega^{zz}(x, y) \;=\;& \Theta_{-x}\, \Theta_y\, \Theta_{\omega+x-y}\, \rho_{\boldsymbol{p}}^{zz}(\omega + x - y) \\
\Delta_\omega^{xy}(x, y) \;=\;& \Theta_{-x}\, \Theta_y\, \Theta_{\omega+x-y}\, \rho_{\boldsymbol{p}}^{xy}(\omega + x - y)
\end{aligned}
$$

$$
\begin{aligned}
\rho_{\boldsymbol{k}}^{zz}(\omega > 0) \;=\; & \frac{1}{4} \sum_{\boldsymbol{k}} \\
\times \;\; & \Big\{ (u_{\boldsymbol{k}} u_{\boldsymbol{k}'} - v_{\boldsymbol{k}} v_{\boldsymbol{k}'})^2 \left(\Delta_\omega(\xi_{\boldsymbol{k}}^+, \xi_{\boldsymbol{k}'}^+) + \Delta_\omega(\xi_{\boldsymbol{k}}^-, \xi_{\boldsymbol{k}'}^-) \right) \\
& + (u_{\boldsymbol{k}} v_{\boldsymbol{k}'} + v_{\boldsymbol{k}} u_{\boldsymbol{k}'})^2 \left(\Delta_\omega(\xi_{\boldsymbol{k}}^+, \xi_{\boldsymbol{k}'}^-) + \Delta_\omega(\xi_{\boldsymbol{k}}^-, \xi_{\boldsymbol{k}'}^+) \right) \Big\}
\end{aligned}
$$

$$
\begin{aligned}
\rho_{\boldsymbol{k}}^{xy}(\omega > 0) \;=\; & \frac{1}{2} \sum_{\boldsymbol{k}} \\
\times \;\; & \Big\{ \left((u_{\boldsymbol{k}} v_{\boldsymbol{k}'})^2 + (v_{\boldsymbol{k}} u_{\boldsymbol{k}'})^2 \right) \left(\Delta_\omega(\xi_{\boldsymbol{k}}^+, \xi_{\boldsymbol{k}'}^+) + \Delta_\omega(\xi_{\boldsymbol{k}}^-, \xi_{\boldsymbol{k}'}^-) \right) \\
& + \left((u_{\boldsymbol{k}} u_{\boldsymbol{k}'})^2 + (v_{\boldsymbol{k}} v_{\boldsymbol{k}'})^2 \right) \left(\Delta_\omega(\xi_{\boldsymbol{k}}^+, \xi_{\boldsymbol{k}'}^-) + \Delta_\omega(\xi_{\boldsymbol{k}}^-, \xi_{\boldsymbol{k}'}^+) \right) \Big\}
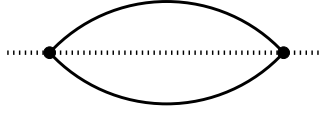\end{aligned}
$$

with

$$
\Delta_\omega(x, y) = \Theta_{-x} \Theta_y \delta(\omega + x - y).
$$

Appendix B

Magnon Self Energies

In this appendix we present the expressions for the magnon self energy that correspond to the Feynman diagrams in Fig. 4.5 of Chap. 4. Only the imaginary part is shown, the real part can be obtained by a Kramers-Kronig transformation. The same notations as in Appendix A are being used and in addition

$$\bar{\omega}_{\boldsymbol{k}} = \frac{x + x_0}{4}\omega_{\boldsymbol{k}}$$

$$
\begin{aligned}
\Sigma''(\omega > 0, \boldsymbol{p}) \;=\;& -\frac{\pi}{16}\sum_{\boldsymbol{k}\boldsymbol{k}'} \\
\times\;& \Big\{ b_{11}^2 \Delta_\omega(\xi_{\boldsymbol{k}}^+, \xi_{\boldsymbol{k}'}^+) + b_{22}^2 \Delta_\omega(\xi_{\boldsymbol{k}}^-, \xi_{\boldsymbol{k}'}^-) \\
& + b_{12}^2 \Delta_\omega(\xi_{\boldsymbol{k}}^+, \xi_{\boldsymbol{k}'}^-) + b_{21}^2 \Delta_\omega(\xi_{\boldsymbol{k}}^-, \xi_{\boldsymbol{k}'}^+) \Big\}
\end{aligned}
$$

$$\Sigma''(\omega < 0, \boldsymbol{p}) \;=\; 0$$

with

$$
\begin{aligned}
b_{11} &= +a_0\theta_+ + a_1\theta_- - a_2\phi_+ \\
b_{22} &= +a_0\theta_+ - a_1\theta_- + a_2\phi_+ \\
b_{12} &= +a_0\phi_- - a_1\phi_+ - a_2\theta_- \\
b_{21} &= -a_0\phi_- - a_1\phi_+ - a_2\theta_-
\end{aligned}
$$

where

$$\begin{aligned}
\theta_\pm &= u_{\bm{k}} u_{\bm{k}'} \pm v_{\bm{k}} v_{\bm{k}'} \\
\phi_\pm &= u_{\bm{k}} v_{\bm{k}'} \pm v_{\bm{k}} u_{\bm{k}'}
\end{aligned}$$

$$a_i = (x + x_0)[\epsilon_i(\bm{k}) - \epsilon_i(\bm{k} + \bm{p})] + x_0[\epsilon_i(\bm{k}') - \epsilon_i(\bm{k}' - \bm{p})]$$
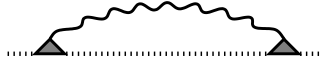
and

$$\Delta_\omega(x, y) = \Theta_{-x} \Theta_y \delta(\omega - \bar{\omega}_{\bm{p}+\bm{k}-\bm{k}'} + x - y).$$

$$\Sigma''(\omega > 0, \bm{p}) = -\frac{\pi x}{16} \sum_{\bm{k}} (\omega_{\bm{k}'} - \omega_{\bm{k}})^2 \delta(\omega - \bar{\omega}_{\bm{k}'} - \omega_{\bm{k}})$$

$$\Sigma''(\omega < 0, \bm{p}) = 0$$

with $\bm{k}' = \bm{k} + \bm{p}$.

$$\begin{aligned}
\Sigma''(\omega > 0, \bm{p}) &= -\frac{\pi}{16} E_{\text{JT}} a_0^2 \omega_0 \sum_{\bm{k}} \\
&\times \left\{ f_{\bm{k}\bm{p}}^+ \Delta_{\bm{k}}^+(\omega - \omega_{\bm{k}'} - \omega_{\bm{k}}^+) \right. \\
&\left. + f_{\bm{k}\bm{p}}^- \Delta_{\bm{k}}^-(\omega - \omega_{\bm{k}'} - \omega_{\bm{k}}^-) \right\}
\end{aligned}$$

$$\Sigma''(\omega < 0, \bm{p}) = 0$$

with $\bm{k}' = \bm{k} + \bm{p}$ and the phonon dispersion

$$\omega_{\bm{k}}^\pm = \omega_0 \left(\bar{\kappa}_{0\bm{k}} \pm \sqrt{\bar{\kappa}_{1\bm{k}}^2 + \bar{\kappa}_{2\bm{k}}^2} \right)$$

where

$$
\begin{aligned}
\bar{\kappa}_{0\boldsymbol{k}} &= 1 + k_1 \epsilon_0(\boldsymbol{k}) \\
\bar{\kappa}_{1\boldsymbol{k}} &= k_1 \epsilon_1(\boldsymbol{k}) \\
\bar{\kappa}_{2\boldsymbol{k}} &= k_1 \epsilon_2(\boldsymbol{k})
\end{aligned}
$$

Further

$$
\begin{aligned}
f_{\boldsymbol{kp}}^{+} &= \frac{\omega_0}{\omega_{\boldsymbol{k}}^{+}} \left(\bar{\lambda}_{\boldsymbol{kp}}^{(1)} \cos\Theta_{\boldsymbol{k}} + \bar{\lambda}_{\boldsymbol{kp}}^{(2)} \sin\Theta_{\boldsymbol{k}} \right)^2 \\
f_{\boldsymbol{kp}}^{-} &= \frac{\omega_0}{\omega_{\boldsymbol{k}}^{-}} \left(\bar{\lambda}_{\boldsymbol{kp}}^{(1)} \sin\Theta_{\boldsymbol{k}} - \bar{\lambda}_{\boldsymbol{kp}}^{(2)} \cos\Theta_{\boldsymbol{k}} \right)^2
\end{aligned}
$$

with

$$
\bar{\lambda}_{\boldsymbol{kp}}^{(i)} = \epsilon_i(\boldsymbol{k}) - \epsilon_i(\boldsymbol{p}) - \epsilon_i(\boldsymbol{k}')
$$

and

$$
\begin{aligned}
\cos\Theta_{\boldsymbol{k}} &= \frac{1}{\sqrt{2}} \left(1 - \frac{\bar{\kappa}_{1\boldsymbol{k}}}{\sqrt{\bar{\kappa}_{1\boldsymbol{k}}^2 + \bar{\kappa}_{2\boldsymbol{k}}^2}} \right)^{1/2} \\
\sin\Theta_{\boldsymbol{k}} &= \frac{1}{\sqrt{2}} \left(1 + \frac{\bar{\kappa}_{1\boldsymbol{k}}}{\sqrt{\bar{\kappa}_{1\boldsymbol{k}}^2 + \bar{\kappa}_{2\boldsymbol{k}}^2}} \right)^{1/2} \operatorname{sign}(\bar{\kappa}_{1\boldsymbol{k}})
\end{aligned}
$$

Finally

$$
\Delta_{\boldsymbol{k}}^{\nu}(x) = \Theta_x \left[\rho_{\nu}^{\mathrm{ph}}(x, \boldsymbol{k}) - \rho_{\nu}^{\mathrm{ph}}(-x, \boldsymbol{k}) \right].
$$

Bibliography

[AFF88a] I. Affleck and J. Marston, Phys. Rev. B **37**, 3774 (1988).

[AFF88b] I. Affleck, Z. Zou, T. Hsu, and P. W. Anderson, Phys. Rev. B **38**, 745 (1988).

[ALE94] A. S. Alexandrov, V. V. Kabanov, and D. K. Ray, Phys. Rev. B **49**, 9915 (1994).

[ALL91] H. Alloul, P. Mendels, H. Casalta, J.-F. Marucco, and J. Arabski, Phys. Rev. Lett. **67**, 3140 (1991).

[AND55] P. W. Anderson and H. Hasegawa, Phys. Rev. **100**, 675 (1955).

[AND87] P. W. Anderson, Science **235**, 1196 (1987).

[AND97] P. W. Anderson, *The Theory of Superconductivity in the High-T_c Cuprates* (Princeton University Press, Princeton, 1997).

[ARO88] D. Arovas and A. Auerbach, Phys. Rev. B **38**, 316 (1988).

[AUE94] A. Auerbach, *Interacting Electrons and Quantum Magnetism* (Springer-Verlag, New York, 1994).

[BAL95] A. V. Balatsky, M. I. Salkola, and A. Rosengren, Phys. Rev. B **51**, 15 547 (1995).

[BAR95] V. Barzykin and D. Pines, Phys. Rev. B **52**, 13 585 (1995).

[BAS87] G. Baskaran, Z. Zou, and P. W. Anderson, Solid State Commun. **63**, 973 (1987).

[BAS88] G. Baskaran and P. W. Anderson, Phys. Rev. B **37**, 580 (1988).

[BED86] J. G. Bednorz and K. A. Müller, Z. Phys. B **64**, 189 (1986).

[BIL96]   S. J. L. Billinge, R. G. DiFrancesco, G. H. Kwei, J. J. Neumeier, and J. D. Thompson, Phys. Rev. Lett. **77**, 715 (1996).

[BIR88]   R. J. Birgeneau, D. R. Gabbe, H. P. Jenssen, M. A. Kastner, P. J. Picone, T. R. Thurston, G. Shirane, Y. Endoh, M. Sato, K. Yamada, Y. Hidaka, M. Oda, Y. Enomoto, M. Suzuki, and T. Murakami, Phys. Rev. B **38**, 6614 (1988).

[BIR89]   R. J. Birgeneau and G. Shirane, in *Physical Properties of High Temperature Superconductors*, edited by D. M. Ginsberg (World Scientific, Singapore, 1989), Vol. 1.

[BOB97a]   J. Bobroff, H. Alloul, Y. Yoshinari, A. Keren, P. Mendels, N. Blanchard, G. Collin, and J.-F. Marucco, Phys. Rev. Lett. **79**, 2117 (1997).

[BOB97b]   J. Bobroff, H. Alloul, Y. Yoshinari, P. Mendels, N. Blanchard, G. Collin, and J.-F. Marucco, Physica C **282-287**, 1389 (1997).

[BOO98]   C. H. Booth, F. Bridges, G. H. Kwei, J. M. Lawrence, A. L. Cornelius, and J. J. Neumeier, Phys. Rev. Lett. **80**, 853 (1998).

[BOU96]   P. Bourges, L. P. Regnault, Y. Sidis, and C. Vettier, Phys. Rev. B **53**, 876 (1996).

[CAP99a]   M. Capone, M. Grilli, and W. Stephan, J. Superconductivity **12**, 75 (1999).

[CAP99b]   M. Capone, M. Grilli, and W. Stephan, cond-mat/9902317.

[CHA93]   A. Chainani, M. Mathew, and D. D. Sarma, Phys. Rev. B **47**, 15 397 (1993).

[CHE99]   S.-W. Cheong and H. Y. Hwang (unpublished).

[COR99]   J. Corson, R. Mallozzi, J. Orenstein, J. N. Eckstein, and I. Bozovic, Nature (London) **398**, 221 (1999).

[DAG94]   E. Dagotto, Rev. Mod. Phys. **66**, 763 (1994).

[DEG60]   P.-G. de Gennes, Phys. Rev. **118**, 141 (1960).

[DES98]   D. S. Dessau and Z.-X. Shen, in *Colossal Magnetoresistive Oxides*, edited by Y. Tokura (Gordon and Breach, 1998).

[DIN96] H. Ding, T. Yokoya, J. C. Campuzano, T. Takahashi, M. Randeria, M. R. Norman, T. Mochiku, K. Kadowaki, and J. Giapintzakis, Nature (London) **382**, 51 (1996).

[END99] Y. Endoh, K. Hirota, S. Ishihara, S. Okamoto, Y. Murakami, A. Nishizawa, T. Fukuda, H. Kimura, H. Nojiri, K. Kaneko, and S. Maekawa, Phys. Rev. Lett. **82**, 4328 (1999).

[EME95] V. J. Emery and S. A. Kivelson, Nature (London) **374**, 434 (1995).

[FAB97] M. Fabrizio and R. Mélin, Phys. Rev. Lett. **78**, 3382 (1997).

[FAB98] M. Fabrizio, M. Altarelli, and M. Benfatto, Phys. Rev. Lett. **80**, 3400 (1998).

[FEI99] L. F. Feiner and A. M. Oleś, Phys. Rev. B **59**, 3295 (1999).

[FER98] J. A. Fernandez-Baca, P. Dai, H. Y. Hwang, C. Kloc, and S.-W. Cheong, Phys. Rev. Lett. **80**, 4012 (1998).

[FIN90] A. M. Finkelstein, V. E. Kataev, E. F. Kukovitskii, and G. B. Teitelbaum, Physica C **168**, 370 (1990).

[FOR75] D. Forster, *Hydrodynamic Fluctuations, Broken Symmetry, and Correlation Functions*, (W. A. Benjamin, Reading, 1975).

[FRA99] J. P. Franck, I. Isaac, W. Chen, J. Chrzanowski, J. C. Irwin, and C. C. Homes, J. Superconductivity **12**, 263 (1999).

[FUJ89] A. Fujimori, S. Takekawa, E. Takayama-Muromachi, Y. Uchida, A. Ono, T. Takahashi, Y. Okabe, and H. Katayama-Yoshida, Phys. Rev. B **39**, 2255 (1989).

[FUK88] H. Fukuyama, Y. Hasegawa, and Y. Suzumura, Physica C **153-155**, 1630 (1988).

[FUK92] H. Fukuyama, Prog. Theo. Phys. Suppl. **108**, 287 (1992).

[FUK96] H. Fukuyama, N. Nagaosa, M. Saito, and T. Tanimoto, J. Phys. Soc. Jpn. **65**, 2377 (1996).

[FUL95] P. Fulde, *Electron Correlations in Molecules and Solids*, 3rd ed. (Springer-Verlag, Berlin, 1995).

[FUR99] N. Furukawa, cond-mat/9905133.

[GOE72] W. Götze and P. Wölfle, Phys. Rev. B **6**, 1226 (1972).

[GOG97] A. O. Gogolin, A. A. Nersesyan, A. M. Tsvelik, and L. Yu, Nucl. Phys. B **540**, 705 (1999).

[GOO55] J. B. Goodenough, Phys. Rev. **100**, 564 (1955).

[HAZ90] R. M. Hazen, in *Physical Properties of High Temperature Super-conductors*, edited by D. M. Ginsberg (World Scientific, Singapore, 1990), Vol. 2.

[HOM93] C. C. Homes, C. T. Timusk, R. Liang, D. A. Bonn, and W. N. Hardy, Phys. Rev. Lett. **71**, 1645 (1993).

[HWA95] H. Y. Hwang, S.-W. Cheong, P. G. Radaelli, M. Marezio, and B. Batlogg, Phys. Rev. Lett. **75**, 914 (1995).

[HWA96] H. Y. Hwang, S.-W. Cheong, N. P. Ong, and B. Batlogg, Phys. Rev. Lett. **77**, 2041 (1996).

[HWA98] H. Y. Hwang, P. Dai, S.-W. Cheong, G. Aeppli, D. A. Tennant, and H. A. Mook, Phys. Rev. Lett. **80**, 1316 (1998).

[IMA98] M. Imada, A. Fujimori, and Y. Tokura, Rev. Mod. Phys. **70**, 1039 (1998).

[IMI93] T. Imai, C. P. Slichter, K. Yoshimura, and K. Kosuge, Phys. Rev. Lett. **70**, 1002 (1993).

[IOF89] L. B. Ioffe and A. Larkin, Phys. Rev. B **39**, 8988 (1989).

[IOF90] L. B. Ioffe and G. Kotliar, Phys. Rev. B **42**, 10 348 (1990).

[ISD93] K. Ishida, Y. Kitaoka, N. Ogata, T. Kamino, K. Asayama, J. R. Cooper, and N. Athanassopoulou, J. Phys. Soc. Jpn. **62**, 2803 (1993).

[ISD96] K. Ishida, Y. Kitaoka, K. Yamazoe, K. Asayama, and Y. Yamada, Phys. Rev. Lett. **76**, 531 (1996).

[ISH96] S. Ishihara, J. Inoue, and S. Maekawa, Physica C **263**, 130 (1996).

[ISH97a] S. Ishihara, M. Yamanaka, and N. Nagaosa, Phys. Rev. B **56**, 686 (1997).

[ISH97b]   S. Ishihara, J. Inoue, and S. Maekawa, Phys. Rev. B **55**, 8280 (1997).

[ISH98]   S. Ishihara and S. Maekawa, Phys. Rev. Lett. **80**, 3799 (1998).

[IYE90]   Y. Iye, in *Physical Properties of High Temperature Supercon-ductors*, edited by D. M. Ginsberg (World Scientific, Singapore, 1989), Vol. 3.

[JIN94]   S. Jin, T. H. Tiefel, M. McCormack, R. A. Fastnacht, R. Ramesh, and L. H. Chen, Science **264**, 413 (1994).

[JOH89]   D. C. Johnston, Phys. Rev. Lett. **62**, 957 (1989).

[JON50]   G. H. Jonker and J. H. Van Santen, Physica (Utrecht) **16**, 337 (1950).

[KAE89]   C. L. Kane, P. A. Lee, and N. Read, Phys. Rev. B **39**, 6880 (1989).

[KAN60]   J. Kanamori, J. Appl. Phys. **31**, 14S (1960).

[KAN63]   J. Kanamori, Prog. Theor. Phys. **30**, 275 (1963).

[KAP96]   S. G. Kaplan, M. Quijada, H. D. Drew, D. B. Tanner, G. C. Xiong, R. Ramesh, C. Kwon, and T. Venkatesan, Phys. Rev. Lett. **77**, 2081 (1996).

[KAW97]   H. Kawano, R. Kajimoto, H. Yoshizawa, Y. Tomioka, H. Kuwa-hara, and Y. Tokura, Phys. Rev. Lett. **78**, 4253 (1997).

[KHA97a]   G. Khaliullin, S. Krivenko, R. Kilian, and P. Fulde, Physica C **282-287**, 1749 (1997).

[KHA97b]   G. Khaliullin, R. Kilian, S. Krivenko, and P. Fulde, Phys. Rev. B **56**, 11 882 (1997).

[KHA99a]   G. Khaliullin, S. Krivenko, R. Kilian, and P. Fulde, Physica B **259-261**, 504 (1999).

[KHA99b]   G. Khaliullin, R. Kilian, S. Krivenko, and P. Fulde, Physica C, **317** 494 (1999).

[KHA99c]   G. Khaliullin and R. Kilian, cond-mat/9904316.

[KHA99d]   G. Khaliullin and R. Kilian, cond-mat/9904318.

[KIL98]   R. Kilian and G. Khaliullin, Phys. Rev. B **58**, R11 841 (1998).

[KIL99a]   R. Kilian, S. Krivenko, G. Khaliullin, and P. Fulde, Phys. Rev. B **59**, 14 432 (1999).

[KIL99b]   R. Kilian and G. Khaliullin, Physica B **259-261**, 805 (1999).

[KIL99c]   R. Kilian and G. Khaliullin, cond-mat/9904317 and cond-mat/9906045.

[KOT88a]   G. Kotliar, Phys. Rev. B **37**, 3664 (1988).

[KOT88b]   G. Kotliar and J. Liu, Phys. Rev. B **38**, 5142 (1988).

[KRI95]   S. Krivenko and G. Khaliullin, Physica C **244**, 83 (1995).

[KUB72]   K. Kubo and N. Ohata, J. Phys. Soc. Jpn. **33**, 21 (1972).

[KUG73]   K. I. Kugel and D. I. Khomskii, Sov. Phys. JETP **37**, 725 (1973).

[KUG82]   K. I. Kugel and D. I. Khomskii, Sov. Phys. Usp. **25**, 231 (1982).

[LAN98]   A. Lanzara, N. L. Saini, M. Brunelli, F. Natali, A. Bianconi, P. G. Radaelli, and S.-W. Cheong, Phys. Rev. Lett. **81**, 878 (1998).

[LAU98]   M. Laukamp, G. B. Martins, C. Gazza, A. L. Malvezzi, E. Dagotto, P. M. Hansen, A. C. Lopez, and J. Riera, Phys. Rev. B **57**, 10 755 (1998).

[LEE92]   P. A. Lee and N. Nagaosa, Phys. Rev. B **46**, 5621 (1992).

[LEE98]   P. A. Lee, cond-mat/9812226.

[LOE96]   A. G. Loeser, Z.-X. Chen, S. S. Dessau, D. S. Marshall, C. H. Park, P. Fournier, and A. Kapitulnik, Science **273**, 325 (1996).

[LOR93]   J. W. Loram, K. Mirza, J. Cooper, and W. Y. Liang, Phys. Rev. Lett. **71**, 1740 (1993).

[LOU97]   D. Louca, T. Egami, E. L. Brosha, H. Röder, and A. R. Bishop, Phys. Rev. B **56**, R8475 (1997).

[LYN96]   J. W. Lynn, R. W. Erwin, J. A. Borchers, Q. Huang, A. Santoro, J. L. Peng, and Z. Y. Li, Phys. Rev. Lett. **76**, 4046 (1996).

[MAE98a]   R. Maezono, S. Ishihara, and N. Nagaosa, Phys. Rev. B **58**, 11 583 (1998).

[MAE98b] R. Maezono, S. Ishihara, and N. Nagaosa, Phys. Rev. B **57**, R13 993 (1998).

[MAH90] G. D. Mahan, *Many-Particle Physics* (Plenum Press, New York, 1990).

[MAN94] A. V. Mahan, H. Alloul, G. Collin, and J.-F. Marucco, Phys. Rev. Lett. **72**, 3100 (1994).

[MAR97] G. B. Martins, M. Laukamp, J. Riera, and E. Dagotto, Phys. Rev. Lett. **78**, 3563 (1997).

[MAS89] J. B. Marston and I. Affleck, Phys. Rev. B **39**, 11 538 (1989).

[MAS99] J. B. Marston, cond-mat/9904437.

[MAT96] M. C. Martin, G. Shirane, Y. Endoh, K. Hirota, Y. Moritomo, and Y. Tokura, Phys. Rev. B **53**, R14 285 (1996).

[MAZ91] G. Martinez and P. Horsch, Phys. Rev. B **44**, 317 (1991).

[MEL97] C. A. R. Sa de Melo, M. Randeria, and J. R. Engelbrecht, Phys. Rev. B **55**, 15 153 (1997).

[MEN94] P. Mendels, H. Alloul, G. Collin, N. Blanchard, J.-F. Marucco, and J. Bobroff, Physica C **235-240**, 1595 (1994).

[MEN99] P. Mendels, J. Bobroff, G. Collin, H. Alloul, M. Gabay, J.-F. Marucco, N. Blanchard, and B. Grenier, cond-mat/9904295.

[MIL95] A. J. Millis, P. B. Littlewood, and B. I. Shraiman, Phys. Rev. Lett. **74**, 5144 (1995).

[MIL96a] A. J. Millis, B. Shraiman, and R. Mueller, Phys. Rev. Lett. **77**, 175 (1996).

[MIL96b] A. J. Millis, R. Mueller, and B. I. Shraiman, Phys. Rev. B **54**, 5389 (1996).

[MIL96c] A. J. Millis, R. Mueller, and B. I. Shraiman, Phys. Rev. B **54**, 5405 (1996).

[MIL98] A. J. Millis, Nature (London) **392**, 147 (1998).

[MIL99] A. J. Millis, Nature (London) **398**, 193 (1999).

[MON94]   P. Monthoux and D. Pines, Phys. Rev. B **50**, 16 015 (1994).

[MOR96]   Y. Morimoto, A. Asamitsu, H. Kuwahara, and Y. Tokura, Nature (London) **380**, 141 (1996).

[MOT98]   Y. Moritomo, T. Akimoto, A. Nakamura, K. Ohoyama, and M. Ohashi, Phys. Rev. B **58**, 5544 (1998).

[MRR98]   D. K. Morr, J. Schmalian, R. Stern, and C. P. Slichter, Phys. Rev. B **58**, 11 193 (1998).

[MTT81]   D. C. Mattis, *The Theory of Magnetism* (Springer-Verlag, Berlin, 1981), Vol. 1, p. 90.

[MUE96]   E. Müller-Hartmann and E. Dagotto, Phys. Rev. B **54**, R6819 (1996).

[MUR98]   Y. Murakami, J. P. Gill, D. Gibbs, M. Blume, I. Koyama, M. Tanaka, H. Kawata, T. Arima, Y. Tokura, K. Hirota, and Y. Endoh, Phys. Rev. Lett. **81**, 582 (1998).

[NAG90]   N. Nagaosa and P. A. Lee, Phys. Rev. Lett. **64**, 2450 (1990).

[NAG95]   N. Nagaosa and T. K. Ng, Phys. Rev. B **51**, 15 588 (1995).

[NAG96]   N. Nagaosa, A. Furusaki, M. Sigrist, and H. Fukuyama, J. Phys. Soc. Jpn. **65**, 3724 (1996).

[NAG97]   N. Nagaosa and P. A. Lee, Phys. Rev. Lett. **79**, 3755 (1997).

[NAG98]   N. Nagaosa, S. Murakami, and H. C. Lee, Phys. Rev. B **57**, R6767 (1998).

[NAK94]   T. Nakano, M. Oda, C. Manabe, N. Momono, Y. Miura, and M. Ido, Phys. Rev. B **49**, 16 000 (1994).

[OKI95]   Y. Okimoto, T. Katsufuji, T. Ishikawa, A. Urushibara, T. Arima, and Y. Tokura, Phys. Rev. Lett. **75**, 109 (1995).

[OKI97]   Y. Okimoto, T. Katsufuji, T. Ishikawa, T. Arima, and Y. Tokura, Phys. Rev. B **55**, 4206 (1997).

[OKU98]   T. Okuda, A. Asamitsu, Y. Tomioka, T. Kimura, Y. Taguchi, and Y. Tokura, Phys. Rev. Lett. **81**, 3203 (1998).

[PEP98]   C. Pépin and P. A. Lee, Phys. Rev. Lett. **81**, 2779 (1998).

[PER96]   T. G. Perring, G. Aeppli, S. M. Hayden, S. A. Carter, J. P. Re-
          meika, and S.-W. Cheong, Phys. Rev. Lett. **77**, 711 (1996).

[PIC96]   W. E. Pickett and D. J. Singh, Phys. Rev. B **53**, 1146 (1996).

[PIN97]   D. Pines, Z. Phys. B **103**, 129 (1997).

[RAM97]   A. P. Ramirez, J. Phys.: Condens. Matter **9**, 8171 (1997).

[REA83]   N. Read and D. M. Newns, J. Phys. C **16**, 3273 (1983).

[REN98]   C. Renner, B. Revaz, J. Y. Genoud, K. Dadowaki, and O. Fischer,
          Phys. Rev. Lett. **80**, 149 (1998).

[RIS94]   R. M. Riseman, H. Alloul, A. V. Mahajan, P. Mendels, N. Blan-
          chard, G. Collin, and J.-F. Marucco, Physica C **235-240**, 1593
          (1994).

[ROE96]   H. Röder, J. Zang, and A. R. Bishop, Phys. Rev. Lett. **76**, 1356
          (1996).

[RUS74]   G. S. Rushbrooke, G. A. Baker, and P. J. Wood, in *Phase Tran-
          sitions and Critical Phenomena*, edited by C. Domb and M. S.
          Green (Academic, New York, 1974).

[SAI95]   S. Saitoh, A. E. Bocquet, T. Mizokawa, H. Namatame, A. Fuji-
          mori, M. Abbate, Y. Takeda, and M. Takano, Phys. Rev. B **51**,
          13 942 (1995).

[SAR96]   D. D. Sarma, N. Shanthi, S. R. Krishnakumar, T. Saitoh, T.
          Mizokawa, A. Sekiyama, K. Kobayashi, A. Fujimori, E. Weschke,
          R. Meier, G. Kaindl, Y. Takeda, and M. Takano, Phys. Rev. B
          53, 6873 (1996).

[SAR98]   D. D. Sarma, A. Chainani, S. R. Krishnakumar, E. Vescovo, C.
          Carbone, W. Eberhardt, O. Rader, Ch. Jung, Ch. Hellwig, W.
          Gudat, H. Srikanth, and A. K. Raychaudhuri, Phys. Rev. Lett.
          80, 4004 (1998).

[SCH95]   P. Schiffer, A. P. Ramirez, W. Bao, and S.-W. Cheong, Phys. Rev.
          Lett. **75**, 3336 (1995).

[SHE87]   Z.-X. Shen, W. Allen, J. J. Yeh, J.-S. Kang, W. Ellis, W. Spicer,
          I. Lindau, M. B. Maple, Y. D. Dalichaouch, M. S. Torikachvili, J.
          Z. Sun, and T. H. Geballe, Phys. Rev. B **36**, 8414 (1987).

[SHI97]   H. Shiba, R. Shiina, and A. Takahashi, J. Phys. Soc. Jpn. **66**, 941 (1997).

[SIG96]   M. Sigrist and A. Furusaki, J. Phys. Soc. Jpn. **65**, 2385 (1996).

[STO97]   B. P. Stojković and D. Pines, Phys. Rev. B **56**, 11 931 (1997).

[SUZ88]   Y. Suzumura, Y. Hasegawa, and H. Fukuyama, J. Phys. Soc. Jpn. **57**, 2768 (1988).

[TAE94]   K. Takenaka, K. Mizuhashi, H. Takagi, and S. Uchida, Phys. Rev. B **50**, 6534 (1994).

[TAI91]   M. Takigawa, A. P. Reyes, P. C. Hammel, J. D. Thompson, R. H. Heffner, Z. Fisk, and K. C. Ott, Phys. Rev. B **43**, 247 (1991).

[TAK89]   H. Takagi, S. Uchida, and Y. Tokura, Phys. Rev. Lett. **62**, 1197 (1989).

[TER97]   J. M. De Teresa, M. R. Ibarra, P. A. Algarabel, C. Ritter, C. Marquina, J. Blasco, J. Garcia, A. del Moral, and Z. Arnold, Nature (London) **386**, 256 (1997).

[TSV92]   A. M. Tsvelik, Phys. Rev. Lett. **69**, 2142 (1992).

[UCH96]   S. Uchida, K. Tamasaku, K. Takenaka, and Y. Fukuzumi, J. Low Temp. Phys. **105**, 723 (1996).

[UEM91]   Y. J. Uemura, L. P. Le, G. M. Luke, B. J. Sternlieb, W. D. Wu, J. H. Brewer, T. M. Riseman, C. C. Seaman, M. B. Maple, M. Ishikawa, D. G. Hinks, J. D. Jorgensen, G. Saito, and H. Yamochi, Phys. Rev. Lett. **66**, 2665 (1991).

[URU95]   A. Urushibara, Y. Moritomo, T. Arima, A. Asamitsu, G. Kido, and Y. Tokura, Phys. Rev. B **51**, 14 103 (1995).

[VAR96]   C. M. Varma, Phys. Rev. B **54**, 7328 (1996).

[WAL74]   R. Walstedt and L. R. Walker, Phys. Rev. B **9**, 4857 (1974).

[WEN96]   X.-G. Wen and P. A. Lee, Phys. Rev. Lett. **76**, 503 (1996).

[WOL55]   E. O. Wollan and W. C. Koehler, Phys. Rev. **100**, 545 (1955).

[WOO97]   B. F. Woodfield, M. L. Wilson, and J. M. Byers, Phys. Rev. Lett. **78**, 3201 (1997).

[XIA87]   G. Xiao, F. H. Streitz, A. Gavrin, Y. W. Du, and C. L. Chien, Phys. Rev. B **35**, 8782 (1987).

[YOS89a]   D. Yoshioka, J. Phys. Soc. Jpn. **58**, 32 (1989).

[YOS89b]   D. Yoshioka, J. Phys. Soc. Jpn. **58**, 1516 (1989).

[ZEN51]   C. Zener, Phys. Rev. **82**, 403 (1951).

[ZHA88]   F. C. Zhang and T. M. Rice, Phys. Rev. B **37**, 3759 (1988).

[ZHO96]   G. M. Zhao, K. Conder, H. Keller, and K. A. Müller, Nature (London) **381**, 676 (1996).

[ZHE93]   G. Zheng, T. Odaguchi, T. Mito, Y. Kitaoka, K. Asayama, and Y. Kodama, J. Phys. Soc. Jpn. **62**, 2591 (1993).

List of Publications

- R. Kilian, S. Krivenko, G. Khaliullin, and P. Fulde, "Impurity-induced spin polarization and NMR line broadening in underdoped cuprates," Phys. Rev. B **59**, 14 432 (1999).

- G. Khaliullin, S. Krivenko, R. Kilian, and P. Fulde, "Theory of impurity-induced NMR line broadening in underdoped cuprates," Physica B **259**, 504 (1999).

- R. Kilian and G. Khaliullin, "Orbital liquid state in ferromagnetic manganites," Physica B **259-261**, 805 (1999).

- G. Khaliullin, R. Kilian, S. Krivenko, and P. Fulde, "Local spin polarization in underdoped cuprates with impurities," Physica C **317**, 494 (1999).

- R. Kilian and G. Khaliullin, "Orbital Polarons in the Metal-Insulator Transition of Manganites," cond-mat/9904317 and cond-mat/9906045 (1999).

- G. Khaliullin and R. Kilian, "Orbital Dynamics: The Origin of Anomalous Magnon Softening in Ferromagnetic Manganites," cond-mat/9904316 (1999).

- G. Khaliullin and R. Kilian, "Orbital order out of spin disorder: How to measure the orbital gap," cond-mat/9904318 (1999).

- R. Kilian and G. Khaliullin, "Orbital dynamics: The origin of the anomalous optical spectra in ferromagnetic manganites," Phys. Rev. B **58**, R11 841 (1998).

- G. Khaliullin, R. Kilian, S. Krivenko, and P. Fulde, "Impurity-induced moments in underdoped cuprates," Phys. Rev. B **56**, 11 882 (1997).

- G. Khaliullin, S. Krivenko, R. Kilian, and P. Fulde, "Impurity effects in spin liquids," Physica C **282**, 1749 (1997).

Zusammenfassung

Die vorliegende Arbeit behandelt den metallischen Zustand von Übergangs-metalloxid-Verbindungen, speziell von Kupfer- und Manganoxiden, den Kupraten und Manganiden. In Kupraten wurde 1986 die Hochtemperatur-Supraleitung entdeckt, ein Phänomen, dessen zugrundeliegender Mechanismus bis heute nicht geklärt ist. Kuprate weisen auch im normalleitenden Zustand ungewöhnliche Eigenschaften auf, von denen allgemein angenommen wird, dass sie Rückschlüsse auf den Paarungsmechanismus des supraleitenden Zustands erlauben. Im Gegensatz zu den Kupraten waren Manganide schon sehr früh Gegenstand intensiver Untersuchungen. Auslöser war der in den 50er Jahren entdeckte Zusammenhang zwischen elektrischen und magnetischen Eigenschaften: Metallisches Verhalten und Ferromagnetismus bedingen einander in diesen Materialien. Kern dieses Verhaltens ist die Doppelaustausch-Wechselwirkung der Leitungselektronen, jedoch weist eine Vielzahl von Experimenten der letzten Jahre darauf hin, dass die Eigenschaften von Manganiden durch weitere, bisher nur unzureichend verstandene Mechanismen bestimmt sind.

Kuprate und Manganide gehören zu den Übergangsmetalloxiden. Diese Verbindungen lassen sich allgemein durch die Anwesenheit einer starken, aber lokal begrenzten Abstoßung zwischen den Leitungselektronen charakterisieren. Das Gegenspiel zwischen dieser lokalen Wechselwirkung und der Tendenz der Leitungselektronen, einen delokalen Zustand einzunehmen, prägt nachhaltig die physikalischen Eigenschaften dieser Materialien. Die Behandlung solcher Korrelationseffekte entzieht sich der konventionellen Theorie schwach wechselwirkender Elektronen. In dieser Arbeit wird stattdessen eine einfache und dennoch wirkungsvolle Methode angewendet, die den wesentlichen Aspekt korrelierter Metalle, die Dualität lokaler und delokaler Elektroneneigenschaften, erfasst. Dies wird durch die Aufteilung der Leitungselektronen in getrennte Quasiteilchen erreicht, denen jeweils der Ladungs-, Spin- und der orbitale Zustand eines Elektrons zugewiesen wird. Spinonen und Orbitonen, die Quasiteilchen der Spin- und orbitalen Freiheitsgrade in Kupraten bzw. Manganiden, verhalten sich in der metallischen Phase nähe-

rungsweise als Fermionen und bilden eine Spin- bzw. orbitale Flüssigkeit. Dieses Konzept liegt, in verschiedenen Abwandlungen, der vorliegenden Arbeit zugrunde. Die Einführung von Hilfsteilchen mag auf den ersten Blick künstlich erscheinen, jedoch hat der theoretische Zugang ein Analogon in der reellen Welt: Experimente weisen darauf hin, dass Spin- und Ladungsfreiheitsgrade in Kupraten teilweise voneinander entkoppelt sind. Jenseits dieser direkten Korrespondenz zwischen Theorie und Experiment ist die hier vorgestellte Methode als ein theoretisches Werkzeug zu verstehen, das eine transparente Behandlung der Korrelationseffekte ermöglicht.

Gegenstand unserer Untersuchungen ist der metallische Zustand von Kupraten und Manganiden. Die ersteren zeigen ungewöhnliche magnetische Eigenschaften, die am deutlichsten bei niedrigen Lochdotierungen zutage treten: (1) Die Spins der Leitungselektronen paaren sich zu Singuletts, die starken räumlichen Fluktuationen unterliegen. (2) Magnetische Anregungen niedriger Energie sind durch die Ausbildung eines „Spin Gaps" unterdrückt. (3) Antiferromagnetische Korrelationen deuten auf die unmittelbare Nähe des antiferromagnetisch geordneten Néel Zustands hin. Wir beschreiben dieses breite Spektrum magnetischer Eigenschaften ausgehend vom Bild einer Spinflüssigkeit. Um einen Vergleich dieses Zugangs mit experimentellen Ergebnissen zu ermöglichen, untersuchen wir die Reaktion der Kupferspins auf das Einbringen von Störstellen in die Kupferoxidschichten und die daraus resultierenden Auswirkungen auf Kernspinresonanz-Messungen. Das Zusammenspiel der magnetischen Eigenschaften der Störstellen und dem Magnetismus der Kupferoxidebenen führt zu mehreren interessanten Beobachtungen, die sich im Einklang mit experimentellen Ergebnissen befinden: Sowohl magnetisch aktive ($S = 1$) als auch inaktive ($S = 0$) Störstellen verhalten sich in Kupraten wie effektive Spins $S = 1/2$. Diese Beobachtung stellt ein starkes Indiz für die oben erwähnte Spinsingulett-Struktur der Kuprate dar. Das Einbringen einer Störstelle entzieht einem der Singuletts seinen Partner, womit ein ungepaarter Spin verbleibt. Im Fall einer nichtmagnetischen Störstelle ist dieser Spin direkt beobachtbar. Anders verhält es sich bei einer magnetischen Störstelle: Hier wird das eingebrachte $S = 1$ Moment teilweise durch den freien Kupferspin abgeschirmt, woraus ein effektiver Spin $S = 1/2$ resultiert. Dieser unterschiedliche Mechanismus schlägt sich in der lokalen Polarisierbarkeit der Kupferspins nieder und erklärt das bisher als widersprüchlich erachtete Verhalten magnetischer und nichtmagnetischer Störstellen in Kernspinresonanz-Messungen. Desweiteren konnte in dieser Arbeit das ungewöhnliche Temperaturverhalten der Resonanz-Linienbreite, das deutlich vom zu erwartenden Curie Gesetz abweicht, auf die Anwesenheit antiferromagnetischer Korrelationen zurückgeführt werden. Zusammenfassend ist zu betonen, dass die hier diskutierten Ergebnisse klar das ungewöhnliche Zu-

sammentreffen von Spinsingulett-Paarung und antiferromagnetischen Korrelationen in unterdotierten Kupraten aufzeigen.

In Manganide unterliegen die Leitungselektronen, ähnlich wie in den Kuprate, einer starken lokalen Abstoßung. Dennoch unterscheiden sich die zwei Substanzen in einem wesentlichen Punkt: Die Doppelaustausch-Wechselwirkung in Manganiden bewirkt die fast vollständig Polarisierung des magnetischen Moments bei niedrigen Temperaturen. Das Pauli Prinzip verbietet dann jede Doppelbesetzung eines einzelnen Orbitals. Nichtsdestotrotz können auch in Manganiden zwei Elektronen gemeinsam einen Gitterplatz besetzen und somit gegenseitig in Wechselwirkung treten. Dies liegt in der Tatsache begründet, dass sich die Leitungselektronen innerhalb eines orbitalen Dubletts bewegen. Der orbital Freiheitsgrad ist somit wichtige Voraussetzung für Korrelationseffekte in metallischen Manganiden. Wir beschreiben diese Korrelationen mit Hilfe des Konzeptes einer orbitalen Flüssigkeit: In Analogie zu der Entkoppelung von Spin und Ladung in einer Spinflüssigkeit werden unterschiedlich Quasiteilchen zur Beschreibung der orbitalen und der Ladungsfreiheitsgrade eingeführt. Diese Quasiteilchen sind in erster Näherung entkoppelt. Eine genauere Betrachtung schließt jedoch die Wechselwirkung zwischen den Teilchen mit ein, die in der Tatsache begründet liegt, dass jeweils zwei Quasiteilchen gemeinsam ein Elektron bilden. Die Berechtigung für die hier eingeschlagene Vorgehensweise wird anschaulich demonstriert anhand der hier präsentierten Ergebnisse. Diese weisen ein hohes Maß an Übereinstimmung mit experimentellen Daten auf, die sich einer theoretischen Beschreibung bisher entzogen haben.

Manganide zeigen in ihrer metallischen Phase ein stark inkohärentes optisches Spektrum, das selbst bei Temperaturen nahe dem absoluten Nullpunkt noch deutlich ausgeprägt ist. Dabei überrascht vorallem die Energieskala des Spektrums, das bis etwa 1 eV reicht. Manganide weisen damit ein Verhalten auf, das konträr zu dem konventioneller Metalle steht: Bei letzteren akkumuliert das spektrale Gewicht bei tiefen Temperaturen größtenteils in einem niederfrequenten „Drude Peak". Aufbauend auf dem Konzept einer orbitalen Flüssigkeit lässt sich dieses ungewöhnliche Verhalten der Manganide auf Korrelationen zwischen den Leitungselektronen zurückführen. Weiter konnte durch eine Analyse der spezifischen Wärme der zuvor von verschiedenen Autoren geäußerte Verdacht widerlegen werden, dass das Bild eines korrelierten metallischen Zustands im Widerspruch zu den experimentellen Werten des Wärmekoeffizienten stehe. Schließlich wurde die wichtige Rolle des Jahn-Teller Effekts in Manganiden diskutiert, welcher der orbitalen Entartung des Leitungsbandes entspringt. Die Anwesenheit dieses phononischen Effekts konnte aus dem optischen Spektrum abgeleitet werden. Zusammenfassend zeigen unsere Ergebnisse, dass Korrelationen zwischen den Leitungselektro-

nen eine wichtige Rolle in der Physik der Manganide spielen und dass diese
zudem durch die Koppelung der Leitungselektronen an Gittermoden ergänzt
werden.

Die magnetischen Eigenschaften metallischer Manganide werden durch
die Doppelaustausch-Wechselwirkung bestimmt: Die Leitungselektronen be-
wegen sich vor dem Hintergrund lokalisierter Spins. Aufgrund der Hundschen
Kopplung an diese Spins übertragen die Leitungseletronen bei ihrer Bewe-
gung eine ferromagnetische Wechselwirkung zwischen benachbarten Gitter-
plätzen. Es ist zu erwarten, dass Korrelationseffekte die spezifische Aus-
prägung dieser Austauschwechselwirkung beeinflussen. In der Tat konnte
in dieser Arbeit mit Hilfe des Bildes einer orbitalen Flüssigkeit gezeigt wer-
den, dass sich die in einigen Manganiden zu beobachtende Abflachung des
magnetischen Anregungsspektrums auf Korrelationen zwischen orbital entar-
teten Leitungselektronen zurückführen lässt. Dieser Mechanismus wird noch
verstärkt durch die Koppelung an Gittermoden, was unsere bereits zuvor
geäußerte Annahme der Wichtigkeit des Jahn-Teller Effekts in Manganiden
unterstreicht. Das Zusammenwirken von Doppelaustausch-Wechselwirkung
und der Dynamik des Kristallgitters führt im Vorfeld der Ausbildung kollekti-
ver Gitterverzerrungen zu einer drastischen Renormierung des magnetischen
Spektrums. Die Rolle, die hierbei sowohl dem Jahn-Teller Effekt als auch der
Kinetik der Leitungselektronen zufällt, wurde angerissen. Zusammenfassend
konnte der Einfluss von Korrelationseffekten und der orbitalen Entartung auf
das magnetische Verhalten von Manganiden herausgearbeitet werden. Zu be-
tonen ist dabei insbesondere der dominante Einfluss von Gittermoden, der
die immanente Tendenz der metallischen Phase zur Ausbildung kollektiver
Gitterverzerrungen zum Ausdruck bringt.

Abschließend wurde in dieser Arbeit eine Theorie des Metall-Isolator
Übergangs in Manganiden vorgestellt, die die bisher unerklärte Abhängig-
keit des Phasendiagramms von der Lochdotierung einschließt. Dazu wurde
das Konzept orbitaler Polaronen eingeführt: Löcher können in einem orbi-
tal entarteten Hubbardmodell ihre Umgebung polarisieren, d.h. sie können
durch eine Verschiebung der Sauerstoffionen und durch die Coulombwech-
selwirkung mit ihrer Umgebung eine Aufhebung der orbitalen Entartung an
benachbarten Gitterplätzen hervorrufen. Dieser Effekt ist bei niedrigen Do-
tierungskonzentrationen besonders ausgeprägt und verschwindet bei höher-
en Lochdichten. Der metallische Zustand entwickelt dadurch bei niedriger
Dotierung die Tendenz, gebundene Zustände zwischen Löchern und den sie
umgebenden Orbitalen auszubilden. Dieser Übergang, bei dem die freien La-
dungsträger effektiv durch Polaronen ersetzt werden, wird von einem scharfen
Einschnitt in der Bandbreite begleitet, was schließlich den Lokalisierungspro-
zess auslöst. Die vorgestellte Theorie wird ergänzt durch die Möglichkeit der

Bildung von Gitterpolaronen. Durch die Beschreibung des Zusammenwirkens von Doppelaustausch-Wechselwirkung und polaronischen Effekten konnten somit erfolgreich die wesentlichen Aspekte des Phasendiagrams von Manganiden bei niedrigen und mittleren Lochkonzentrationen reproduziert werden. Besonders zu erwähnen ist hierbei die vollständige Unterdrückung metallischen Verhaltens unterhalb einer kritischen Lochkonzentation sowie das Auftreten von Ferromagnetismus in isolierenden Phasen. Diese im Experiment zu beobachtenden Effekte entziehen sich einer Erklärung durch eine konventionellen Theorie der Doppelaustausch-Wechselwirkung. Zusammenfassend kann betont werden, dass die Polarisierung der Orbitale in der Umgebung von Löchern wichtiger Bestandteil der Physik von Manganiden ist. Dieser Effekt hat Auswirkungen auf das gesamte Phasendiagramm, die weit über die hier aufgezeigte Rolle in der Lokalisierung der Ladungsträger hinausreichen.

Thesen

- Korrelationen der Leitungselektronen beeinflussen nachhaltig das physikalische Verhalten von Kupraten und Manganiden. Diese stellen in ihrem Grundzug Mott-Hubbard Systeme dar.

- Metallische Kuprate bilden bei niedriger Lochkonzentration eine Spinflüssigkeit. Dies steht im Einklang mit experimentellen Untersuchungen an störstellendotierten Kupraten.

- Das Spinflüssigkeitsverhalten von Kupraten ist durch das Zusammenspiel von Spinsingulett-Paarung und antiferromagnetischen Korrelationen charakterisiert.

- Die orbitale Entartung der Leitungselektronen ist wesentliche Voraussetzung für Korrelationseffekte in metallischen Manganiden. Das Konzept einer orbitale Flüssigkeit ist in der Lage, diese Effekte zu erfassen.

- Das experimentell zu beobachtende inkohärente optische Spektrum in metallischen Manganiden ist auf Korrelationseffekte zurückzuführen.

- Ein Widerspruch zwischen Messergebnissen des Wärmekoeffizienten in Manganiden und dem Bild eines korrelierten Metalls besteht nicht.

- Die Doppelaustausch-Wechselwirkung wird durch Korrelationseffekte und die orbitale Entartung beeinflusst. Dies bestimmt das ungewöhnliche magnetische Anregungsspektrum metallischer Manganide.

- Der zusätzliche Einfluss von Gittermoden bewirkt eine dramatische Veränderung des magnetischen Anregungsspektrums in unmittelbarer Nähe des Übergangs zu einer orbital geordneten Phase.

- Die Polarisierung von Orbitalen in der Umgebung von Löchern ist immanenter Bestandteil des orbital entarteten Mott-Hubbard Modells.

- Die orbitalen Polarisierung ermöglicht die Bildung orbitaler Polaronen. Diese spielen eine wichtige Rolle bei der Beschreibung des Metall-Isolator Übergangs in Manganiden.

Acknowledgements

Curriculum Vitae

ROLF KILIAN
Born in Ulm, Germany, on April 8th, 1969

PRIMARY EDUCATION

1975 - 1979   Elementary School, Ulm

SECONDARY EDUCATION

1979 - 1986   Schubart Gymnasium, Ulm
1986 - 1987   Castro-Valley High School, San Francisco, U.S.A.
1987 - 1989   Schubart Gymnasium, Ulm

MILITARY SERVICE

1989 - 1990   Compulsory military service, Ulm

UNIVERSITY

1990 - 1993   Freie Universität Berlin
                     - Vordiplom in Physics
                     - Vordiplom in Mathematics
1993 - 1994   State University of New York at Stony Brook, U.S.A.
                     - Master of Arts in Physics
1994 - 1996   Universität Hamburg
                     - Diplom in Physics

DOCTORAL DEGREE

1996 - 1999   Max-Planck-Institut für Physik komplexer Systeme,
                     Dresden

Versicherung

Hiermit versichere ich, dass ich die vorliegende Arbeit ohne unzulässige Hilfe Dritter und ohne Benutzung anderer als der angegebenen Hilfsmittel angefertigt habe; die aus fremden Quellen direkt oder indirekt übernommenen Gedanken sind als solche kenntlich gemacht. Die Arbeit wurde bisher weder im Inland noch im Ausland in gleicher oder ähnlicher Form einer anderen Prüfungsbehörde vorgelegt. Die Arbeit wurde unter Betreuung von Prof. Dr. Peter Fulde und Prof. Dr. Giniyat Khaliullin am Max-Planck-Institut für Physik komplexer Systeme in Dresden angefertigt. Die Promotionsordnung wird anerkannt.

Dresden, im Mai 1999